4D *In situ* Visualization of Chemo-mechanical Membrane Degradation in Fuel Cells: Understanding and Mitigating Edge Failures

by

Yixuan Chen

B.Sc., University of Alberta, 2018

Thesis Submitted in Partial Fulfillment of the
Requirements for the Degree of
Master of Applied Science

in the
School of Mechatronic Systems Engineering
Faculty of Applied Sciences

© Yixuan Chen 2020
SIMON FRASER UNIVERSITY
Summer 2020

Approval

Name:	**Yixuan Chen**
Degree:	**Master of Applied Science**
Title:	**4D *In situ* Visualization of Chemo-mechanical Membrane Degradation in Fuel Cells: Understanding and Mitigating Edge Failures**
Examining Committee:	**Chair: Ramtin Rakhsha** Lecturer
	Erik Kjeang Senior Supervisor Associate Professor
	Francesco P. Orfino Supervisor Research Associate
	Nimal Rajapakse Internal Examiner Professor School of Engineering Science
Date Defended/Approved:	August 17th, 2020

Abstract

Fuel cell is a zero-emission energy conversion device using hydrogen and oxygen to generate power with water as the only by-product. Membrane electrode assembly (MEA) edges are sensitive regions that could influence the overall durability of fuel cells, where membrane degradation at poorly designed edges may lead to premature cell failures. In this work, two MEA edge designs were implemented to study their robustness during combined chemical and mechanical accelerated stress testing. Four-dimensional *in situ* visualization, enabled by X-ray computed tomography, was performed to understand and mitigate the edge failure issue. Interaction of adhesive-containing polyimide gasket with catalyst coated membrane (CCM) was identified as the key contributor to premature edge failures, which was mitigated by using a non-adhesive inert frame at the CCM interface, thus enabling a robust MEA edge wherein the failures were shifted into the active area. Overall, findings of this research may contribute to robust fuel cell manufacturing and enhanced membrane durability.

Keywords: fuel cell; membrane durability; edge design; mechanical degradation; chemical degradation; X-ray computed tomography

To Suzumiya Haruhi

Acknowledgements

First of all, I would like to thank my senior supervisor Dr. Erik Kjeang for giving me this opportunity to conduct fuel cell research as a research assistant in his lab, and for his advice, support (both academically and financially), and guidance throughout my entire master career. I'm also thankful to Dr. Nimal Rajapakse for being my internal examiner.

I would also like to thank the following individuals from SFU Fuel Cell Research Lab (FCReL) and Ballard Power Systems: Mr. Francesco Orfino for his enormous knowledge and expertise in fuel cell and X-ray computed tomography (XCT); Ms. Monica Dutta for coordinating the research group with Ballard and her supervision; Ms. Natalia Kremliakova and Dr. Pei Pei for managing the lab and ordering lab supplies in time; Dr. Yadvinder Singh and Mr. Dilip Ramani for their expertise in membrane degradation and AST conditions; Dr. Robin T. White for his expertise in XCT and image processing; Mr. Jonas Stoll for his experience in manufacturing and prototyping; Dr. Narinder Singh Khattra for sharing interesting Indian cultures with me. Their help and input are essential to the success of this work. Furthermore, I would also like to thank the staff at SFU 4D LABS for providing training and technical support on laser micromachining.

My thanks also to coop students Mr. Ardavan Mohseni-Javid and Mr. Francesco Pero for helping me conduct degradation tests in every stage of my work, so that I can enjoy a nap in my office after lunch rather than staring at the test station. Wish you all the best in your study and career in the future.

Last but not least, I would like to thank my parents for keep worrying about my career and progress, although your worry didn't help me finish the degree earlier. Thank you for your endless love.

Table of Contents

List of Tables

List of Figures

x

List of Acronyms

2D/3D/4D	Two/three/four dimensional
ACL	Anode Catalyst Layer
AST	Accelerated Stress Testing
BOL	Beginning-of-life
CCL	Cathode Catalyst Layer
CCM	Catalyst Coated Membrane
CL	Catalyst Layer
COCV	Cyclic Open Circuit Voltage
CV	Cyclic Voltammetry
EIS	Electrochemical Impedance Spectroscopy
ELDT	Electrochemical Leak Detection Test
EOL	End-of-life
EPSA	Effective Platinum Surface Area
ePTFE	Expanded Polytetrafluoroethylene
FCReL	Fuel Cell Research Lab
FEP	Fluorinated Ethylene Propylene
FOV	Field of View
GDE	Gas Diffusion Electrode
GDL	Gas Diffusion Layer
GHG	Greenhouse Gas
HART	High Aspect Ratio Tomography
HFCV	Hydrogen Fuel Cell Vehicle
HFR	High Frequency Resistance
HOR	Hydrogen Oxidation Reaction
ICE	Internal Combustion Engine
MEA	Membrane Electrode Assembly
MPL	Microporous Layer
OCV	Open Circuit Voltage
ORR	Oxygen Reduction Reaction
PEM	Proton Exchange Membrane
PEMFC	Proton Exchange Membrane Fuel Cell

PFSA	Perfluorosulfonic Acid
PTFE	Polytetrafluoroethylene
PVDF	Polyvinylidene Fluoride
RH	Relative Humidity
SEM	Scanning Electron Microscope
SOFC	Solid Oxide Fuel Cell
SPIs	Sulfonated Polyimides
SPSs	Sulfonated Polystyrene Copolymers
SSF	Small Scale Fixture
TC	Thermal Couple
US DOE	The United States Department of Energy
XCT	X-ray Computed Tomography

Chapter 1.   Introduction

Global warming has become a survival issue for the entire human race since several decades ago. In a recent report by the Canadian government, it is believed that the warming in Canada is about twice the magnitude of global warming on average [1]. Human activities have significant impact on the ever-growing global warming issue, such as burning fossil fuels and deforestation. Those activities produce great amount of carbon dioxide, which is a type of greenhouse gas (GHG). GHG produces greenhouse effect, where incoming heat through radiation of the sun is trapped by the earth's atmosphere and causes warming issue [2]. Therefore, reducing GHG emission is an effective way to fight the global warming and climate change. According to statistical data in year 2017, the transportation sector was the second largest GHG contributor in Canada, accounting for 24% [3]. Between 1990 and 2017, GHG emission in the transportation sector has grown by 43%, mainly due to freight trucks and passenger light trucks [3]. In order to reduce transportation GHG emission, engineers and scientists have been working on finding alternative power solutions to replace the traditional internal combustion engine (ICE) for automotive use. Ideally, the alternative energy sources should be completely GHG emission free, or at least produce less GHG. The fuel cell, which was invented back in 1839 by Sir William Grove [4], is considered as a promising alternative to ICE. Fuel cell is an energy conversion device that converts chemical energy of the fuel directly into electrical energy without combustion [5]. In general, fuel cell has higher efficiency than ICE. After more than hundred years of development and engineering efforts, various fuel cells in different categories have been invented and put into practice to address different levels of power needs. Nowadays, the most common way to categorize fuel cell is by electrolyte. Common types include alkaline fuel cell, solid oxide fuel cell (SOFC), and proton exchange membrane fuel cell (PEMFC). Among the many fuel cell types, PEMFC that uses hydrogen as its fuel is particularly promising in automotive application because of its low operation temperature (below 100°C), zero GHG emission, and higher efficiency compared to ICE. With the release of Toyota Mirai® (Japanese for "future") in year 2014 [6], hydrogen fuel cell sedan-like vehicle (HFCV) first became commercially available to the general public. Moreover, fuel cell bus fleets are currently operated around the world, marking the maturity of fuel cell technology in automotive application. According to some studies, the

adoption rate of alternative energy vehicle needs to reach 80-90% in Canada by 2050 in order to meet national GHG reduction target [7,8]. However, durability and cost effectiveness remain major barriers for HFCV mass adoption. Low temperature PEMFC requires noble metal platinum as catalyst to make fuel cell reactions happen. Moreover, other core components including membrane, gas diffusion media, and bi-polar plates are also costly [9]. In addition to reducing fuel cell stack cost, prolonging fuel cell lifetime is also an effective way to improve cost effectiveness. During automotive dynamic fuel cell operation, mixed degradation processes including mechanical degradation, chemical degradation, and thermal degradation will take place and gradually deduct fuel cell performance over time until ultimate failure is reached [10–12]. The United States Department of Energy (US DOE) has proposed an ultimate lifetime target of 25,000 hours for fuel cell buses, and combined chemical and mechanical durability of 20,000 hours for membrane by year 2020 [13,14]. Therefore, research on fuel cell degradation, especially on membrane degradation has gained significant attention [15], and is critical to fuel cell commercialization and product realization. Fuel cell degradation study is usually carried out on lab scale with accelerated experiments and involves application of electrochemical diagnostics techniques that detect degradation and performance loss. Visualization is another key failure analysis method that provides additional understanding. Scanning electron microscope (SEM) is a commonly used visualization tool; however, SEM based visualization is limited to 2D *ex situ* surface visualization of specimens, which is often insufficient to fully resolve the dynamic degradation processes associated with the 3D structure of the fuel cell. To overcome the shortcomings of SEM, X-ray computed tomography (XCT) has been gaining popularity owing to its non-destructive 3D visualization capability [16]. The non-destructive nature of XCT also provides the feasibility of 4D *in situ* and *operando* visualization with three space dimensions and one time dimension. In this work, the degradation mechanism of proton exchange membrane under combined chemical and mechanical stressors is studied, with the application of 4D *in situ* visualization conducted by XCT imaging technique.

1.1. Proton Exchange Membrane Fuel Cells

As indicated in Figure 1, a PEMFC is typically composed of (i) flow field plates that create paths for the reactants to enter the fuel cell; (ii) gas diffusion layers (GDLs), which facilitate reactant and product transport to/from reaction sites; (iii) anode and

2

cathode catalyst layers (ACL and CCL), which contain platinum particles and provide reaction sites; and (iv) PEM, which is the electrolyte made of proton conductive but electron resistive ionomers. All of these main fuel cell components will be introduced in detail shortly. The laminated membrane, CLs, and GDLs embody the membrane electrode assembly (MEA), which is the core of a fuel cell.
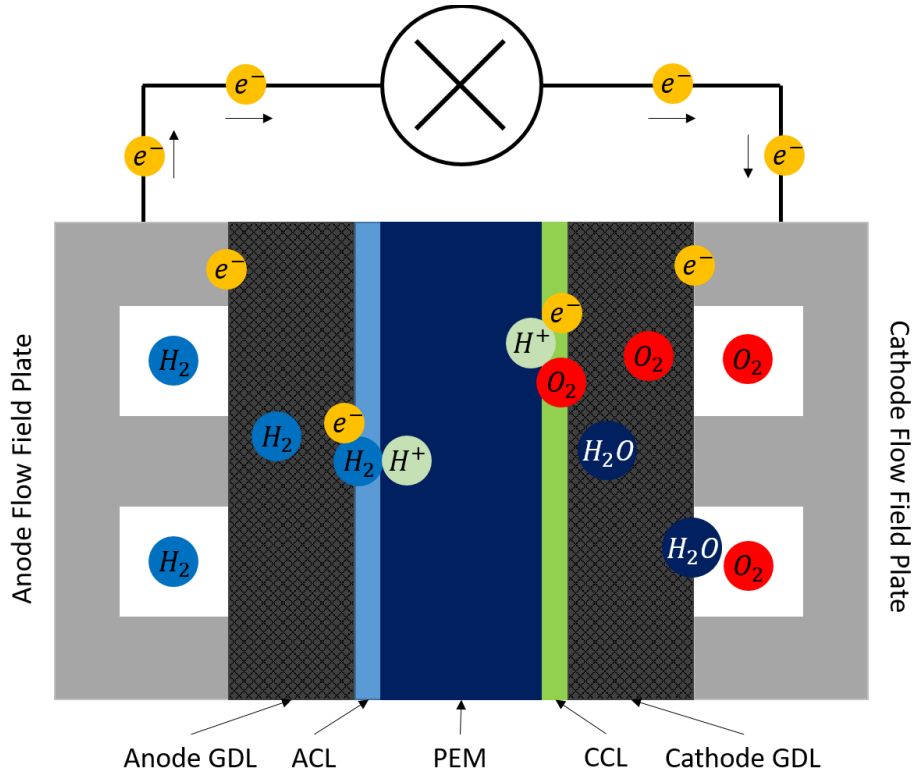
Figure 1: **Schematic of a PEMFC.**

In fuel cell reaction, hydrogen and oxygen (usually air) is supplied to the anode and cathode respectively through the flow channels. Reactant gas then diffuses through the GDL and reaches the CL. Microporous layer (MPL) is typically coated on GDL surface and lies in between GDL and CL in order to provide sufficient structural support to CL and membrane since GDL has relatively large pore size. On the ACL catalyst surface, hydrogen molecules split into protons and electrons, where protons pass through PEM electrolyte and electrons go through external circuit. On cathode side, proton, electron, and oxygen molecules meet at the CCL and combine into water. In this cell reaction, hydrogen undergoes hydrogen oxidation reaction (HOR) while oxygen undergoes oxygen reduction reaction (ORR). Anode, cathode, and the overall reaction equation can be expressed as follows:

$$\text{Anode: } 2H_2 \rightarrow 4H^+ + 4e^- \tag{1}$$

$$\text{Cathode: } O_2 + 4H^+ + 4e^- \rightarrow 2H_2O \tag{2}$$

$$\text{Overall: } 2H_2 + O_2 \rightarrow 2H_2O \tag{3}$$
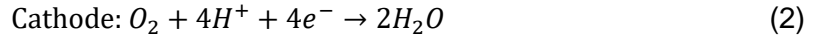
The anode reaction can be further divided into the following two reactions with platinum catalyst taking part into the reaction:

$$H_2 \leftrightarrow 2(Pt - H) \tag{4}$$

$$(Pt - H) \leftrightarrow H^+ + e^- \tag{5}$$

On platinum catalyst surface, hydrogen bonds in hydrogen gas molecules break, splitting molecules into atoms. Hydrogen atoms are then chemisorbed on platinum surface as indicated in the first step, which is referred to as the Tafel reaction. Next, electrons transfer from the hydrogen atoms that have been chemisorbed, causing protons to be released. This step is referred to as the Volmer reaction.

Total cell potential is basically the difference between HOR and ORR potential, as described in Equation 6.

$$E_{cell} = E_{cathode,red} - E_{anode,red} \tag{6}$$

In electrochemistry field, the standard hydrogen electrode (SHE) is commonly used as the datum to represent 0 potential. In hydrogen fuel cell reaction, anode HOR is the SHE while cathode ORR has a potential of +1.23 [V] relevant to the SHE. As a result, the theoretical hydrogen fuel cell potential is:

$$E_{cell} = 1.23 - 0 = 1.23 \text{ [V]} \tag{7}$$

As mentioned earlier, fuel cell is an energy conversion system that converts chemical energy into electrical energy. Fuel cell reaction is an exothermic chemical reaction that releases energy. Scientists have defined a term called thermal potential to represent the maximum voltage that can be achieved if all work released from chemical reaction is converted into electrical work. The thermal potential E_{th}, or sometimes presented as E^{oo}, can be determined using the equation below:

$$E_{th} = E^{oo} = -\frac{\Delta H}{nF} \tag{8}$$

In Equation 8, ΔH is the change in enthalpy (kJ/kmol), F is Faraday's constant (C/mol), and n is the number of electrons transferred. Under standard condition, thermal potential is 1.48 V for hydrogen fuel cell. However, not all work can be converted into electrical work due to the concept of entropy. Only reversible work, which is referred to as the Gibbs free energy (G), is the "available" energy. Therefore, another term called reversible cell potential is defined to represent the theoretical maximum cell potential that can be expected. Reversible cell potential is often represented by E_{cell} or E^o, which is 1.23 V as shown in Equation 9 under standard condition. From thermodynamic point of view, reversible cell potential is calculated by the following expression where ΔG is the total change in Gibbs free energy:

$$E_{cell} = E^o = -\frac{\Delta G}{nF} \tag{9}$$

As a result, the maximum thermodynamic efficiency of a PEMFC is:

$$\eta_{th,max} = \frac{E^o}{E^{oo}} = \frac{1.23}{1.48} = 83\% \tag{10}$$

However in practice, actual cell potential is usually below 1 [V] due to various losses such as activation loss, ohmic loss, and mass transportation loss.

1.1.1. Proton Exchange Membrane

Proton exchange membrane functions as gas separator and electrolyte which conducts protons from anode electrode to cathode electrode but resists electrons. In fuel cell industry, perfluorosulfonic acid (PFSA) ionomer based membrane such as DuPont Nafion® is most commonly used due to its high proton conductivity and stability [17]. Nafion® NR 211, which is used in this work, has the chemical structure shown in Figure 2.
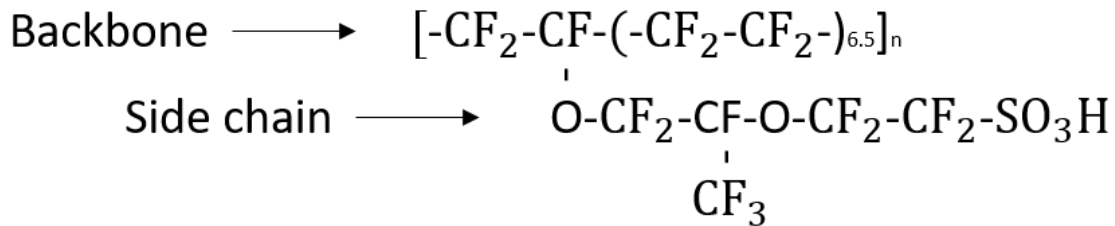
Figure 2: **Chemical structure of Nafion® NR 211 [18].**

As indicated in Figure 2, the NR 211 ionomer molecule is composed of polytetrafluoroethylene (PTFE) as backbone structure that is both chemically and mechanically stable, and sulfonic acid side chain [19]. The PTFE backbone structure is hydrophobic and proton resistive, but sulfonic acid side chain is hydrophilic and proton conductive. PFSA membrane is usually hydrated during operation, given the fact that ion conductivity of PFSA membrane almost reduces to 0 in dry state. The hydrophilic side chains can be considered as isolated clusters in the membrane structure, which are surrounded by hydrophobic PTFE. Under dry condition, proton physically transports between clusters, and this mechanism is referred to as *vehicular mechanism*. However under humidified condition, water connects isolated sulfonic acid clusters and creates pathway for proton. The $H_3O^+ - SO_3^-$ group enables proton movement along the pathway, which is known as *hopping mechanism* or *Grotthuss mechanism* [20]. The schematics of *vehicular mechanism* and *Grotthuss mechanism* are demonstrated in Figure 3(a) and 3(b) respectively.
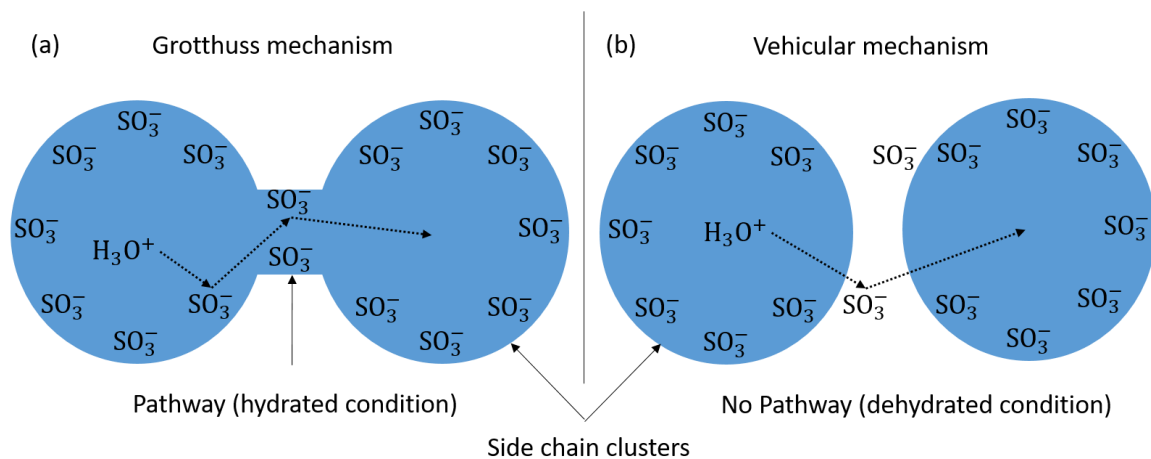
Figure 3:   **Proton transport schematics: (a) Grotthuss mechanism in hydrated membrane; and (b) Vehicular mechanism in dehydrated membrane.**

Despite the many advantages of PFSA membrane, its cost remains a major drawback since only a few companies around the world have the ability to manufacture it due to the highly regulated chemical ingredients and complex synthesis [17]. Moreover, environmental concern against PFSA due to high fluorine content has also been raised and is growing [21]. Therefore, there is increasing interest in alternative PEM materials. For instance, sulfonated hydrocarbon membrane is a substitution to PFSA membrane, which was first used in the United States space program [22]. Sulfonated hydrocarbon membrane can be classified into several subdivisions according to their backbone

structure, such as sulfonated polystyrene copolymers (SPSs) and sulfonated polyimides (SPIs) [23]. Hydrocarbon based membrane can be synthesized in various ways with relatively cheap and accessible materials [24]. Besides, most hydrocarbon membranes are more thermally and mechanically stable than PFSA membranes, but chemical stability is lower than PFSA membrane due to the relatively weak hydrocarbon bonds [25]. Comparing to PFSA membrane, hydrocarbon membrane is less gas permeable and more hydrophilic, but its proton conductivity is lower due to the less effective water channel formation [26]. Currently, the trend in fuel cell industry is to use reinforced PFSA membrane to prolong lifetime, such as using expanded PTFE (ePTFE) to reinforce the backbone structure. A schematic of ePTFE reinforced membrane is demonstrated in Figure 4.

Figure 4: **Schematic of ePTFE reinforced membrane.**

1.1.2. Catalyst Layer

Catalyst layer (CL) is present on both anode and cathode between membrane and gas diffusion media, and is a porous medium composed of carbon supported platinum particles and ionomer. There are four major functions of the CL, which are to (i) enable fuel cell reaction, (ii) conduct proton from reaction site to electrolyte, (iii) conduct electron from reaction site to gas diffusion media, and (iv) remove water out of reaction site [5]. The noble platinum metal is the actual catalyst which reduces the activation energy of chemical reaction so that HOR and ORR can happen spontaneously at relatively low temperature. However, the reaction is blocked if electrons and protons cannot get delivered to the cathode. As a result, catalyst, electronic conductor, ionic conductor, and reactant need to be present simultaneously for reaction to happen. Figure 5 shows the schematic of catalyst layer and fuel cell reaction in micro level.
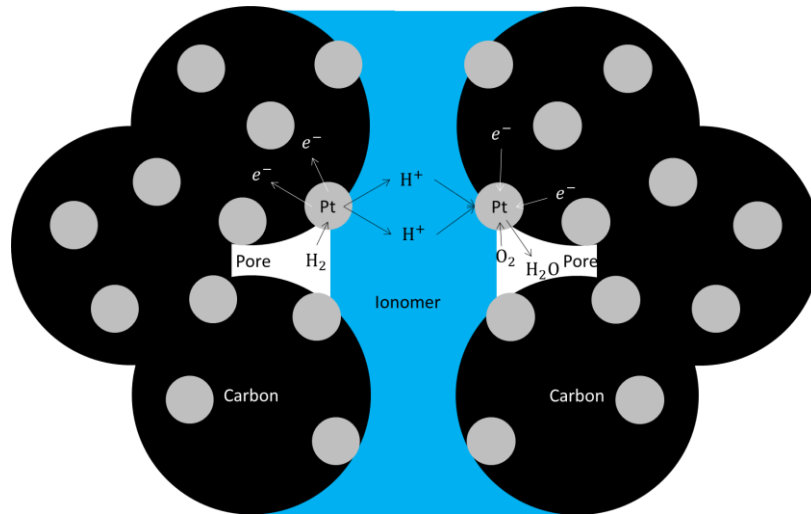
Figure 5:   **Catalyst layer in micro scale.**

In MEA fabrication, CLs could be either coated on the membrane forming catalyst coated membrane (CCM) composite [27], or on the GDLs forming gas diffusion electrodes (GDEs) [28]. In addition, hot pressing is often applied in MEA assembly to ensure good contact between each layer [29].

1.1.3. Gas Diffusion Layer

Modern PEMFCs usually employ a gas diffusion layer between flow field plate and CL to ensure uniform reactant distribution and optimize water management. GDL is a porous medium with larger pore size compared to CL, and is made of carbon based materials due to their electronic conductivity, elasticity, and chemical stability in acidic environment [30]. At present, GDL is usually composed of two layers, macroporous substrate and MPL. MPL is coated on the surface of the macroporous substrate and placed between GDL and CL to provide structural support to the CL and minimize ohmic loss by maximizing contact area. Woven carbon cloth and non-woven carbon fiber paper are the two most common materials [22] for macroporous substrate as illustrated in Figure 6. Carbon fiber is made by graphitizing at high temperature over 2000°C, and then soaked with thermoset resin to form paper. Carbon cloth, on the other hand, is first weaved with carbon yarns and then carbonized and graphitized [31]. To make water removal more effective and efficient, carbon materials have to go through hydrophobic treatment, where common hydrophobic agent such as PTFE, polyvinylidene fluoride (PVDF), or fluorinated ethylene propylene (FEP) is applied to the carbon material surface [32–34].
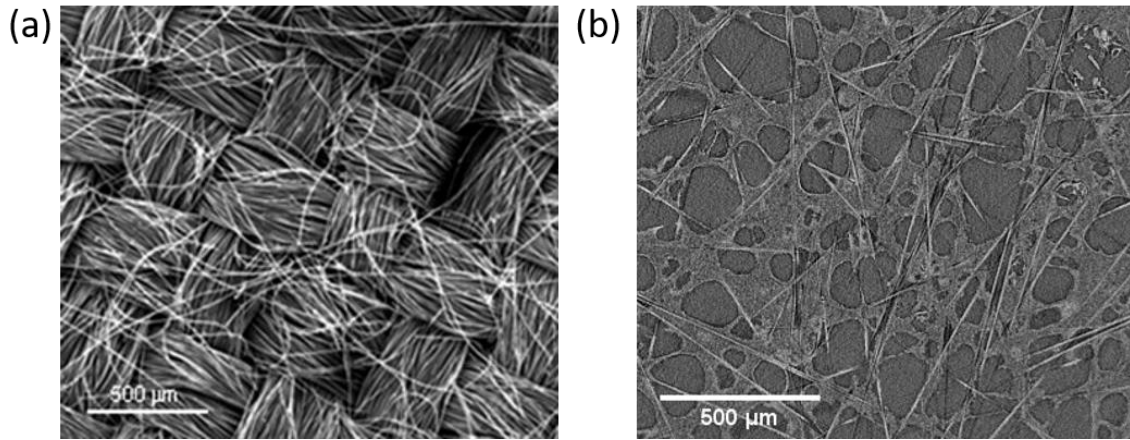
Figure 6: **(a) Woven carbon cloth GDL [35] and (b) non-woven carbon fiber paper GDL.**

1.1.4. Flow Field Plate

The flow field plate is an essential component in modern PEMFCs whose function is to deliver reactants to reaction sites and remove water from fuel cell whilst conducting electrons and heat in the solid phase. Structurlly, compression is usually applied on flow field plates to reduce contact resistance against the GDL and seal the MEA. In reality, a fuel cell stack is often composed of multiple fuel cells to meet different power demands, resulting in one flow plate serving as both anode and cathode plate for two adjacent cells. In this case, the plate will have two flow channels; one for anode and one for cathode, and such plate is referred to as bipolar plate. For a stack with multiple cells connected in series, all flow plates are bipolar plates except the first and last ones. In a PEMFC stack, bipolar flow plates could take up more than 80% of the total weight [36]. As a result, flow plates need to be highly electrically conductive, chemically and mechanically stable, robust, impermeable to gas, light, cheap, etc. Since the most important flow plate function is to deliver reactant, the flow field design needs to be optimized to deliver flow efficiently and evenly to the active cell area. Common, simple, but effective flow field designs include parallel, serpentine, interdigitated, and mesh flow channels [37] as depicted in Figure 7. Although the optimum flow field design might be much more complex, simple flow field is more cost-effective and therefore is generally preferred by the industry.
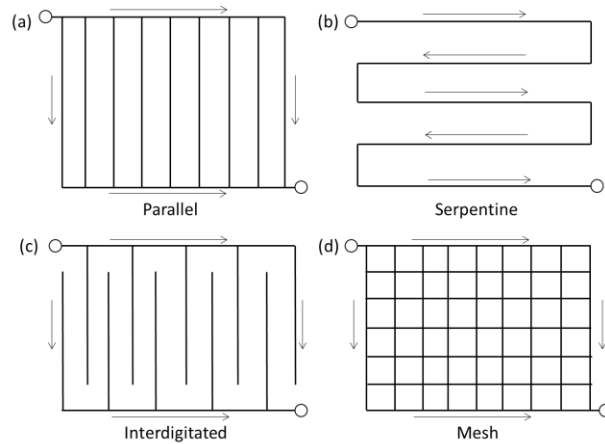
Figure 7: **Common flow field designs: (a) parallel; (b) serpentine; (c) interdigitated; and (d) mesh.**

1.2. Membrane Durability

As mentioned earlier, the fuel cell membrane is subjected to various degradation mechanisms including chemical, mechanical, and thermal degradation in dynamic automotive operation. Membrane degradation is critical and will compromise its key function as gas separator, which will then lead to significant performance loss and ultimate cell failure. Therefore, the membrane degradation mechanisms need to be studied and thoroughly understood so that mitigation strategies can be developed to prolong fuel cell lifetime. Membrane degradation study could be done by segregating the mechanisms and study each one of them separately, or it can be done with combined degradation mechanisms.

1.2.1. Chemical Degradation

In fuel cell operation, radical chemical species such as hydroxyl (•OH), hydroperoxyl (•OOH), and hydrogen (•H) [38,39] can be formed through the following reactions:

$$O_2 + 2H^+ + 2e^- \rightarrow H_2O_2 \rightarrow 2 \cdot OH \tag{11}$$

$$H_2O_2 + \cdot OH \rightarrow \cdot OOH + H_2O \tag{12}$$

$$\cdot OH + H_2 \rightarrow \cdot H + H_2O \tag{13}$$
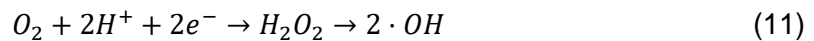
On the cathode side, hydrogen peroxide can be produced as an ORR by-product, which can later dissociate into •OH, as demonstrated in Equation 11 [38]. This reaction can also take place on anode side with crossover oxygen. In addition to dissociation, hydrogen peroxide can also react with •OH and form •OOH [40]. •H can be formed through the reaction of •OH with crossover hydrogen [39], and •H can again react with oxygen to produce more •OOH [41]. The reactions demonstrated in Equation 11-13 are only part of the complicated chemical reactions in an operating fuel cell, more detailed explanation is available elsewhere [15,42].

It has been indicated that •H could attack the C-F bond on both backbone and side chains, while •OH could attack side chain of the PFSA ionomer [18]. The SO_3H group on PFSA side chain is critical to proton conductivity. Therefore, the loss of side chain, as indicated in Figure 8 [43], could significantly impact membrane performance. Moreover, radical species attack will cause polymer chain scission, and membrane will gradually lose material in the long run. In macroscopic view, the continuous material loss will appear as global membrane thinning [44]. An effective way to detect chemical degradation is to measure fluorine release through exhaust water [45]. In addition to material loss, chemical degradation will also cause membrane embrittlement, therefore reducing membrane strength and making fractures easier to develop [46]. Cracks and holes can compromise the membrane function as gas separator and lead to the mixing of hydrogen and air. The rapid oxidation or direct combustion of hydrogen will pose more significant damage to the MEA. Operating conditions such as high temperature, low relative humidity, high voltage, and/or high reactant concentration can accelerate chemical degradation, thus these conditions are usually applied in accelerated degradation experiments [47–49].

$$[-CF_2-CF-(-CF_2-CF_2-)_{6.5}]_n$$
$$O-CF_2\text{-}CF\text{-}O\text{-}CF_2-CF_2-SO_3H \longrightarrow$$
$$CF_3$$

$$CF_3COOH$$
$$CF_2OH - CF_2SO_3H$$
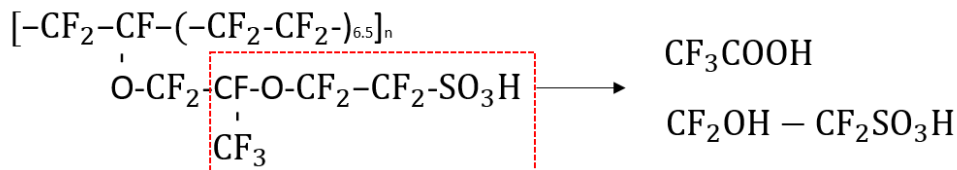
Figure 8: **PFSA membrane side chain scission schematic [43].**

1.2.2. Mechanical Degradation

Mechanical membrane degradation is driven by mechanical stresses through fatigue and creep during the dynamic fuel cell operation. PFSA ionomer based membranes are highly hygroscopic and their water uptake is strongly affected by temperature and relative humidity (RH) [50,51]. During dynamic fuel cell operation, both temperature and RH goes through rapid cyclic change, inducing membrane shrinkage and swelling accordingly. Membrane experiences in-plane tension during shrinkage and in-plane compression during swelling. Consequently, fatigue induced membrane cracks could initiate from the surfaces and propagate over time [52]. In addition to cyclic in-plane stress, improper MEA design or assembly imperfections could also cause stress concentration and induce local membrane failure, especially around the frame region where the MEA structure is inhomogeneous. The membrane may also interact with other MEA components such as CL and GDL during cycling and induce additional mechanical degradation. Recent studies have found that MPL and CL surfaces could develop cracks and holes during fabrication [53]. Catalyst layer cracks can form during the drying procedure of catalyst ink [54]. MPL ink on the other hand, could intrude into macroporous media and leave holes after drying [55]. As a result, there could be interfacial gaps between CL and MPL [53], which could result in membrane buckling during RH cycles [56]. Studies simulating the membrane buckling has demonstrated CL crack formation at the buckling sites after multiple RH cycles [56,57]. Other studies reported that CL cracks have the potential to cause stress concentration and propagate into membrane under pure mechanical degradation [44], which could finally become through-plane membrane cracks and ultimate failure. In a fuel cell stack, the compression force is concentrated under the land region since there is no mechanical support under the flow channels. Local membrane cracks or tears are more likely to happen at the interface between land and channel due to the inhomogeneous mechanical stress [15]. Additionally, creep is another mechanical membrane failure that can happen under certain conditions such as over compression even without cycling [58]. To overcome mechanical degradation, various mitigation strategies have been developed to increase membrane strength, such as applying an extra ePTFE layer as reinforcement. The application of ePTFE layer can effectively improve membrane mechanical properties and reduce in-plane expansion during swelling [59].

Although pure chemical and pure mechanical degradation studies are sufficient in identifying membrane degradation mechanisms, they are limited in terms of representing the actual degradation process since chemical and mechanical mechanisms are simultaneously contributing in automotive fuel cell operation. Recently, more studies are focusing on combined chemical and mechanical degradation [16,60]; for instance, exclusive membrane crack formation has been observed without CL interaction under combined chemical and mechanical stress [16].

1.2.3. Thermal Degradation

The PFSA ionomer is able to remain chemically stable up to ~150°C due to the strength of C-F bonds [15]. Modern PEMFCs typically operating below 100°C are therefore unlikely to cause explicit thermal degradation of the membrane. However, if gas crossover is present due to other degradation mechanisms, there could be local hot spots experiencing accelerated degradation [61]. Thermal control such as applying coolant in fuel cell stack is an effective way to avoid membrane from direct expose to high temperature. In addition to degradation at high temperature, low temperature below 0°C could also pose an additional challenge to the membrane since water will be freezing. Studies have reported ionic conductivity and mechanical strength loss on PFSA membrane due to freeze/thaw cycling [62]. Purging with dry inert gas after shutting down the fuel cell is an effective way to remove water and prevent ice formation. It is also noteworthy that high temperature accelerates both chemical and mechanical degradation.

1.3. Accelerated Stress Testing

Laboratory scale *in situ* durability studies are typically carried out using accelerated stress testing (AST). AST is designed to generate degradation mechanisms and failure modes that are representative for the automotive fuel cell operation, but are produced in significantly shorter timeframes [46]. Two standard AST protocols for pure chemical and pure mechanical degradation of the membrane, respectively, are prescribed by the US DOE [63]. In brief, the chemical AST introduces chemical stressors through a steady-state open circuit voltage (OCV) hold at high temperature and low RH, while the mechanical AST involves RH cycling that creates dynamic mechanical

stresses. A durability study could focus on chemical or mechanical degradation applied separately, or jointly as combined chemical and mechanical degradation. Combined degradation is typically composed of OCV hold and RH cycling between dry and saturated gas [64]. Membrane failure in combined degradation is usually reached with reduced time compared to pure chemical or mechanical degradation [46].

1.4. Membrane Electrode Assembly Sealing Technique

While the operational conditions are a key contributor to fuel cell component degradation, MEA design and manufacturing process can also have a significant impact on cell performance and lifetime. As introduced earlier, CL could be either coated on the membrane forming catalyst coated membrane (CCM) composite, or on the GDLs forming gas diffusion electrodes (GDEs). Membrane (or CCM) is then sandwiched between GDEs (or GDLs), often aided by thermal compression, to produce an MEA. During assembly between the bipolar plates, the edge of the MEA needs to be adequately sealed in order to prevent (i) internal gas crossover between anode and cathode, referred to as internal leakage; and (ii) gas leakage to the surroundings, referred to as external leakage. To date, there are four types of sealing structures (Figure 9) commonly used in the automotive fuel cell industry, namely, PEM direct sealing, PEM-wrapped frame sealing, MEA-wrapped frame sealing, and rigid protective frame sealing [65]. The PEM direct sealing requires membrane to have larger dimensions than GDL in order to fully cover and separate anode and cathode. Additionally, sealing member such as rubber rings are applied on both anode and cathode side to close the edge [66,67]. The PEM direct sealing usually has simple design and is easy for realization. However, membrane (or CCM) beyond the sealing member is not active, thus causing material waste. Rigid protective frame sealing is similar to PEM direct sealing except that solid material frames such as polymer films are used instead of flexible gasket material. Frame is often coated with adhesive layer in order to completely close the edges [67,68]. Rigid frame usually has better protection of the MEA from over compression, but the membrane waste issue still exists. The frame sealing methods are commonly seen in lab scale research cells since they can be easily custom designed and are relatively easy for (dis)assembly. PEM or MEA wrapped sealing utilizes injection molding technique to inject the sealant around PEM or MEA [69,70]. In general, wrapped frame sealing has a better sealing performance over PEM

direct sealing and rigid frame sealing since sealant is more rigid and chemically stable. However, the processing temperature needs to be strictly controlled to prevent damage to fuel cell components. The wrapped frame sealing technique is more commonly used in serial production than in prototyping since it requires a mould and is less amenable to design change. Moreover, research cells, especially those intended for post mortem study, are not recommended for frame sealing since it is difficult for disassembly. Although numerous different sealing approaches are applied in MEA edge design, a reliable edge design should always provide good gas separation and mechanical stability. In contrast, poorly designed or manufactured MEA sealing structure can cause undesirable edge effects, such as gas leakage, mechanical stress concentration, and edge failure, which could have deleterious effects on fuel cell performance and/or durability. For instance, Sompalli et al. [71] showed that misaligned electrodes at MEA edges will significantly accelerate membrane degradation; however, degradation studies typically tend to focus on defects or damage in the main active area, while very limited literature reports have so far addressed the MEA edge effects.
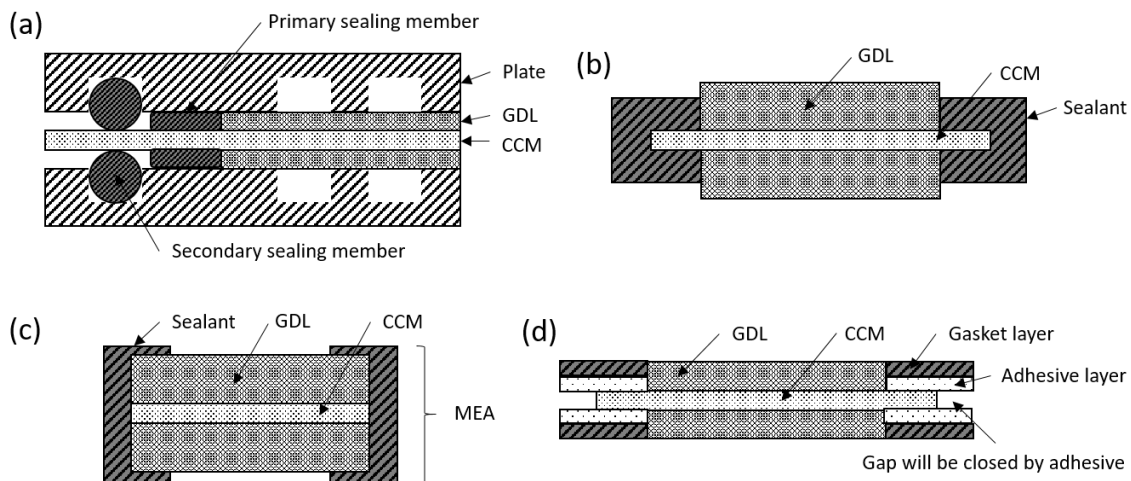
Figure 9: **Schematics of (a) PEM direct sealing, (b) PEM-wrapped sealing, (c) MEA-wrapped sealing, and (d) rigid frame sealing [65].**

1.5. X-ray Computed Tomography

1.5.1. Technological Background

X-ray computed tomography (XCT) is a promising non-destructive 3D imaging technique. X-ray, discovered by Wilhelm Röntgen in 1895, is a type of high energy

electromagnetic wave with extremely short wavelength generated by exposing metallic materials to high energy incident electrons. In metallic atoms, electrons occupy multiple orbitals differentiated by energy, with inner shell orbitals at low energy and outer shell orbitals at high energy. When an electron in the low energy orbitals gets dislodged by incident particle, another electron in the high energy orbitals will lose energy and replace the dislodged electron. During this process, part of the lost energy is emitted as X-ray photons. In modern XCT equipment, the X-ray source (tube) typically looks like the schematic demonstrated in Figure 10.
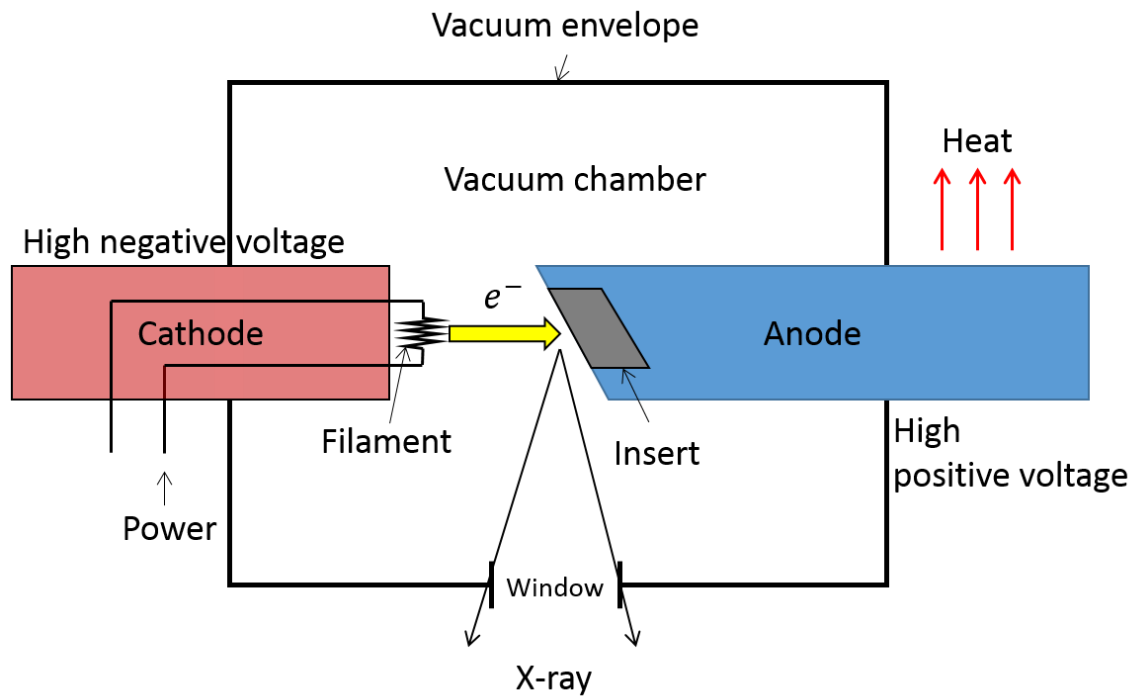
Figure 10:   Schematic of X-ray tube [72].

There are three major components in the X-ray tube: vacuum envelope, cathode with filament, and anode with insert. During operation, the filament is powered and heated to incandescence to generate electrons. The cathode and anode are held at high negative and positive voltage respectively so that electrons can be accelerated. In general, cathode potential is -10 to -500 kV [72] with respect to anode. The accelerated electrons then hit the metal insert on the anode, which releases X-ray photons. The anode metal insert is commonly made by tungsten alloy, and only ~1% of the energy released is converted into X-ray and the rest into heat [72]. As a result, the anode is made by materials with good thermal conductivity such as copper, and coolant may be needed to prevent melting. Both anode and cathode are enclosed in a vacuum envelope

which is commonly made by ceramic in order to prevent any obstruction along the electron pathway.

An X-ray photon has strong penetrability due to its high energy. Therefore, some opaque materials to visible light are transparent to X-ray. However, X-ray does attenuate when penetrating through materials, which is the key property to make X-ray imaging feasible. When a parallel X-ray beam penetrates through a sample, transmitted irradiance can be expressed by the following equation:

$$\Phi^E = \Phi_0^E e^{-\mu y} \tag{14}$$

In Equation 14, Φ_0^E and Φ^E are the irradiance of incoming and transmitted X-ray beams respectively; μ is the linear attenuation coefficient, which is a function of beam energy, atomic number, and mass density; and y is the material thickness along the X-ray direction. Physically, the attenuated X-ray is either absorbed or scattered by sample material at low energy range (below 1.02 MeV) [72]. Transmitted X-ray beam is then collected by a detector with scintillator materials and a 2D radiograph can be generated, which is basically an X-ray attenuation map. To obtain a 3D tomography, multiple 2D radiograph acquisitions are needed across 180 or full 360 degree rotation. The 2D radiograph dataset can then be converted into a single 3D virtual stack through a digital reconstruction process.

1.5.2. Application in Fuel Cell Study

Before the potential of XCT was realized, MEA visualization was typically carried out by SEM. Previous studies based on SEM imaging technique have discovered membrane cracks due to mechanical degradation [73], membrane thinning due to chemical degradation [46], and round membrane pinhole formation under combined chemical and mechanical degradation [60]. Additionally, SEM studies of catalyst layer cracks were also carried out in CCMs [54]. SEM imaging, however, is limited to 2D *ex situ* surface visualization of specimens in vacuum chamber, which is often insufficient to fully resolve the dynamic degradation processes associated with the 3D structure of the MEA. Besides, cross-sectional visualization needs the sample to be cut and embedded into epoxy, and the surface is then grinded and polished [74]. Such preparation procedure is destructive in nature and may bring additional artefacts to the specimen,

thus compromising reliability in morphological degradation study. To overcome the shortcomings of SEM, XCT has been gaining popularity owing to its non-destructive 3D visualization capability. In the early stage of XCT adoption, the major focus was on *ex situ* analysis of the structures of CLs [75,76] and GDLs/MPLs [77–79]. As introduced before, since CL and GDL are both porous media, the application of 3D image analysis can obtain properties such as porosity, tortuosity, and diffusivity. Furthermore, numerical simulation can be carried out based on the 3D model obtained from XCT. In more recent studies, *in situ* visualization technique was developed, where the entire MEA is visualized in assembled state. Each individual MEA component can then be virtually separated by image processing software such as ImageJ [80], according to their different X-ray absorption rate. 3D *in situ* visualization is mainly utilized in degradation [16,44,81,82] and water distribution studies [83,84]. Combining XCT image and electrochemical diagnostics data, performance loss can be directly linked to morphological changes. A major advantage of *in situ* degradation study is that the interaction between membrane, CL, and GDL can be captured. In addition, the simultaneous access to both planar and cross-sectional views can yield better understanding to the reasons of deformation features. Water distribution study is usually accompanied with *operando* visualization, since the fuel cell needs to run at certain current in order to produce water. Water distribution, accumulation, and transport can be captured by XCT. However, one notable limitation of 3D *in situ* visualization is that the evolution of degradation sometimes remains unclear with BOL and end-of-life (EOL) image analysis only. To overcome this, a novel technique referred to as 4D *in situ* visualization has recently been developed [52,85,86]. 4D visualization is based on three spatial dimensions plus one time dimension. During the experiment, the MEA is scanned and subjected to AST alternately, and the image location is kept the same from BOL until EOL, allowing the evolution of degradation to be tracked. So far, the SFU Fuel Cell Research Lab (FCReL) has successfully carried out 4D *in situ* membrane degradation studies under pure mechanical AST and pure chemical AST using a custom designed small scale fuel cell fixture (SSF) that is compatible with the existing ZEISS Xradia® 520 Versa micro XCT system. It was found in 4D pure mechanical AST study that MEA defects such as electrode cracks and membrane-electrode delamination at BOL are the root cause of fatigue-driven membrane cracks, and the membrane cracks propagate faster in the later degradation stage [52]. On the other hand, electrode shorting driven by

18

locally amplified membrane thinning is the key MEA failure mode in 4D pure chemical AST study [87].

1.6. Objectives

The primary goal of this work is to understand the fundamentals and root cause of combined chemical and mechanical fuel cell membrane degradation in both active area and edge regions. Although combined chemical and mechanical membrane degradation has been researched using post mortem image analysis techniques in many studies, there is still lack of knowledge in the evolution of membrane degradation. Besides, there is also limited knowledge addressing the mechanisms of edge failure in the literature. However, membrane failure in poorly designed edges can lead to premature cell failures as well as reduced durability. These gaps are addressed in this work using the 4D *in situ* XCT visualization technique, which enables same location image acquisition for both active area and edge regions over time. This work focuses on rigid frame sealing which is commonly used for research scale fuel cell experimentation and testing, including accelerated stress tests. For the experimental stream of this work, a subsequent edge design equipped with suitable mitigations is first proposed based on preliminary findings from the original design. The subsequent design is then subjected to the same combined chemical and mechanical AST with 4D *in situ* visualization and diagnostic methods to verify and demonstrate the efficacy of implemented mitigations. The motivation is to increase the robustness of edge design of the small scale MEA that is typically utilized in 4D *in situ* visualization studies. With the robust edge design, early chemical or mechanical membrane failures can be eliminated such that studies focusing on damage occurring within the active MEA area could be effectively pursued toward enhanced overall fuel cell durability.

Chapter 2.   Experimental

2.1. Membrane Electrode Assembly Preparation

All MEAs used in this work were composed of CCM with Dupont Nafion® NR211 non-reinforced PFSA ionomer membrane, GDLs, polyimide Kapton® adhesive sheet, and PTFE Teflon® sheet. The CCM was fabricated using a high CCL crack density half CCM [86] designed for research scale membrane degradation studies. The ACL was applied on the membrane side of the half CCM through decal transfer at 150°C and 15 bar for 180 seconds. The Pt loading was 0.1 and 0.4 $\mathrm{mg/cm^2}$ for ACL and CCL respectively with 50:50 Pt/C ratio. The GDLs were composed of teflonated Avcarb® non-woven carbon paper with MPL coated on one side. Two different customized MEA designs were developed in this work to perform XCT imaging using the existing small scale fixture developed by FCReL. In both MEA designs, the MEA was manually assembled without hot pressing by sandwiching a piece of CCM between two GDLs, with the MPL side facing the CCM. The CCM was rigid frame sealed by 80 μm thick Kapton® polyimide adhesive film as the primary gasket to prevent leakage. PTFE Teflon® sheets with 75 μm thickness were applied on both sides as secondary gasket layer to control overall MEA thickness and compression. The customized small scale fuel cell was designed to minimize X-ray attenuation and optimize XCT image quality. It was composed of two main parts: MEA and flow field plates. Both fuel cell designs to be presented later shared the same MEA and flow field plate design but had different MEA dimensions and frame designs, where MEA edge design 2 was refined from the originally developed MEA edge design 1. The flow field plates used in this work were CNC machined compressed graphite with cured resin. Graphite was chosen as the plate material for its good electrical conductivity and X-ray transparency. As indicated in Figure 11, the hourglass shaped graphite plate had 10 x 30 $\mathrm{mm^2}$ outer dimensions with cylindrical neck having diameter of 6 mm in the middle. The purpose of this necked design was to reduce X-ray attenuation from non-MEA components such that high signal-to-noise ratio could be achieved with minimum X-ray exposure time. Two parallel cylindrical shaped straight flow channels with 1 mm diameter and 11 mm length were located at the centre of the plate, separated by a 0.25 mm wide landing. Parallel co-flow gases were supplied to anode and cathode. Rectangular shaped slots were cut on the

top and bottom edges of the flow plate, and 3D printed alignment blocks were placed inside the slots for alignment of the other plate. Laser micromachined indentations were created on the Kapton® and/or Teflon® gasket layers to ensure MEA alignment inside the plates.

2.1.1. MEA Edge Design 1

The original MEA edge design (design 1) illustrated in Figure 11 was inspired by rigid frame sealing technique, and has a nominal active area of 3 x 5 mm^2, which is the dimension of the central window in the Kapton® sheets. For assembly procedure, a piece of Kapton® with adhesive side facing up was first placed on 10 x 30 mm^2 vacuum plate with female alignment feature, while CCM was placed on 4 x 7 mm^2 vacuum plate with male alignment feature as indicated in Figure 12. The two vacuum plates were then clamped together with vacuum enabled so that the CCM was placed at the center of the Kapton® sheet. Next, the other Kapton® sheet placed on 10 x 30 mm^2 vacuum plate with male alignment feature was clamped with the previous Kapton® sheet to form a Kapton®-CCM sub-assembly. The CCM was larger than the Kapton® window so that its periphery could be sealed by adhesive to prevent internal gas crossover. This sub-assembly was then compressed between the two graphite plates together with Teflon® sheets and GDLs on both sides. Teflon® window and GDLs were cut to 4 x 5 mm^2 to enable a 0.5 mm wide overlap over the lateral edges of the Kapton® gasket layers, such that any CCM regions that were unsupported by GDL due to GDL-Teflon® alignment offset were minimized. However, the lateral edges of the GDLs in the overlap region would experience over compression, as indicated in Figure 11(c). Due to its location outside the active area, this over compression is unlikely to affect cell performance or durability. The outer dimensions of both gasket layers were 10 x 30 mm^2 which was consistent with the graphite plates. Detailed dimensions of each MEA component can also be found in Table 1. All MEA components were cut with high precision IPG® photonics laser micromachining system. Detailed laser cut settings are given in Table 2. Laser beam is in rectangular shape and its dimensions are represented by the beam size. Energy and attenuator together control the laser beam, whereas the frequency represents the number of laser shots per second. Pulse rate sets the distance travelled between two consecutive laser shots and pass defines how many times the pre-determined path is etched.
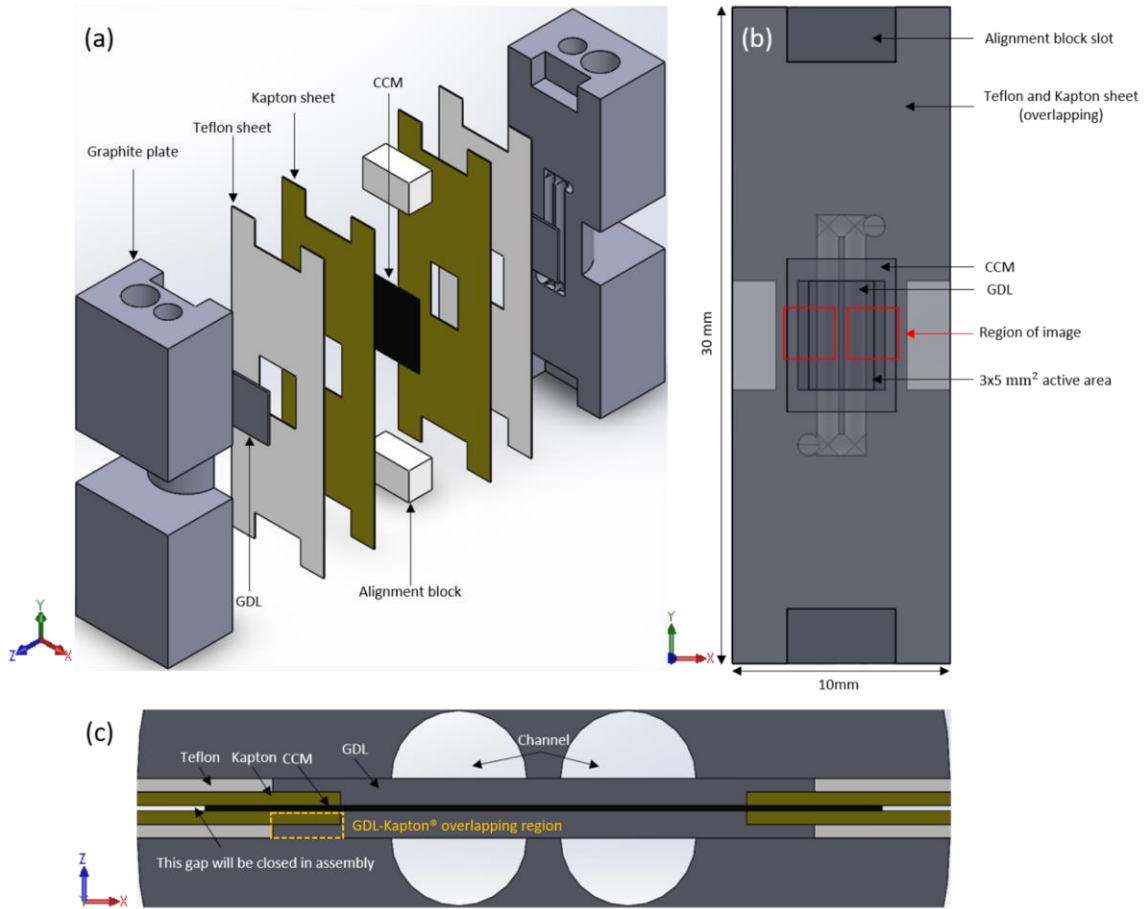
Figure 11: MEA edge design 1: (a) 3D exploded view; (b) planar view; and (c) cross-sectional view.
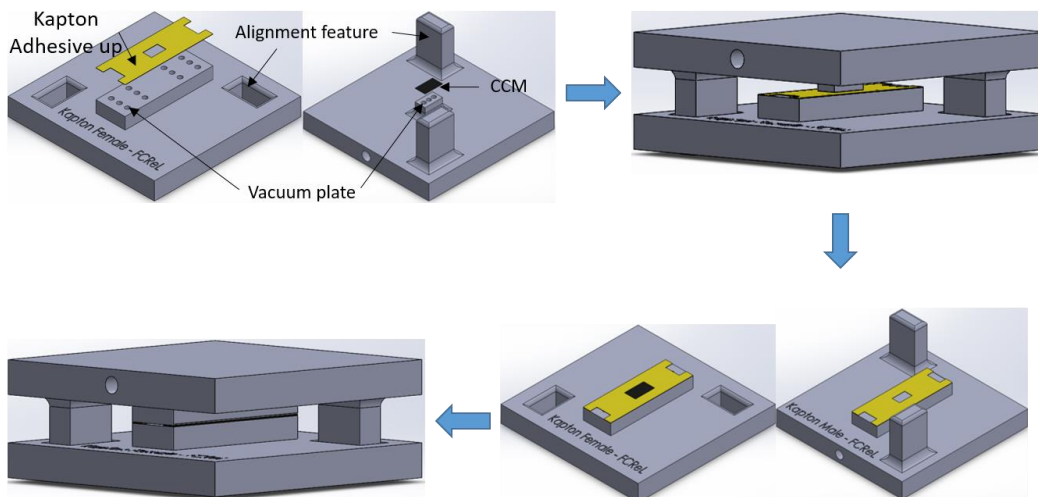
Figure 12: Kapton®-CCM sub-assembly assembly procedure and setup.

2.1.2. MEA Edge Design 2

The second MEA edge design (design 2) shown in Figure 13 still used rigid frame sealing technique, but with a larger nominal active area of 4 x 13 mm^2. The key difference in comparison to design 1 is that the Teflon® layer is inserted into the Kapton®-CCM sub-assembly, thus forming a Kapton®-Teflon®-CCM sub-assembly wherein the Teflon® interfaces with the CCM. In this design, Kapton® adhesive sheet was first attached to Teflon® sheet and then laser cut together with the Teflon® sheet facing the laser beam. Two cuts were needed in this scenario, one for Teflon® outline that only cuts through Teflon® sheet and the other for window at the center that needs both Teflon® and Kapton® sheets to be penetrated. Teflon® outline with 6 x 16 mm^2 was cut using higher pulse rate (Table 2) so that Kapton® sheet beneath it remained unharmed. In contrast, the window was cut using lower pulse rate and additional passes. This modification in gasket layers reduced the number of components from five in design 1 (Kapton-CCM sub-assembly, two Teflon® sheets, and two GDLs) to three in design 2 (Kapton®-Teflon®-CCM sub-assembly and two GDLs) during final assembly, which simplified the assembly and improved alignment accuracy. Moreover, the alignment of Kapton® and Teflon® windows was nearly perfect since they were created during the same cut. Whereas the windows in design 1 were more prone to handling related misalignment during assembly. Another modification was the longitudinal dimension of GDL. With 4 x 13 mm^2 GDL and window size, the active area was increased with the GDL covering the entire flow channel including inlet and outlet mixing chambers. This coverage differed from the 3 x 5 mm^2 active area of design 1 wherein the gasket region partially overlaps the flow channel, which could introduce certain undesirable deformations in the flow channels that are discussed later. Detailed dimensions of each MEA component can be found in Table 1 as well.
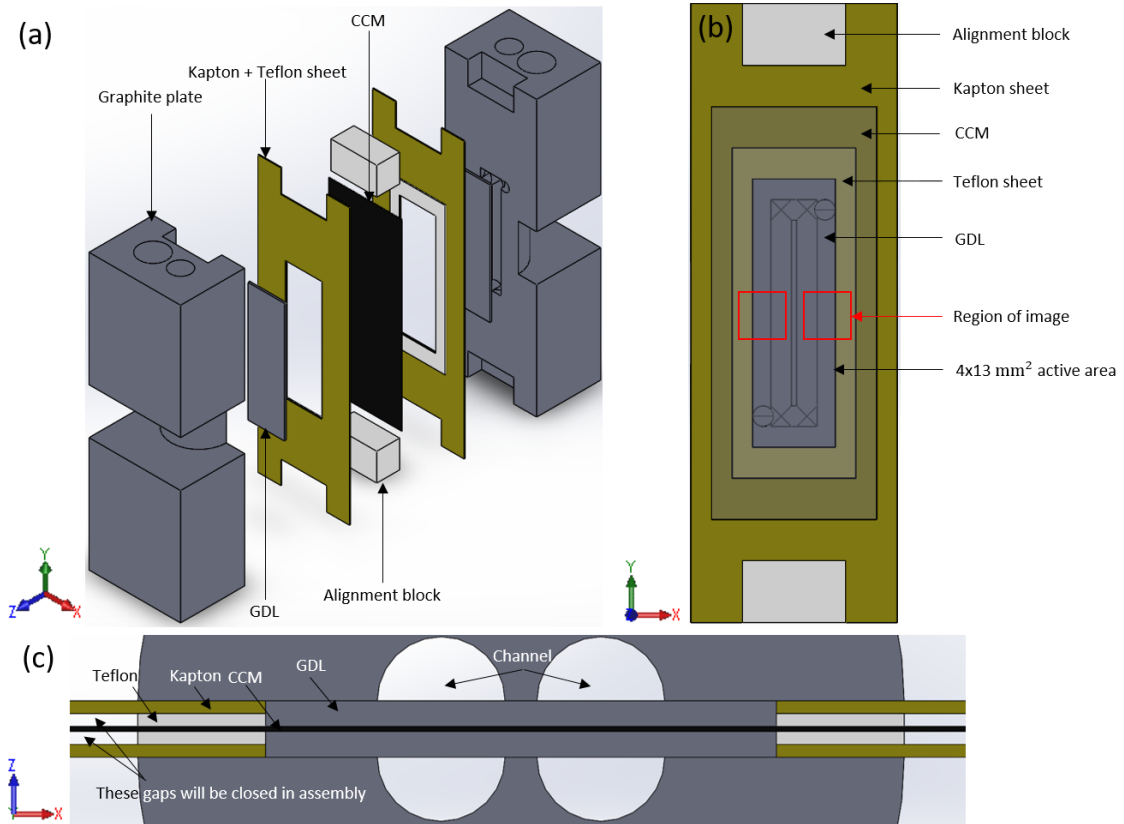
Figure 13:   MEA edge design 2: (a) 3D exploded view; (b) planar view; and (c) cross-sectionalal view.

Table 1:   MEA component dimensions

| | Dimension [mm x mm] | | | |
	Kapton	Teflon	GDL	CCM
Design 1	Outer 10x30 Inner 3x5	Outer 10x30 Inner 4x5	4x5	4x7
Design 2	Outer 10x30 Inner 4x13	Outer 6x16 Inner 4x13	4x13	8x20

Table 2:   Laser cut settings

Material	Beam Energy [mJ]	Frequency [Hz]	Pulse [µm/shot]	Pass	Attenuator [°]	Beam Size [µm x µm]
Teflon®	3	950	0.5	1	70	
Kapton®	3.5	950	0.6	1	90	
GDL	4	800	0.6	3	80	
CCM	4	800	0.6	1	60	25 x 25
Kapton-Teflon (both)	3	900	0.2	2	80	
Kapton-Teflon (Teflon only)	3	900	0.6	1	80	

2.2. Fuel Cell Testing Hardware

In order to facilitate joint testing and visualization of miniaturized fuel cells, the Fuel Cell Research Lab has developed a unique small scale fixture (SSF) to hold the MEA so that it is compatible with the fuel cell test station and more importantly, the micro XCT system. Figure 14 shows both assembled and exploded view of the SSF. The graphite flow field plates are held by two pairs of plastic clamp parts with blue pair at the top and red pair at the bottom. Each pair of the round shaped plastic clamps is tightened by a metal hose clamp. The neck region of the graphite plate is exposed to the surrounding in order to minimize xX-ray attenuation during CT scan. The base can be divided into two portions: (i) a hollow cylinder at the top and (ii) a major arc shaped base at the bottom. The hollow cylinder is to adjust overall height of the entire fixture to align it with the X-ray source and detector. The base was designed to match the shape of the rotating stage with a slot for additional clamp attachment to the platform. The front opening on the base allows electrical wires and outlet tubes to be extended out of the fixture and get connected to the test station. Inlet tubes are inserted in inlet holes on top of the graphite plates, and are connected to the gas supply of test station.
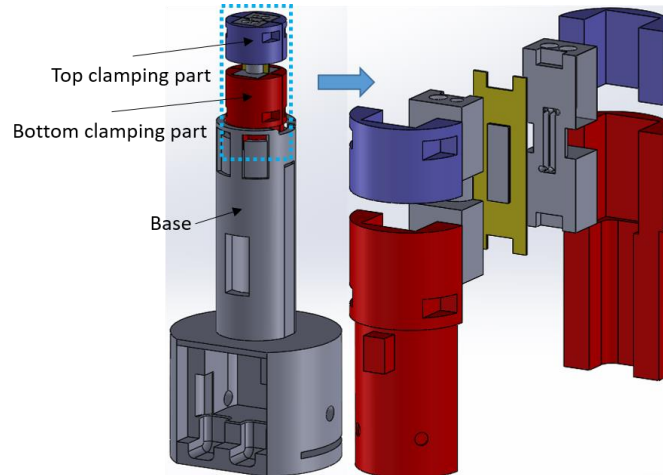
Figure 14:   **3D CAD model of the small scale fixture developed for joint testing and visualization of a fuel cell.**

Fuel cell operation and testing requires precise control of temperature, relative humidity (RH), gas flow rate, and pressure. It is also important to monitor cell voltage and current during the testing period if applicable. In this work, fuel cell testing can run for up to 120 consecutive hours. As a result, the system needs to be automated and various alarms need to be in place to shut off the system in case of any emergency. As

indicated in Figure 15, a Greenlight Innovation® fully automated G20 fuel cell test station (G20) was used to carry out the testing part of this work. The G20 test station is equipped with flow rate control, back pressure control, dew point temperature control, and inlet gas temperature control. It also allows two extra heaters to be connected and controlled through thermal couples (TC). The SSF was connected to the test station as illustrated in Figure 15(b). The anode and cathode inlet tubes coming out of the station were wrapped with heating tape and insulation materials, therefore allowing gas to be continuously heated after passing the humidifier. A TC was placed at the end of the inlet tube to control inlet gas temperature. As indicated in Figure 15(c), the connection tube from test station to SSF was reduced to critical length to minimize heat loss. A cartridge heater was plugged into the anode plate in order to maintain certain cell temperature. A TC was hooked up with the cartridge heater to feedback its temperature to the test station which closes the control loop. Another TC was placed in the cathode plate to monitor the actual cell temperature. For the present work, anode gas can be switched between pure hydrogen and pure nitrogen while cathode gas can be switched between air and pure nitrogen. In both lines, gas can also bypass the humidifier, which provides the feasibility of RH cycling between wet and dry phases. Fuel cell performance can be measured as well by applying the built-in load bank of the G20 station. In addition, a Gamry® Interface 5000E potentiostat was used in this work as a function generator to conduct *in situ* electrochemical fuel cell diagnostics.
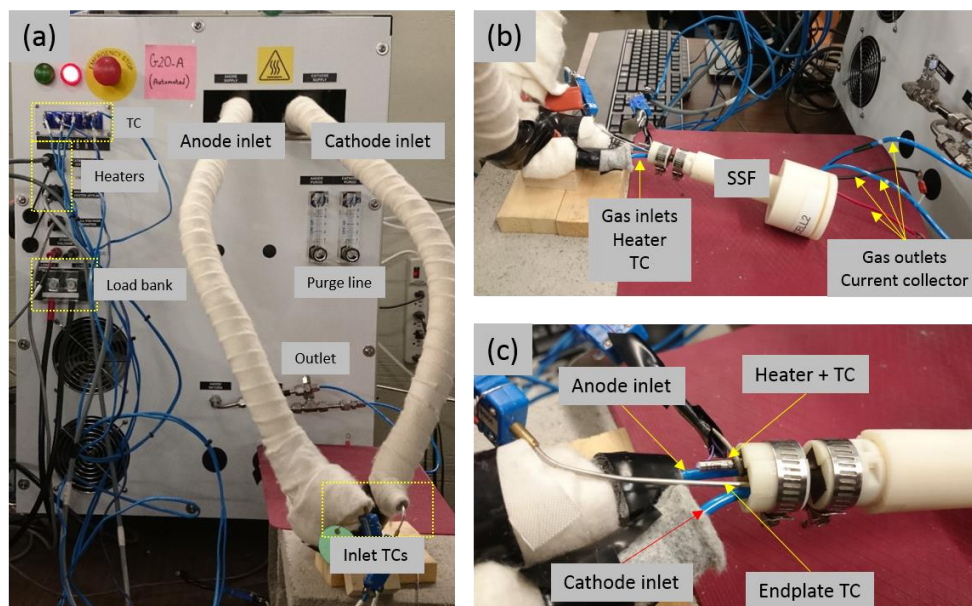
Figure 15: (a) Greenlight Innovation G20 fuel cell test station; (b) SSF connection; (c) SSF inlet close-up.

2.3. Accelerated Stress Test Protocol

During automotive fuel cell operation, both chemical and mechanical stressors act synergistically on the membrane to induce its degradation. In the present work, an accelerated stress test (AST) protocol that applies elevated levels of both chemical and mechanical stressors on the examined small scale MEA is utilized to produce accelerated membrane degradation and failure. This protocol is hereafter referred to as the alternating chemo-mechanical AST. One complete combined AST cycle consists of chemical degradation phase that is 20 hours of steady-state OCV hold followed by mechanical degradation phase which is 10 repeated RH cycles. The cell temperature is maintained at 75°C throughout. In the OCV hold phase, high temperature, low humidity hydrogen and air is flowed to the anode and cathode respectively in order to generate rapid chemical membrane degradation. During this phase, the cell is operated with a 15 kPa overpressure on the anode side to push any convective hydrogen crossover to the cathode side in case internal leakage happens. In each RH cycle, the cell is first humidified for 3 minutes by flowing over saturated nitrogen gas through both anode and cathode, followed by 17 minutes dehydration using dry nitrogen that bypasses the humidifier system. It is noticeable that chemical degradation phase requires low humidity, so the dew point is controlled at 60°C, but RH cycling requires oversaturated gas, so that dew point is set to 85°C. The heating procedure is gradual, and during this process gas with increasing RH is continuously flowed into the cell. As a result, the very first wet cycle is done by 10 minutes heating. Such cyclic hydration and dehydration process is intended to introduce cyclic mechanical stress in the membrane through its repeated constrained swelling and shrinkage, which facilitates the mechanical degradation. Detailed settings of the AST protocol can be found in Table 3. The fully automated Greenlight Innovation® G20 fuel cell test station introduced in the previous section was used to execute the chosen AST protocol with repeated alternating chemo-mechanical phases until the MEA reaches ultimate membrane failure, which is characterized by 20% OCV loss from the BOL or 30 mV OCV loss at 15 kPa anode overpressure (indicative of internal gas leakage), whichever is reached first.

Table 3:   Alternating chemical and mechanical AST protocol.

	Chemical Degradation	Mechanical Degradation
Test condition	Steady state OCV for 20 hours	10 cycles Wet: 3 mins @150% RH (First wet phase is achieved by 10 min warm up) Dry: 17 mins @0% RH
Cell temperature	Gas inlet temperature = 95 °C	Gas inlet temperature = 95 °C
Cell RH	51% RH	Wet: 150% RH Dry: 0% RH
Fuel/Oxidant	Anode: H2 at 0.1 slpm Cathode: Air at 0.2 slpm	Anode: N2 at 0.5 slpm Cathode: N2 at 0.5 slpm
Gas pressure	Anode inlet = 15 kPa (back pressure controlled)	No back pressure control

2.4. Fuel Cell Conditioning

All small scale fuel cells will first go through leak tests and conditioning before being subjected to AST. Leak tests include both external leak test and internal leak test. External leak test was conducted on dead-ended anode and cathode outlets with air flowing in through both inlets. The cell was considered to be free from any external leak if escaping air was not detected from anywhere around the cell after submerging the entire fixture in water for 2 minutes. Internal leak test was done by sealing one outlet (either anode or cathode) and flowing air from the same side's inlet. An internal leak free cell was confirmed separately for both anode and cathode sides, provided that no escaping air was detected opposite to the sealed electrode side. After both internal and external leak detection test, the leak tight cell was then connected to the fuel cell test station for conditioning. Conditioning was performed by first applying at least 40 repeated cycles of cyclic voltammetry (CV) with hydrogen/nitrogen flowing to anode/cathode at flow rate of 0.2/0.4 slpm, sweeping between 0.1 to 1 V at a scan rate of 0.05 V/s. During the CV sweep, the platinum surface is reconstructed into crystalline structure through cyclic oxidation and reduction reactions. As more platinum gets reconstructed into crystalline structure, several distinguishable peaks appear in the hydrogen desorption region at low potential; ideally, three peaks will appear that correspond to three different crystalline structures, though sometimes only two of them were visible and distinguishable. The CV sweep was followed by five cycles of air starvation. In each air starvation cycle, hydrogen and air was initially flowed to anode

and cathode at 0.2/0.4 slpm flow rate for 2 minutes, allowing the cell to reach a stable OCV. Cathode air was then switched to nitrogen to create an air starved environment that leads to OCV drop. Air was switched back once the OCV dropped to 0.2 V, which completes a full air starvation cycle. The air starvation phase reduces the platinum oxide back to platinum, and therefore increases the total amount of available platinum catalyst that improves overall cell performance. As the final step of conditioning, 20 hours of steady state medium current density (around 500 mA/cm^2) operation was performed at 75 °C and 100% RH with hydrogen and air flowing to anode and cathode at 0.2/0.4 slpm flow rate. The purpose of steady state operation is to condition the ionomer phase in the membrane and CLs as well as opening up water channels in the ionomer phase. At high temperature and high RH, the membrane ionomer becomes softer and fills the interfacial gaps between membrane and catalyst layer. The entire steady state operation is conducted with current generation to prevent degradation from high voltage and produce water for humidification.

2.5. Fuel Cell Recovery

In the fuel cell degradation process, some degradation modes are irreversible and cause permanent damage, such as catalyst dissolution, membrane thinning, and carbon corrosion. These modes need systematic investigation and preventative mitigation. However, other degradation modes are reversible and can be recovered by applying certain recovery procedures. Typical reversible modes include flooding, dryout, fuel starvation, benign voltage reversal, and certain gas impurity. In order to minimize the influence of reversible losses, and focus the analysis on irreversible degradation, it is recommended to run a recovery procedure after AST and before diagnostics. The US DOE has developed a recovery protocol which was adopted for this work by adjusting the flow rate for the small scale cell, as indicated in Table 4. In addition to the US DOE protocol, three CV cycles using the conditioning CV protocol were also conducted as part of the recovery. During the entire recovery procedure, the cell was maintained at 70°C and 100% RH.

Table 4:   Recovery steps

Step	Step Name	Anode gas	Anode flow rate [slpm]	Cathode gas	Cathode flow rate [slpm]	Duration [s]
1	N_2 soak	N_2	0.3	N_2	0.5	300
2	Air soak	N/A	0	Air	0.5	900
3	N_2 soak	N_2	0.3	N_2	0.5	120
4	H_2 soak	H_2	0.3	N/A	0	600
5	H_2-air back on	H_2	0.3	Air	0.5	5

2.6.   *In situ* Electrochemical Diagnostics

In situ electrochemical diagnostics is an effective way to examine fuel cell performance and degradation from AST without disassembling the fuel cell. In the present work, *in situ* diagnostics was performed at BOL after conditioning and repeated after every five chemo-mechanical AST cycles until EOL was reached. Diagnostic techniques applied in this work include polarization curve measurement, CV, electrochemical impedance spectroscopy (EIS), and electrochemical leak detection test (ELDT). All *in situ* diagnostics were performed at 75 °C and 100% RH. Detailed settings regarding anode and cathode gas flows for each diagnostic technique can be found in Table 5.

Table 5:   Diagnostics gas flow

Diagnostic Technique	Anode Gas	Anode Flow Rate [slpm]	Cathode Gas	Cathode Flow Rate [slpm]
Polarization Curve	H_2	0.2	Air	0.5
CV	H_2	0.2	N_2	0.5
EIS	H_2	0.2	N_2	0.5
ELDT	H_2	0.2	Air	0.5

2.6.1. Polarization Curve

The fuel cell polarization curve, also known as I-V curve, shows the relationship between cell voltage and cell current. It is a standard figure for fuel cell performance evaluation. Prior to each polarization curve measurement, five cycles of air starvation were applied to eliminate reversible cell performance loss. Polarization curve measurement was started with an OCV measurement followed by adding 0.01 A in steps and measuring the cell voltage response after 1 minute holding time. The measurement was stopped once the voltage dropped below 0.2 V. Figure 16 is an example of a typical

polarization curve. The curve can be divided into three regions (region 1, 2, and 3). In region 1 with low current density, the losses are dominated by the activation over potential, which is the potential required to overcome the activation energy of fuel cell electrochemical reaction on platinum surface. It represents the voltage required to initiate fuel cell reaction. In region 2 with moderate current density, the losses are dominated by ohmic loss, which is due to the resistance of electrical and ionic conduction through all fuel cell components including PEM, CLs, GDLs, flow plates, external circuit, and their interconnecting contact resistance. The polarization curve generally follows a linear pattern in this region, which can be explained by Ohm's law. In region 3 with high current density, the losses are dominated by mass transport loss, which is due to the limitation of reactant transport rate. Although the polarization curve is usually divided into three regions for analysis and each region is dominated by one type of loss, all three types of losses are contributing through the entire polarization curve.
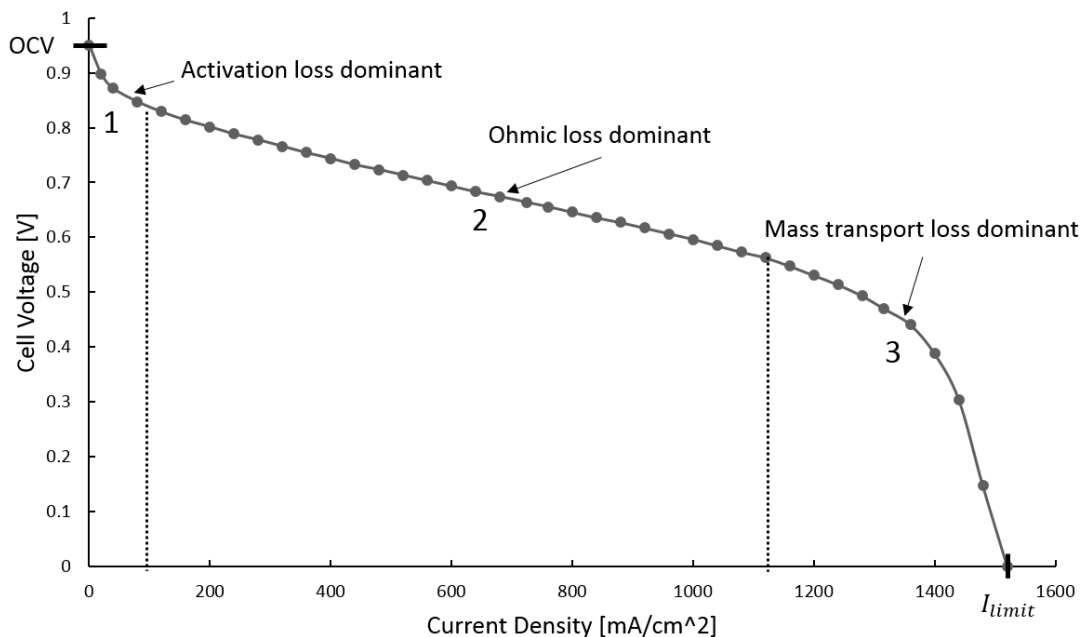
Figure 16: **Sample polarization curve.**

2.6.2. Cyclic Voltammetry

Cyclic voltammetry (CV) is an electrochemical technique that is commonly used for electrode characterization. In CV measurement, a forward and reverse linear voltage sweep between low potential and high potential at designated sweep rate is applied to the electrode of interest. During the voltage sweep, current will be generated due to

31

electrochemical surface reaction. Therefore, a current versus potential plot can be obtained which is referred to as a voltammogram. The voltammogram can be used in fuel cell diagnostics and for determining fuel cell performance parameters such as effective platinum surface area (EPSA) and double layer capacitance (C_{dl}). A Gamry® Interface 5000E potentiostat was used to carry out the CV measurement in this work. The voltage was swept from 0.05 V to 0.8 V with a constant sweep rate of 50 mV/s, generating a triangular wave function. Gas flow during CV sweep is indicated in Table 5. In fuel cell reaction, the ORR on cathode side is slower and critical. Therefore, the CV measurement was performed with respect to cathode. In this case, the working and sense electrodes of the potentiostat were connected to cathode and the counter and reference electrodes were connected to anode. Figure 17 shows an example of voltammogram obtained in this study.
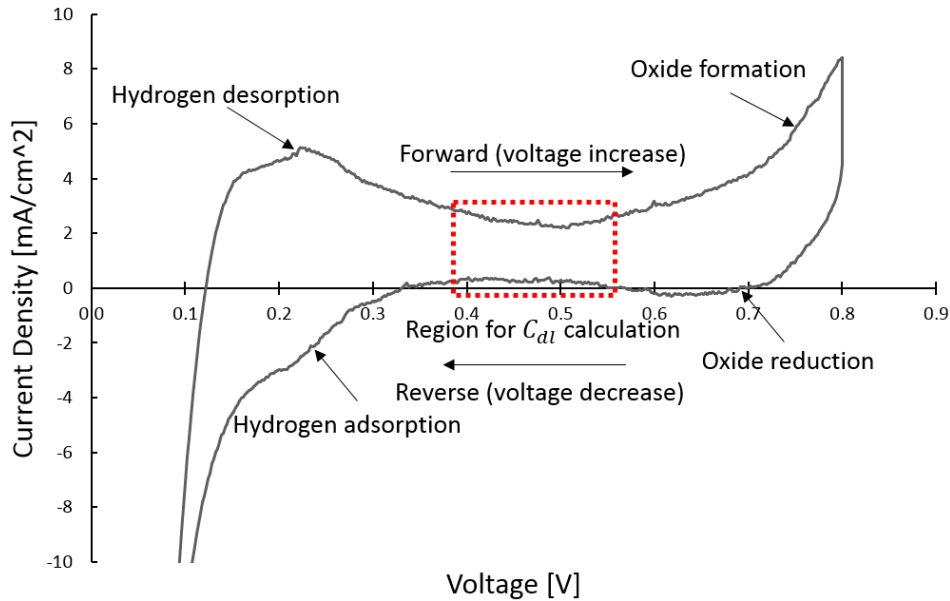
Figure 17:   Sample CV curve.

As indicated in Figure 17, there is a peak in the low potential region of the forward scan that represents hydrogen desorption. In this low potential range, the following electrochemical reaction takes place on platinum surface which generates the current [5]:

$$Pt - H + H_2O \rightarrow Pt + H_3O^+ + e^- \tag{15}$$
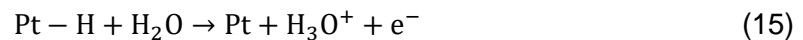
Hydrogen adsorption reaction happens on the reverse scan and the reverse reaction of Equation 15 takes place. In some cases, more than one peak can be

observed in the hydrogen desorption region, which is due to the different platinum crystallographic structures. However, the multiple peaks are not well distinguishable within the present cell. EPSA can be calculated by the following expression:

$$\text{EPSA} = \frac{\int I(t)dt}{SC} \tag{16}$$

The proportionality constant S for platinum is 210 $\mu C/cm^2$ and C is the platinum loading of catalyst layer. The catalyst used in this work has an area specific platinum loading of 0.4 mg/cm^2, thus C is 0.208 mg with cell active area being 0.52 cm^2. In Equation 16, the integration of current with respect to time represents the total charge generated from hydrogen desorption reaction. It is also common to introduce carbon monoxide (CO) and use CO peak to determine EPSA. Since the voltammogram is a current versus potential plot and the scan rate is known, the total charge can be determined using the alternative equation, where r is the scan rate at 0.05 V/s:

$$\int I(t)dt = \int \frac{I(v)}{r} dv \tag{17}$$

Therefore, the final EPSA expression can be written in the following form with the unit of [m^2/g Pt]:

$$\text{EPSA} = \frac{\int I(v)dv}{rSC} \tag{18}$$

In the present work, the integration part of the EPSA calculation was conducted using Gamry® Echem Analyst software, as indicated in Figure 18. In the case of using hydrogen desorption peak for integration, first, the lowest current point on the forward scan was identified. Then, a horizontal line parallel to the voltage axis was drawn passing through the lowest current point as the integration baseline. After the baseline is defined, total charge was obtained using the "integrate" built-in function.
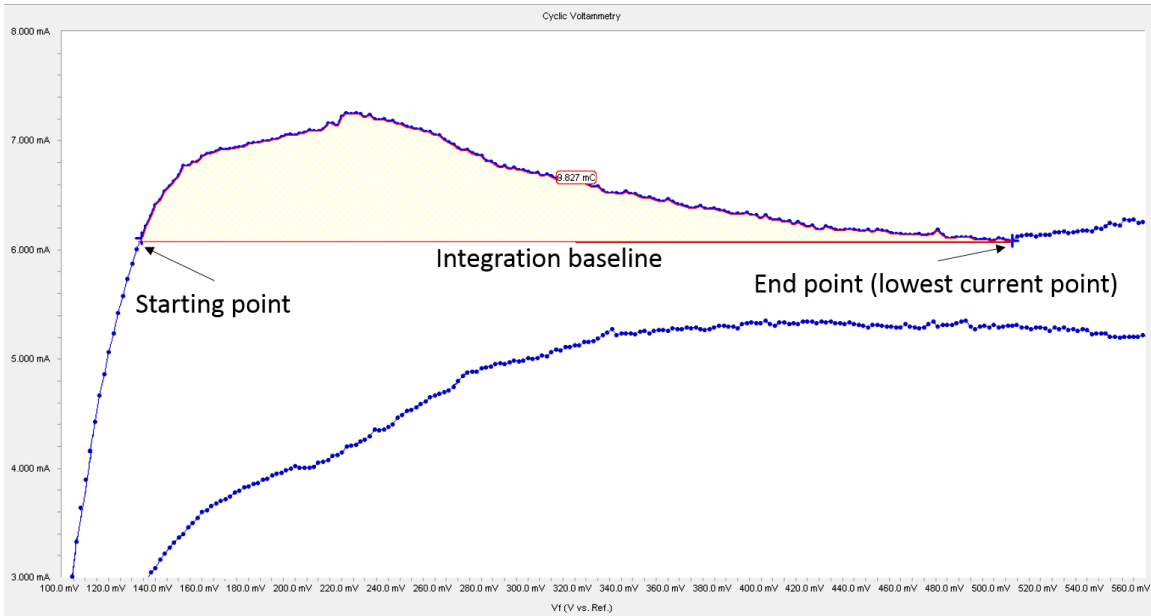
Figure 18: EPSA integration via hydrogen desorption peak.

Double layer capacitance can be obtained through the capacitive region in the intermediate potential range indicated by the red rectangle in Figure 17. Current in this region is the exchange current from charging and discharging of the double layer, which can be treated as a capacitor. The double layer charging current can be calculated from the following equation:

$$i_{dl} = \frac{i_1 - i_2}{2}$$ (19)

In Equation 19, i_1 is the current density of the forward (charging) scan and i_2 is the current density of the reverse (discharging) scan (Figure 19). Double layer capacitance can then be determined by:

$$C_{dl} = \frac{i_{dl}}{r}$$ (20)
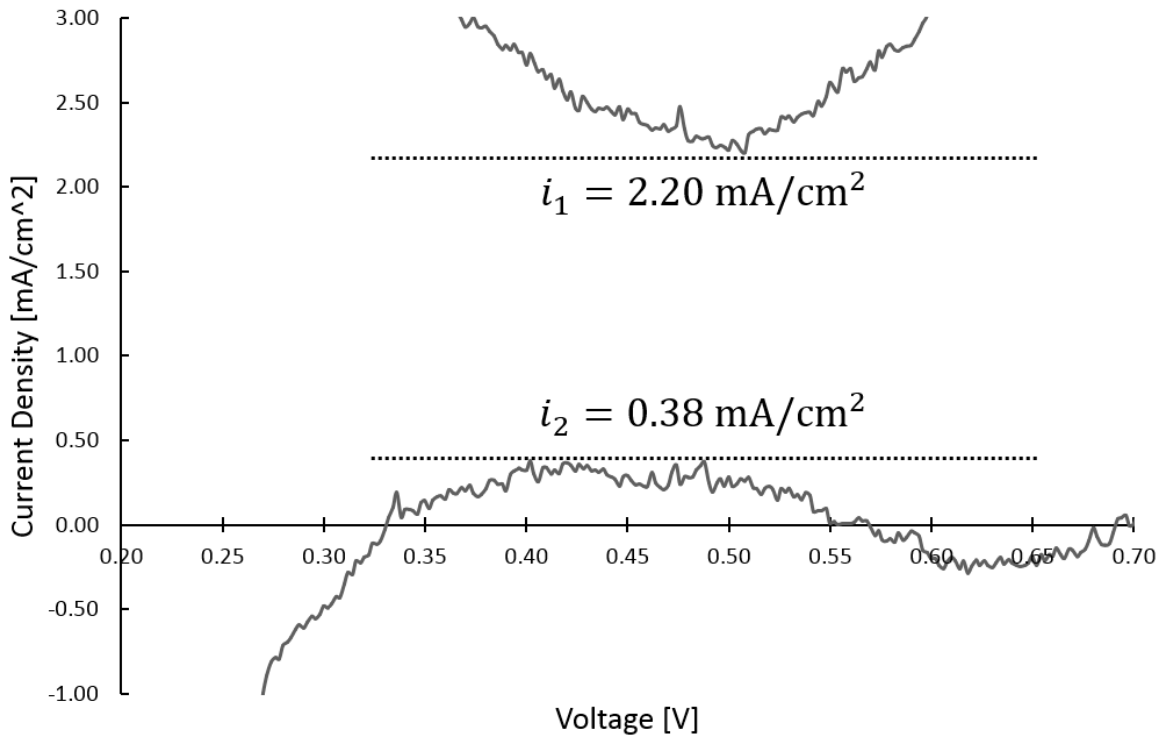
Figure 19: Obtaining exchange current from CV curve.

The electrical double layer will be introduced in more detail in the next section since double layer capacitance can be determined from EIS as well. In addition to EPSA and double layer capacitance, the voltammogram can also be used in detecting internal shorting of the MEA. Theoretically, the PEM should be electron resistive so that current is forced to go through the external circuit. However, if localized contact between ACL and CCL exists, there will be internal shorting. As a result, a cell with internal shorting behaves more like a resistor rather than a capacitor and extra current will be generated during CV sweep when the cell potential changes. As a result, the voltammogram will look tilted, as Figure 20 shows as an example. According to Ohm's law, the inverse of the tilt slope physically represents the shorting resistance (R_{sh}). In a normal CV curve without tilting, the tilt slope will be zero, representing infinite shorting resistance.
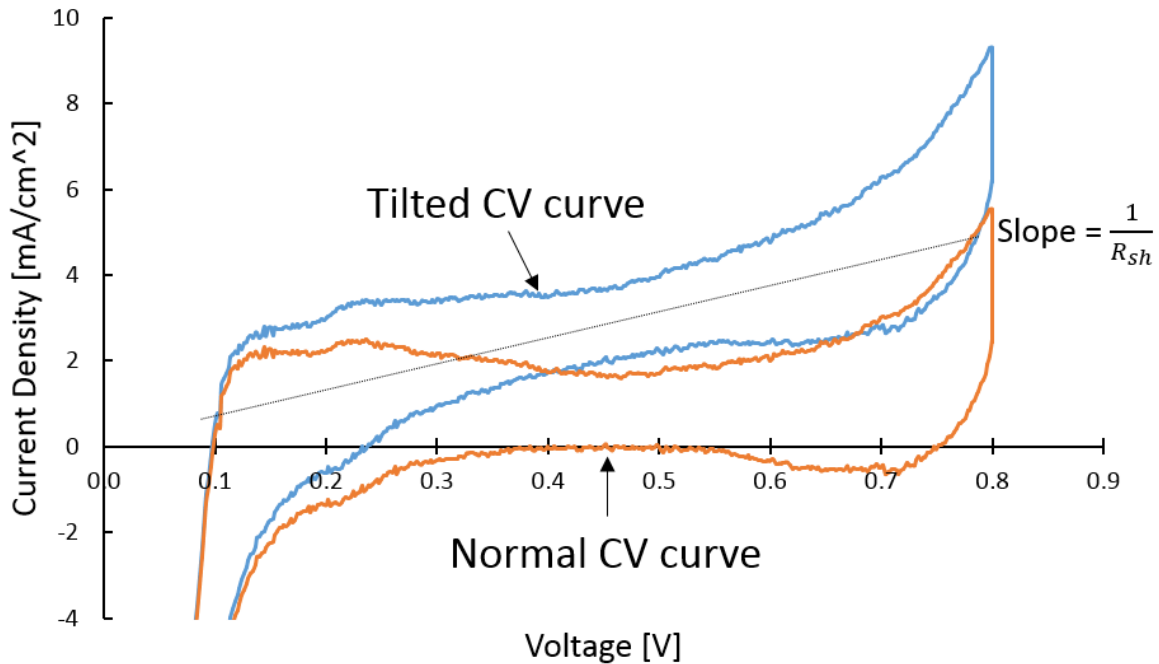
Figure 20: **Tilted CV curve and shorting resistance calculation.**

2.6.3. Electrochemical Impedance Spectroscopy

Electrochemical impedance spectroscopy (EIS) is another useful electrochemical diagnostics technique. Similar as CV, EIS was also conducted by Gamry Interface 5000 series potentiostat with working and sense electrodes connected to cathode and counter and reference electrodes connected to anode. Instead of triangular linear sweep, the input signal of EIS is a sinusoidal wave with small amplitude and varying frequency from high to low to measure the impedance of the system and gain other information related to charge transfer, mass transfer, and the double layer. EIS data is usually presented in Nyquist plot which is imaginary impedance (Z_{Im}) versus real impedance (Z_{Re}) plot. In fuel cells or other electrochemical systems, the schematic of electrode and electrolyte interface can be simplified as Figure 21 shows.
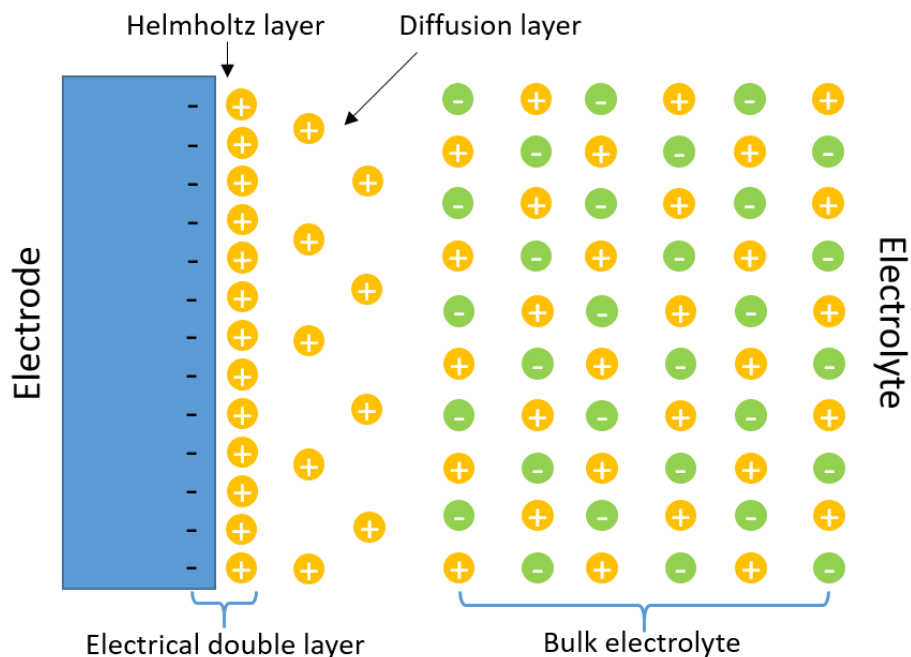
Figure 21: **Schematic of electrode-electrolyte interface.**

As illustrated in Figure 21, the surface of electrode is full of negative charge. As a result, ions with positive charge in the electrolyte are attracted to the electrode, forming a layer of positive ions at their interface (Helmholtz surface). Such structure is referred as the electrical double layer. In the electrolyte, the attractive force gradually reduces as the distance to electrode increases, which leads to the transition from Helmholtz surface to diffusion layer and finally to bulk electrolyte. It is notable that the sign of electrode surface charge depends on the electrode. The schematic shown in Figure 21 with negative surface charge refers to the anode while cathode surface has positive charge. In the case of cathode, negative ions in the electrolyte will be attracted. The double layer can be considered as a capacitor and its capacitance is referred to as the double layer capacitance (C_{dl}). Meanwhile, the faradaic reaction at the electrode-electrolyte interface will introduce faradaic impedance (Z_f) that is electrically parallel connected with the double layer capacitor. Faradaic reaction is composed of two processes, charge transfer and mass transfer. As a result, the faradaic impedance can be divided into charge transfer resistance (R_{ct}) and Warburg impedance (Z_w) which are series connected and corresponds to charge transfer and mass transfer respectively. The resistance of electrodes and electrolyte add up together to the internal cell resistance (R_Ω) and is series connected with double layer elements. Therefore, the equivalent circuit demonstrated in Figure 22 can be used to describe the schematic showed in Figure 21.
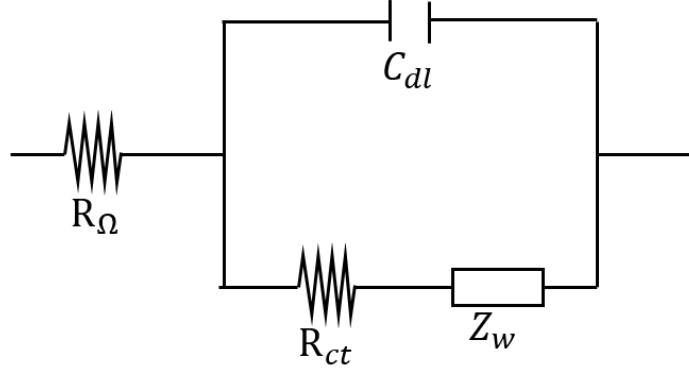
Figure 22: **Equivalent circuit of electrode-electrolyte interface.**

Impedance of the double layer capacitor is expressed as follows where ω is frequency:

$$Z_{dl} = \frac{1}{jC_{dl}\omega} \tag{21}$$

The Warburg impedance can be expressed by the following equation where σ is called Warburg constant and is related to mass transport:

$$Z_w = \frac{\sigma}{\omega^{\frac{1}{2}}} - j\frac{\sigma}{\omega^{\frac{1}{2}}} \tag{22}$$

As a result, real impedance and imaginary impedance of the equivalent circuit can be expressed by Equation 23 and 24. Detailed derivation of Equation 23 and 24 is presented in Appendix A.

$$Z_{Re} = R_\Omega + \frac{R_{ct}+\sigma\omega^{-\frac{1}{2}}}{\left(1+C_{dl}\sigma\omega^{\frac{1}{2}}\right)^2+C_{dl}^2\omega^2\left(R_{ct}+\sigma\omega^{-\frac{1}{2}}\right)^2} \tag{23}$$

$$Z_{Im} = \frac{C_{dl}\omega\left(R_{ct}+\sigma\omega^{-\frac{1}{2}}\right)^2+\sigma\omega^{-\frac{1}{2}}\left(1+C_{dl}\sigma\omega^{\frac{1}{2}}\right)}{\left(1+C_{dl}\sigma\omega^{\frac{1}{2}}\right)^2+C_{dl}^2\omega^2\left(R_{ct}+\sigma\omega^{-\frac{1}{2}}\right)^2} \tag{24}$$

In a given electrochemical system, internal resistance (R_Ω), charge transfer resistance (R_{ct}), and double layer capacitance (C_{dl}) are all system properties and remain constant. During EIS measurement, the sinusoidal wave is applied at various frequencies (ω). As a result, a Nyquist plot of Z_{Im} versus Z_{Re} can be obtained. An example of theoretical Nyquist plot using MATLAB® plotting function is demonstrated in Figure 23 with frequency ranging from 0.5 to 50000 Hz.

38
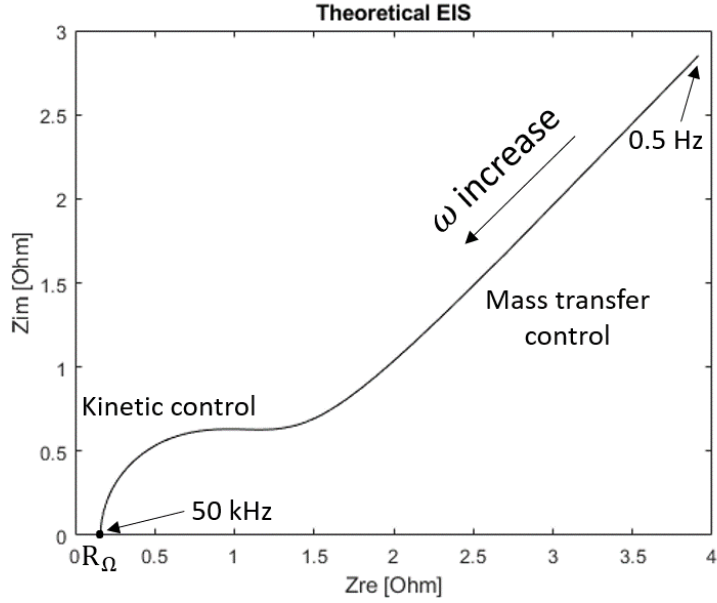
Figure 23: **Theoretical EIS plot.**

As indicated in Figure 23, the plot looks like an arc in high frequency region and a straight line in low frequency region. Such shape can be explained mathematically as well. In low frequency region where ω approaches 0, Equation 23 and 24 become the following form:

$$Z_{Re} = R_\Omega + R_{ct} + \sigma\omega^{-\frac{1}{2}} \tag{25}$$

$$Z_{Im} = 2C_{dl}\sigma^2 + \sigma\omega^{-\frac{1}{2}} \tag{26}$$

Rearranging Equation 25 and 26 yield the relation between Z_{Im} and Z_{Re}:

$$Z_{Im} = Z_{Re} - R_\Omega - R_{ct} + 2C_{dl}\sigma^2 \tag{27}$$

The plot of Equation 27 is a straight line with slope of 1, which matches the low frequency region as indicated in Figure 23. In the low frequency region, mass transfer is the dominating factor. Detailed derivation of Equation 25 and 26 can be found in Appendix A as well.

In the high frequency region where ω approaches infinity, mass transfer becomes negligible so that Warburg impedance in the equivalent circuit can be considered zero. As a result, the circuit in Figure 22 becomes:

39
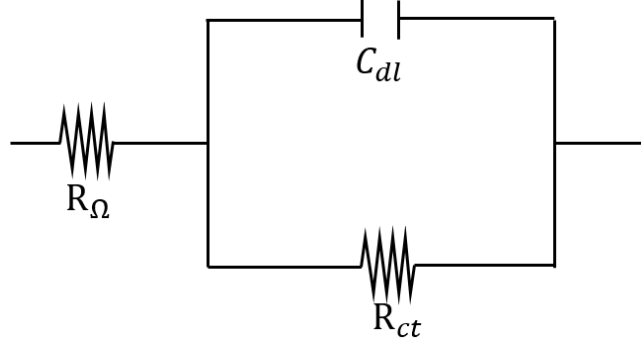
Figure 24:   Equivalent circuit of electrode-electrolyte interface at high frequency.

In this case, real and imaginary impedance of the system becomes:

$$Z_{Re} = R_{\Omega} + \frac{R_{ct}}{1+\omega^2 C_{dl}^2 R_{ct}^2} \tag{28}$$

$$Z_{Im} = \frac{\omega C_{dl} R_{ct}^2}{1+\omega^2 C_{dl}^2 R_{ct}^2} \tag{29}$$

Rearranging Equation 28 and 29 yield the relation between Z_{Im} and Z_{Re}:

$$\left[Z_{Re} - \left(R_{\Omega} + \frac{R_{ct}}{2}\right)\right]^2 + Z_{Im}^2 = \left(\frac{R_{ct}}{2}\right)^2 \tag{30}$$

The plot of Equation 30 is a semi-circle that matches the shape of the high frequency region in Figure 23. As the frequency approaches infinity, Z_{Re} and Z_{Im} of Equation 30 become R_{Ω} and 0, which corresponds to the point laid on Z_{Re} axis in Figure 23. Physically, it represents the total internal resistance of the cell, which is also called high frequency resistance (HFR). Detailed derivation of Equation 28 and 29 is also explained in Appendix A.

In the present work, a DC voltage of 0.45 V with a 10 mV AC perturbation signal was applied to sweep from 75000 to 0.5 Hz to obtain the EIS Nyquist plot. The plot was then fit into Randles circuit with Gamry® Echam Analyst software to obtain cell internal resistance (R_{Ω}), charge transfer resistance (R_{ct}), and double layer capacitance (C_{dl}). If only internal resistance is of interest, one can also read the Z_{Re} value when Z_{Im} equals to 0 without fitting the curve. An example of an actual EIS Nyquist plot is shown in Figure 25. The actual Nyquist plot is indeed following the overall trend of the theoretical plot.
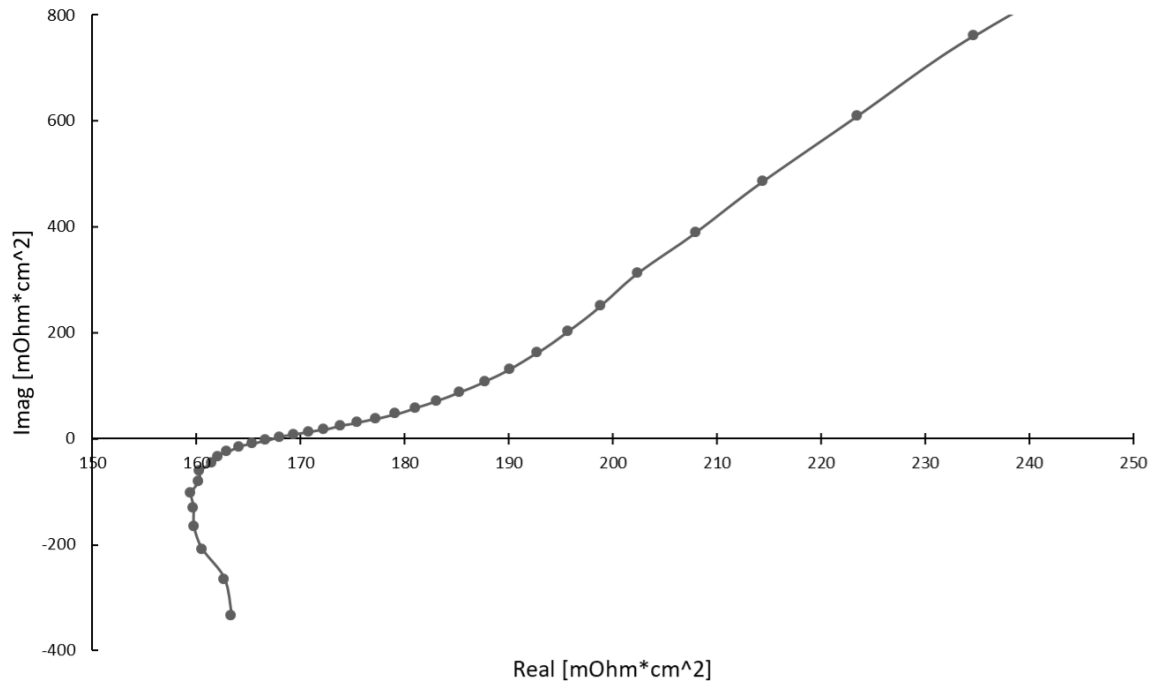
Figure 25: **Sample experimental EIS plot in the high frequency range.**

2.6.4. Electrochemical Leak Detection Test

Electrochemical leak detection test (ELDT) is an effective way to detect internal gas crossover through the membrane. In late stage of membrane degradation, membrane cracks and pinholes are very like to form, thus creating internal gas crossover path. Internal gas crossover will not only cause significant performance loss, but also raise safety concern since mixture of hydrogen and oxygen can be explosive. Therefore, it is important to check internal crossover frequently. The ELDT test was done at 75 °C with 100% RH. First, the cell was left at OCV for 20 minutes without back pressure control to reach steady state. Then, a 15 kPa pressure gauge was created by controlling anode back pressure. As mentioned earlier, overpressure was applied to the anode so that hydrogen will crossover to air side and form a mixture with low hydrogen concentration in case of leakage. The cell was left for another 5 minutes with anode overpressure. Average OCV in 5 minutes before and after applying the pressure gauge was then calculated and compared. As for the small scale cell design, a threshold of 30 mV was used to determine failure. In other words, if OCV dropped more than 30 mV after applying overpressure, the cell was considered to have reached end of life. This was generally verified against regular OCV measurements to confirm leak related failure.

2.7. X-ray Imaging and 4D *In situ* Visualization

X-ray computed tomography (XCT) is a non-invasive 3D imaging technique. Unlike the SEM based surface imaging, XCT is capable of scanning the interior MEA components without needing to disassemble the examined small scale fuel cell, which provides the feasibility to re-operate the cell after each scan. Such capability enables microstructural data acquisition of identical MEA locations in three space and one time dimensions, which is termed herein as 4D *in situ* visualization [52,85,86]. In this work, the MEA was scanned by a laboratory based ZEISS® Xradia 520 Versa micro-XCT system, which uses a tungsten target to generate X-ray. Principally, the XCT system consists of an X-ray generating source, a four degree of freedom (X, Y, Z translation and Y rotation) platform, and an X-ray detector, as illustrated in Figure 26. The examined small scale fuel cell sample housed in the custom designed fixture was attached to this platform prior to imaging. All XCT scans were performed at dry state except for BOL and EOL where both dry and wet scans were conducted. Dry scan requires the cell to be dehydrated while wet scan requires the cell to be pre-humidified. No gas was flowed into the cell during both dry and wet scanning. The dehydration was conducted on Greenlight® G20 fuel cell test station by flowing 70°C dry nitrogen for through both anode and cathode for 3 hours. The pre-humidification was conducted on a Scribner® 850C fuel cell test station by flowing 70°C oversaturated nitrogen through both anode and cathode for 2 hours. Both wet and dry scans were done at room temperature and share the same XCT settings. In each scan, voltage and power of the X-ray beam were set to 80 kV and 7 W respectively in order to penetrate platinum containing catalyst layers which tend to absorb X-ray due to its large atomic nucleus. Moreover, a built-in X-ray filter LE #1 was placed in front of the X-ray source to obtain ideal transmission. X-ray source and a 4X detector were placed at 30 mm and 40 mm from the sample, respectively, resulting in a 2.89 x 2.89 mm^2 field of view (FOV) and 1.42 μm pixel resolution. MEA regions at the neck of the hourglass shaped graphite plate were chosen for imaging, as indicated in Figure 26, since lower thickness graphite material is likely to produce less noise in projections. Two separate XCT scans of left and right edges, along with the adjacent channels, were performed in each scanning cycle, and the chosen source/detector distances were an optimal setting for preventing any collision with the sample during its rotation. In each scan, 1601 2D radiographic projections were acquired over a 180° angle range with additional flag angle of 4° (-94° to +94°) of the rotating sample. Each

projection requires 10s of X-ray exposure in order to achieve sufficient intensity throughout the MEA components. High aspect ratio tomography (HART) setting was also applied to enhance image quality, wherein higher density of projections were obtained from computational reconstruction of the acquired 1601 2D images using ZEISS Xradia's XMReconstructor software. During the entire experiment, design 1 experienced approximately 40 hours of total X-ray irradiation, whereas design 2 had a longer cumulative exposure of around 96 hours owing to its delayed failure. According to previous X-ray exposure studies on a similar small scale fuel cell, 96 hours exposure time is not expected to pose significant impact on fuel cell performance [88], and 50 hours exposure time is not expected to pose significant impact on membrane mechanical properties [52].
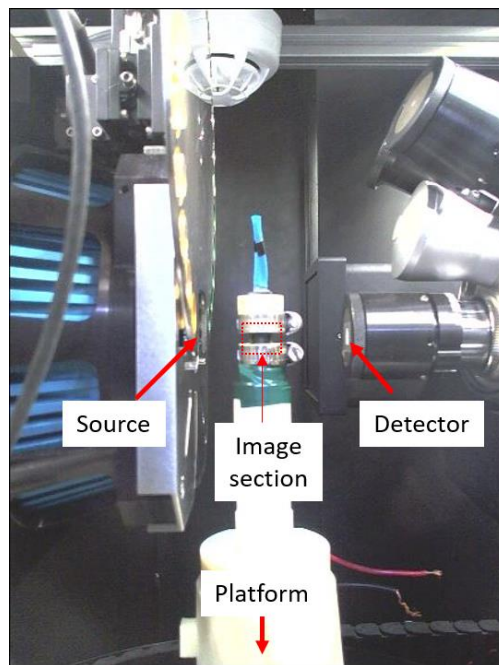
Figure 26:   Visualization setup inside the micro-XCT system.

2.8. Image Processing

The 3D virtual image stack contained all MEA components as well as partial graphite flow field plates. Focused image analysis on the membrane component requires the membrane to be digitally isolated from the other components, especially from the CLs. In the present work, reconstructed image stacks were saved in TIFF files and processed by open source software Fiji ImageJ®. The steps of image processing and membrane segmentation are illustrated in the flow chart of Figure 27.
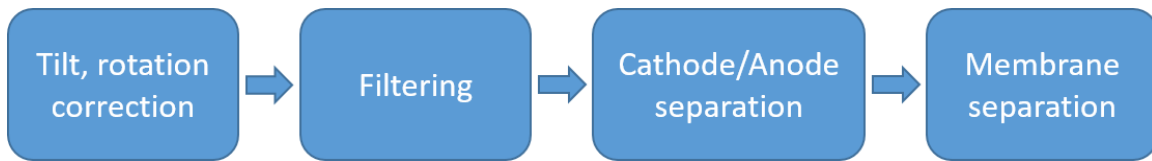
Figure 27:   Flow chart of image processing.

ImageJ displays the virtual 3D image stack as multiple slices along XY, XZ, or YZ planes. Ideally, it is preferred to have the membrane parallel to XY plane for easier segmentation. However, the raw image stacks are likely to be slightly tilted, as demonstrated in Figure 28(a). The tilt can be adjusted by rotating the image stack along each individual axis. As indicated in Figure 28(b), a larger portion of the CCM can be included in the corrected slice compared to the uncorrected slice.
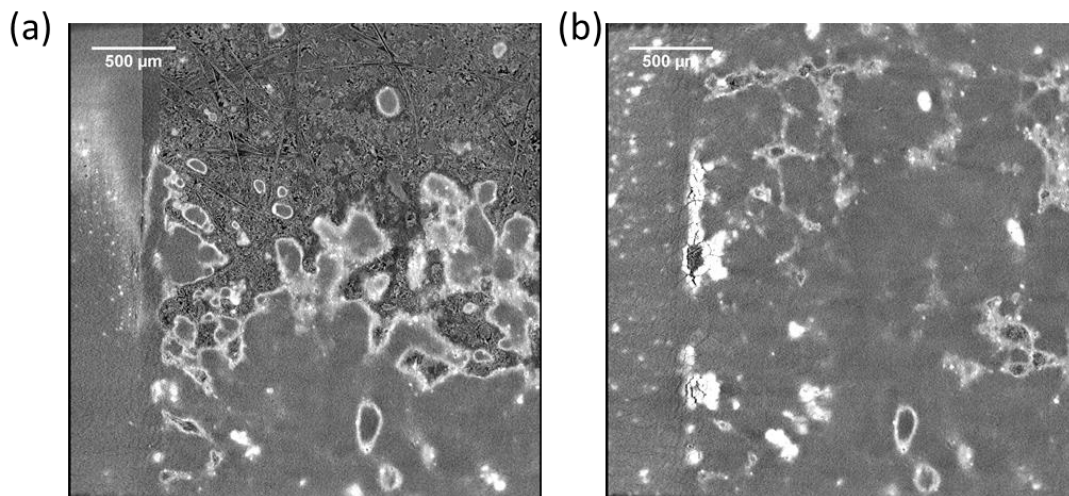
Figure 28:   Same CCM plane (a) before tilt correction (b) after tilt correction.

After tilt correction, the image stack needs to be filtered in order to reduce noise before cathode and anode separation. Catalyst layer separation is based on the greyscale difference between membrane and catalyst so that threshold can be applied accordingly. However, the unfiltered image contains noise which will compromise the quality of thresholding algorithm, as indicated in Figure 29(a)-(b). To reduce the effect of noise, two filters were applied to the image: (i) 3D median filter of size 2 x 2 x 2 pixels; and (ii) anisotropic 2D diffusion filter. The median 3D filter aims to remove the speckle noise while the anisotropic diffusion filter reduces greyscale variation inside a single phase in order to improve segmentation accuracy. The same slice after filtering is demonstrated in Figure 29(c)-(d). As observed, the noise level under the same threshold has been greatly reduced.
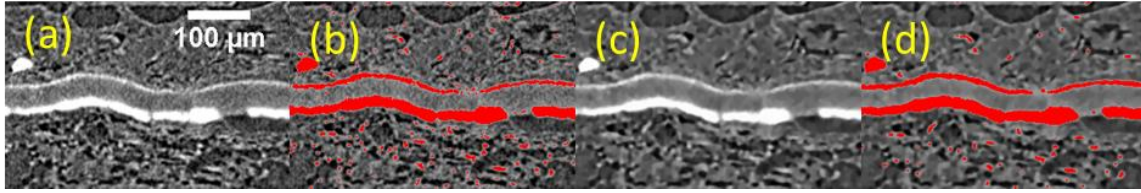
Figure 29: MEA cross-sectional slice (a,b) before and (c,d) after filtering. (a) and (c) show the grayscale view whereas (b) and (d) show the thresholded view.

In terms of catalyst layer separation, the first step was to separate CCL by defining a global threshold, as indicated in Figure 29(d). In addition to CCL, ACL and some GDL fibers were also selected by the global threshold, which will be removed later by a custom developed algorithm named 'cathode separator'. The cathode separator first applies a 2D Gaussian blur to connect the catalyst islands, followed by selection based on volume that has been connected. In the present work, CCL was thicker than ACL, resulting in larger total volume compared to ACL. Therefore, ACL and noise in GDL were abandoned while only CCL was selected and separated. The CCL will be masked after the separation and ACL will be separated in a similar way. Full CCL and ACL separation procedure is demonstrated in Figure 30.
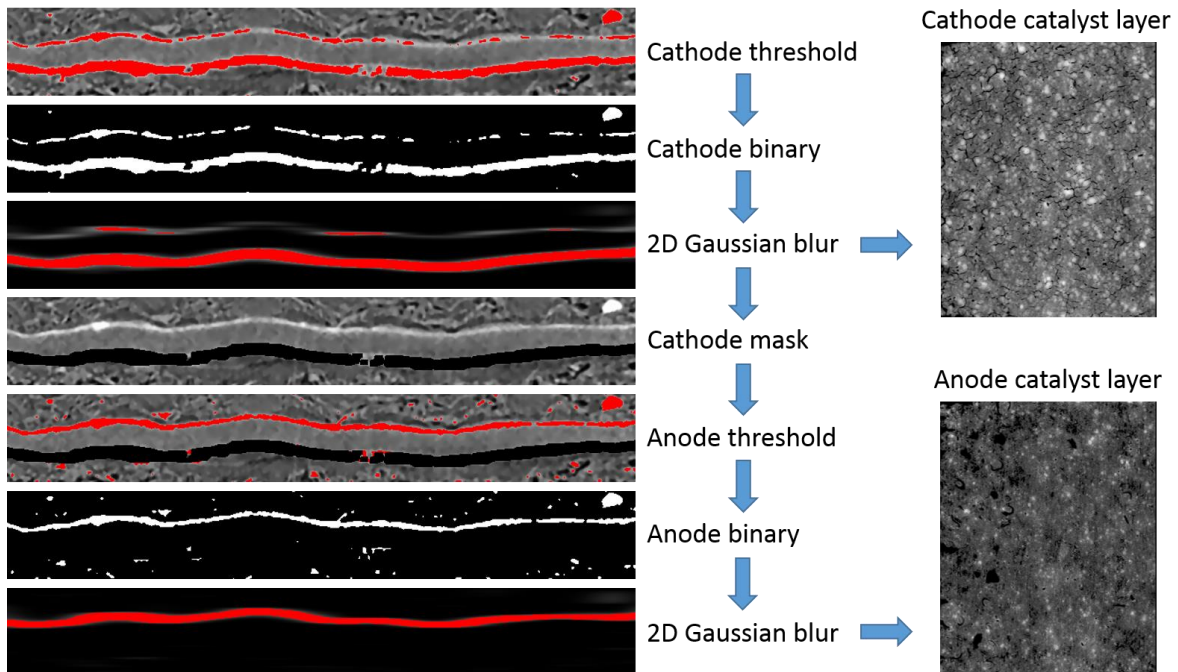
Figure 30: Cathode and anode CL separation procedure.

The segmentation of membrane was accomplished by using ACL and CCL as upper and lower boundary, with any material in between being assigned to the membrane part. This process was carried out by another custom developed application called 'MemSeg'. Here, dynamic slices were used to show the evolution in the membrane structure from the anode interface to the cathode interface. Dynamic slices are especially useful for membrane degradation analysis. For instance, it can help identify if a membrane crack is through-plane and determine on which electrode membrane cracks were initiated. In the present work, membrane separation was sometimes challenging due to irregular structure at the MEA edge, such as additional CL cracks and local membrane thinning and buckling. Such features may induce artefacts in the CL separation and thus compromise the quality of the boundaries used in membrane segmentation. For this reason, features observed on the segmented membrane were always compared with the original image stack to ensure fidelity.

Chapter 3.   Results and Discussion

As mentioned in introduction chapter, the primary goal of this work is to understand the fundamentals and root cause of combined chemical and mechanical fuel cell membrane degradation in both active area and edge regions. This chapter contains two sub-sections, where section 1 is focused on edge region membrane degradation and mitigation, and section 2 is focused on active area membrane degradation. In section 1, failure of the original Teflon®-Kapton®-CCM rigid frame edge design is discussed and analyzed first. Then, degradation of the subsequent Kapton®-Teflon®-CCM rigid frame edge design is presented to compare with the original edge design. In section 2, active area membrane degradation of the MEA with subsequent edge design is presented and discussed, with electrochemical diagnostic results showed first then followed by morphological analysis.

3.1. Edge Failure Mitigation

3.1.1. MEA Edge Design 1

Morphological Analysis

Small scale MEA with Teflon®-Kapton®-CCM rigid frame edge design (design 1, Figure 11) was subjected to the combined chemical and mechanical AST with XCT scans and diagnostics taken periodically up to the 21st AST cycle. Due to the area limitation of FOV, the two flow channels were imaged separately as indicated in Figure 11(b). Membrane plane at BOL was crack free for both edges, as indicated in Figure 31 (a) and (c). The dark, round shaped feature in BOL active area in Figure 31(c) was induced by membrane curvature, which is an out-of-plane feature rather than membrane defect. The same FOVs were periodically imaged so that evolution of the morphological changes is able to be captured. Through-thickness edge failures in the membrane were first observed after the 9th AST cycle when a number of cracks had formed under the Kapton®/Teflon® gasket layer covered regions on both left and right MEA edges, as depicted in Figure 31 (a) and (c). By this stage, there was about 10% OCV loss and an introduction of voltage fluctuations during the OCV hold phase. At the left edge, three large cracks were observed after 9 cycles in the cross-flow direction, where crack A and

B were relatively narrow and oriented at an angle with the X axis, i.e., perpendicular to flow field direction, while crack C was wider and almost parallel to the X axis. When examined through the cross-sectional perspective, the span of crack C was found to lie almost directly underneath the outer Teflon® gasket layer at the edge. Moreover, the CCM had undergone a significant permanent in-plane expansion by the 9th cycle, as detected by changes in the cathode's in-plane morphology shown in Figure 32 This is indicative of plastic creep deformation experienced by the membrane during the AST. This deformation was likely favored by a reduced level of adhesion between the CCM and Kapton® gasket due to a possible 'flow' of adhesive glue present on the interfacing Kapton® layer under the elevated temperature and humidity conditions of the AST. Cracks A, B and C were 973, 805, and 967 µm long, respectively, at this stage. After another two AST cycles, two more similarly shaped edge cracks (crack D and E) were formed with crack D being 1059 µm in length and comparable to the existing crack sizes. The length of crack E was not measurable since it spanned beyond the FOV. Propagation of the three existing cracks was negligible from 9 to 11 cycles. No such additional cracks were formed from 11 to 21 cycles (*i.e.*, EOL) and there was negligible propagation of the existing cracks. On the right MEA edge, similarly oriented and sized (approx. 1000 µm length) edge cracks were observed after 9 AST cycles underneath the same Kapton®-Teflon® gasket region. However, another unique membrane damage feature (tear F) was formed underneath the extended Kapton® sub-gasket region as indicated in Figure 31(c)-(d). Tear F had maximum length of 1865 µm and maximum width of 356 µm, with total approximate surface area of $0.6\,mm^2$. Its shape and orientation were different from the other edge cracks, and it spanned longer in the Y (parallel-flow) direction than X (cross-flow) direction. Upon examining the planar and cross-sectional views together, the left edge of tear F was found to be a straight line constrained by the edge of the Kapton® sub-gasket layer. Given its relative proximity to the flow fields, the tear F could have potentially introduced more hydrogen crossover than the other cracks, and consequently, its shape may have been further influenced by membrane damage from any associated chemical combustion. Similar to the left edge, the propagation of cracks was also negligible at the right edge from 9 cycles to EOL.
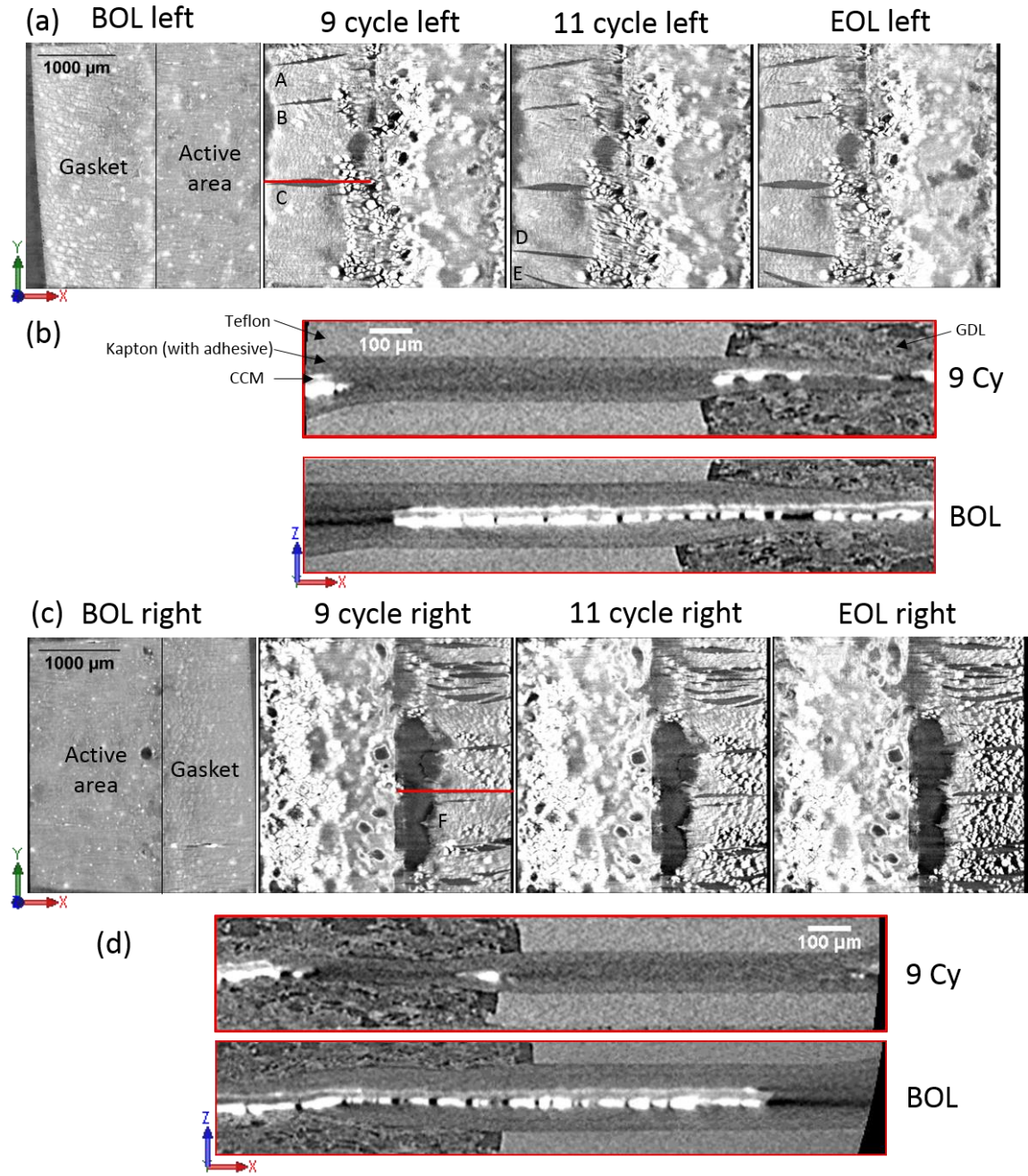
Figure 31: MEA edge design 1 4D identical location XCT imaging: (a) left edge membrane planar view from BOL to EOL; (b) crack C cross-sectional view at the highlighted location after 9 AST cycles; (c) right edge membrane planar view from BOL to EOL; and (d) tear F cross-sectional view at the highlighted location after 9 AST cycles.

Teflon Kapton Teflon Kapton
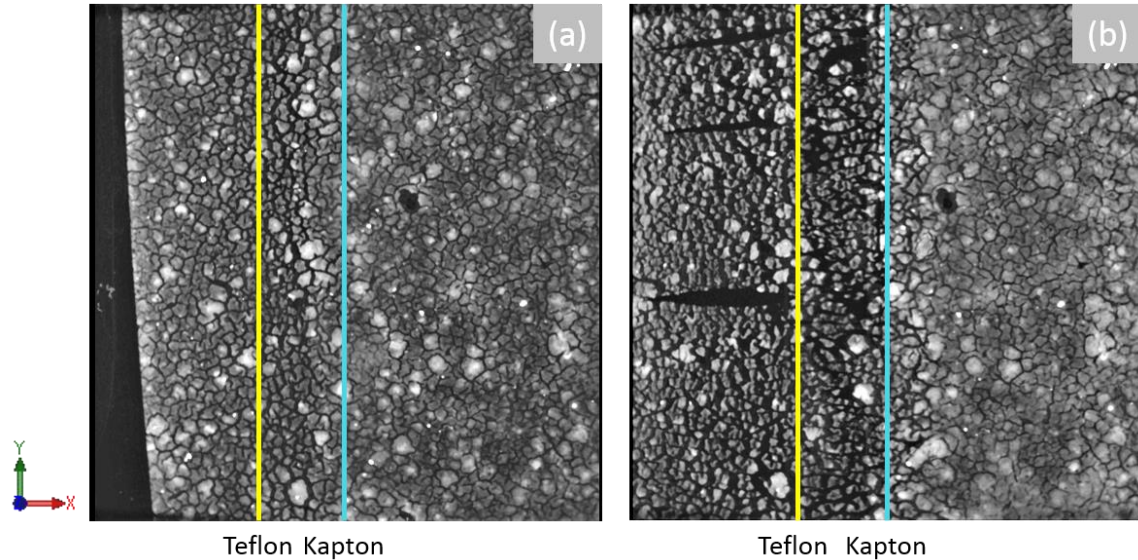
Figure 32: **Identical-location planar images of MEA edge design 1 CCL at (a) BOL (b) after 9 AST cycles.**

The formation of membrane cracks under the Kapton®-Teflon® gasket region and permanent in-plane membrane/CCM expansion showed in Figure 32 were likely related to mechanical factors. In Figure 32(a), left edge of the catalyst layer is clearly seen within the FOV, but this edge is no longer visible in Figure 32(b) after 9 AST cycles. Besides, catalyst particles left to the Kapton® edge are denser in Figure 32 (a), but their distribution becomes more discrete after 9 AST cycles in Figure 32(b). Therefore, membrane left to the Kapton® edge has expanded after 9 AST cycles. During the RH cycling, rapid humidity change allows membrane to repeatedly swell and shrink. In the swelling phase, membrane can have in-plane and/or through-plane expansion, as governed by the assembly constraints. The CCM is interfaced with GDLs in the active area and with Kapton® in the gasket regions. In the active area, the membrane could readily expand through-plane by compressing the GDL. Moreover, the typically rough MPL surface [53] may have provided sufficient friction to minimize relative motion between the CCM and GDL, and accordingly, the cathode microstructure remained unaltered in these regions suggesting a negligible permanent deformation of the CCM. In the gasket region, contrastingly, the rigid Teflon® held under compression is a stronger constraint against through-plane membrane expansion, which likely 'forced' the membrane to expand in plane. Additionally, viscosity of the adhesive coated on Kapton® layer may have reduced under heated and humidified conditions of the AST, leading to a loss of the gasket's capacity to constrain in-plane CCM expansion. Accordingly, CCM

may have experienced in-plane slipping motion under the Kapton® gasket that resulted in its permanent hygrothermal creep. During the drying phase, tension will be generated as the membrane dehydrates and shrinks. The weak part of membrane with relatively larger tension was likely to have cracks formed. Additionally, the length of edge cracks (excluding tear F) were all around 1000 µm which is same as the width of the Teflon® gasket layer compressed by graphite plate. The cracks were limited to the Teflon® gasket covered region, wherein the membrane was likely under the highest compression. Tear F was the only crack that formed under the Kapton® sub-gasket layer region overlapping the CCM. According to its morphology, the left edge was a straight line but the right edge demonstrated a non-uniform outline. Moreover, the surface area of tear F was significantly larger than any other edge cracks. It's possible that the formation and propagation of this particular feature was influenced by both chemical and mechanical stressors. Due to the presence of Kapton® gasket layer, membrane under this region experiences higher through-plane compression relative to the active area. Therefore, mechanical failure could be initiated due to locally restricted through-plane expansion and enhanced in-plane expansion. Given the proximity to active area, gas crossover may have further accelerated local chemical membrane degradation, thereby reducing its mechanical strength.

In addition to the membrane cracks observed at the lateral edges, wrinkling was another membrane deformation that has been observed at the longitudinal edges. Figure 33 demonstrates the 3D XCT image of another cell with MEA edge design 1 after 15 cycles of combined chemical and mechanical AST.
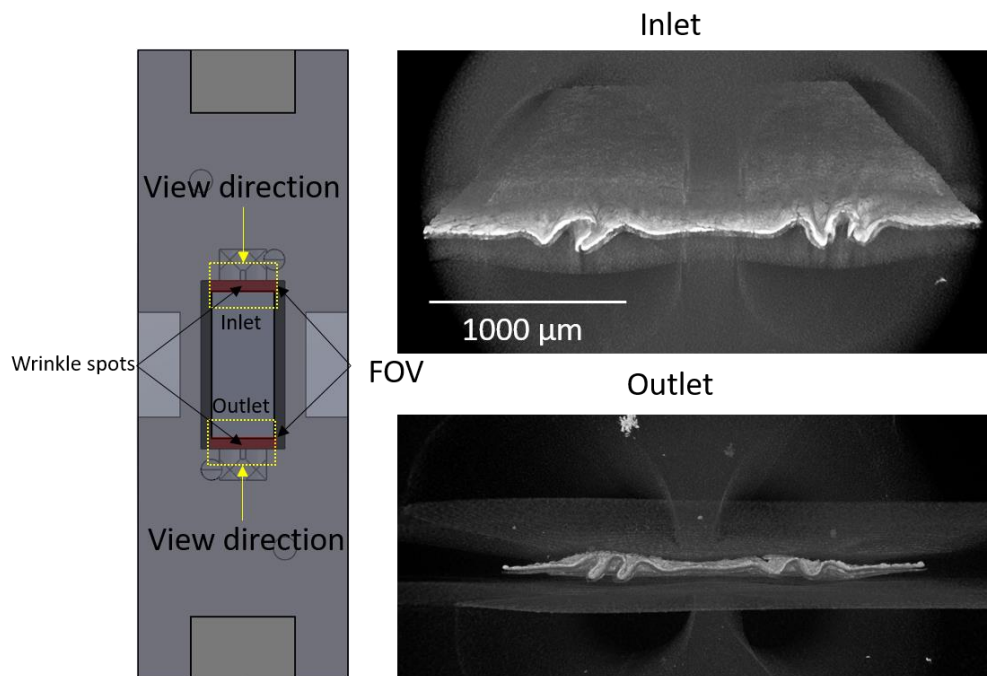
Figure 33:   **CCM wrinkling at inlet and outlet under flow channels.**

As indicated in Figure 33, the formation of CCM wrinkling needs to meet two requirements: (i) membrane is covered by adhesive layer of Kapton® sub-gasket rather than GDL; and (ii) membrane is located under the flow channels. As discussed before, membrane lateral edges tend to have in-plane expansion due to the presence of compressed graphite plates and relatively rigid Teflon® gasket layer. However, compression is absent at the flow channel portion of the longitudinal edges, causing non-uniform compression on the four edges, as indicated in Figure 34(a). During combined AST cycles, Kapton adhesive may creep into the flow channel regions and form big agglomerations. The big agglomerations will then push the gasket layers and force them to curve, which provided the space for through-plane membrane wrinkling in the first place. On the other hand, lateral edges undergo in-plane expansion as indicated in Figure 34(b), which squeezes the longitudinal edges so that longitudinal edges are forced into the channel regions. Inside flow channels, adhesive cannot serve as a strong constraint because it behaves like fluid. Therefore, membrane wrinkling happens as a result of longitudinal edges being squeezed. The morphology of CCM after going through numbers of AST cycles with MEA edge design 1 generally has the shape as demonstrated in Figure 34(b), due to expansion in lateral edges and extrusion in longitudinal edges. When membrane dehydrates, edge cracks will form at local strong adhesion spots due to tensions generated as membrane shrinks.
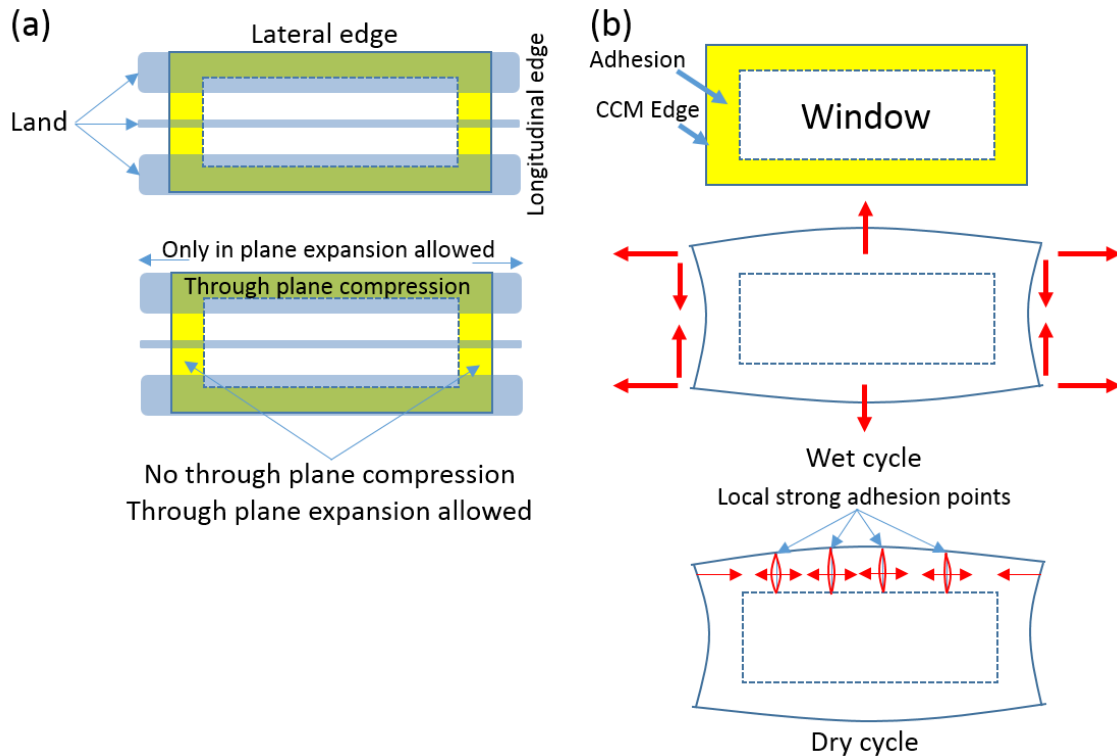
Figure 34: **(a) Non-uniform compression on MEA edges in land and channel regions (b) Schematic of CCM morphological change and edge failure formation.**

Performance Loss Analysis

OCV of the cell was monitored throughout until the cell reached failure after 21 cycles, characterized by an OCV loss of more than 20% from the BOL state, which indicated hydrogen leak across the membrane. Performance effects of membrane edge cracks in the small scale MEA were evaluated using the aforementioned *in situ* diagnostics techniques. According to the OCV plot shown in Figure 35, the cell voltage remained relatively steady from BOL to 7th AST cycle, indicating negligible degradation up to this life stage. An abrupt OCV drop occurred from the beginning of 8th AST cycle along with the introduction of voltage fluctuations, which continued until the 14th AST cycle. This timeframe coincides with the edge crack development period, as identified by the 4D *in situ* visualization methodology. It was further confirmed that there were no detectable microstructural changes indicative of membrane degradation in the MEA active area up to this stage. Accordingly, it is inferred that the edge cracks opened up hydrogen crossover channels and led to the observed OCV decay and fluctuation, which is consistent with Macauley et al.'s observation in accelerated membrane durability testing [46]. The OCV remained relatively steady at around 0.75 V from 14th to 21st AST

53

cycle with the fluctuations still present and growing in amplitude. The steady voltage region could be attributed to the lack of crack propagation observed from the edge cracks. The cell failed at 22nd AST cycle, but without any indications of significant membrane failures in the active area. The polarization curves shown in Figure 36 also indicate gradual OCV and performance loss from BOL to the 21st AST cycle, especially in the activation region. Ohmic loss was relatively steady according to the slope of the polarization curves. Similarly, the mass transport loss region did not reveal any significant trends. CV and EIS measurements also did not reveal any statistically significant changes due to degradation and are hence omitted. ELDT measurement was not feasible with design 1 due to the voltage fluctuations. Accordingly, the significant development of edge cracks in the membrane was deemed to be primarily responsible for the failure of the small scale MEA with edge design 1. This failure mode prevented any meaningful 4D analysis of membrane degradation in the MEA active area and its correlation with the diagnostics. The OCV loss from edge cracks may have further reduced the membrane chemical stressors, thus lowering the effectiveness of the applied AST in producing membrane degradation in the active area.
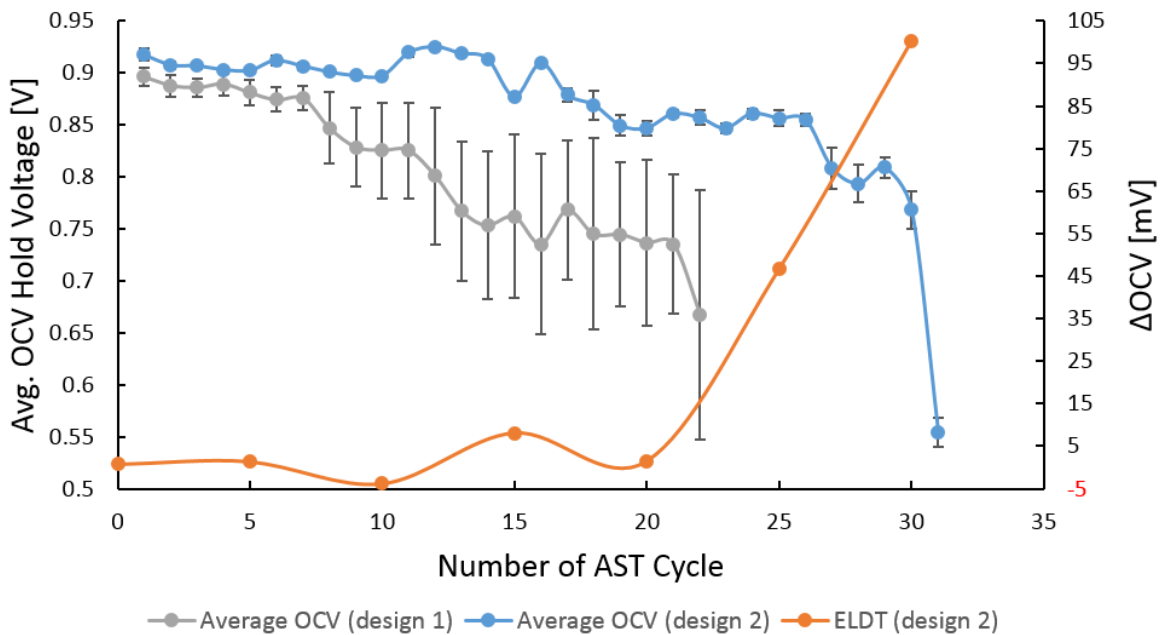
Figure 35: **OCV decay and ELDT plot.**
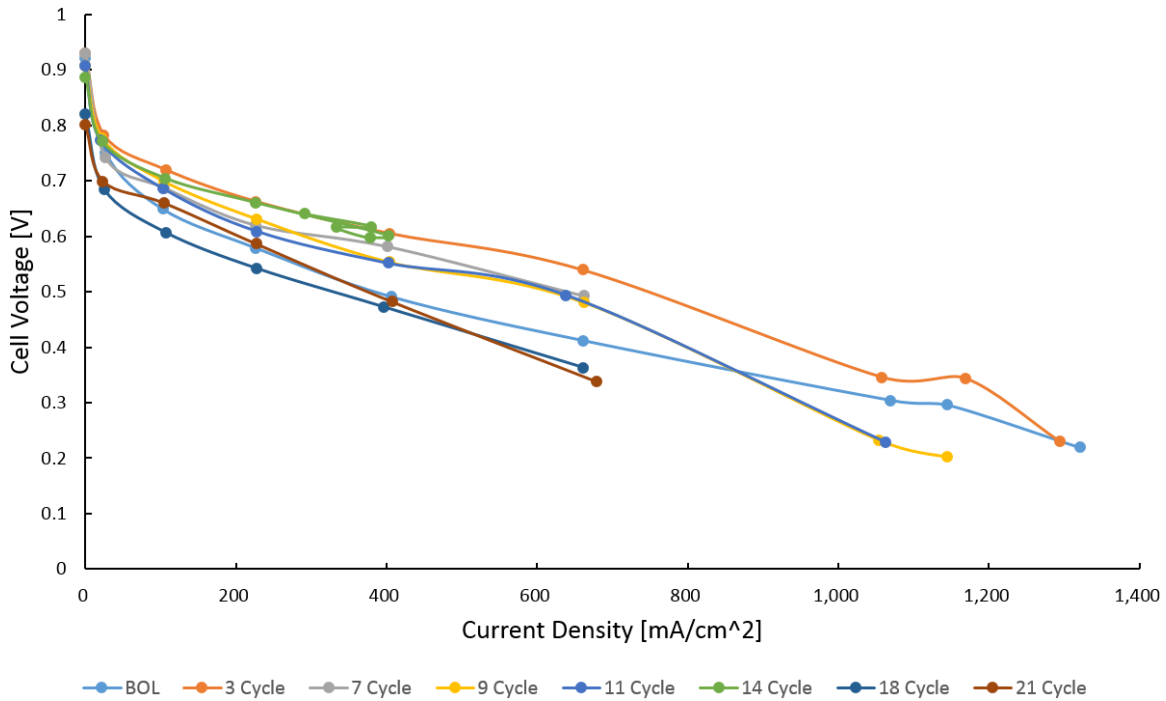
Figure 36: Polarization curves of the MEA with edge design 1.

3.1.2. MEA Edge Design 2

Design Modification

Based on the analysis of in the membrane failure mode at the edges of MEA edge design 1, two major design changes were made in MEA edge design 2 in order to conceivably mitigate edge failure and shift the membrane failure into the main active area. However, MEA edge design 2 is still based on rigid frame sealing technique. First, the position of Kapton® and Teflon® gasket layers was switched in assembly such that the Teflon® layer now interfaced with the CCM. The rough surface of Teflon® without adhesive could minimize CCM slippage and deformation relative to the gasket layers. The Teflon® layer, however, does not have adhesive coated on it, which introduces two assembly-related challenges: i) CCM could not be fixed on the interfacing gasket layer (unlike the framed Kapton®-CCM sub-assembly of design 1), thus increasing the number of separate layers to be handled during assembly; and ii) there could be micro voids at the Teflon® layer–CCM interface, which could potentially compromise the leak prevention function of the gasket. To overcome these two challenges, the outer dimension of Teflon® was reduced from 10 x 30 mm^2 to 6 x 16 mm^2 and the CCM dimension was increased to 8 x 20 mm^2, which allowed the peripheral outline of the

55

CCM to be attached on Kapton® adhesive layer to create a secondary sealing as well as a rigid single-piece frame for convenient assembly.

The second major design change was to increase the dimension of gasket layer windows and GDLs to 4 x 13 mm^2 in order to fully cover the flow channel length with GDL, thereby providing a uniform compression throughout the channel length. In design 1, the inlet and outlet regions of the flow channels were only partially covered by the GDLs which led to non-uniform compression and associated mechanical stress concentration effects. Therefore, CCM wrinkling occurred as the result. Uniform compression throughout the channel length should in theory eliminate wrinkling issue.

Morphological Analysis

Identical edge locations of the small scale MEA with edge design 2 were visualized after each set of 5 AST cycles from BOL to EOL. Edge cracking was first observed at the left and right edges after 10 and 15 AST cycles, respectively. Figure 37 shows the periodically acquired identical membrane plane locations at both edges along with periodic cross-sectional views of representative edge cracks. There were several spots in the membrane plane where traces of catalyst layer and adhesive regions could be seen due to the curvature of membrane, as indicated in the cross-sectional view. Accordingly, supplementary verifications of the observations were also made using the cross-sectional views afforded by the 3D nature of data. At BOL, the membrane was crack free and had a slight curvature at the edge of gasket region. At the left edge, three small edge cracks were formed after 10 AST cycles, with crack L1 being a through-thickness crack showing clear boundary while cracks L2 and L3 showed less distinguishable outline and were not yet extending through the full thickness of the membrane. After another 5 cycles of operation, crack L1 propagated along its direction, and crack L2 and L3 became through thickness membrane cracks. In addition, crack L4 was newly formed and observed at the 15th cycle. The right edge remained crack free until three through-thickness edge cracks R1-R3 formed after 15 AST cycles. As a result, major cracks only developed after 15 cycles at both left and right edges. The cell failed at 31st cycle due to significant abrupt loss in OCV as indicated in Figure 35, which was evidently caused by hydrogen crossover associated with membrane damage in the active area (to be discussed further in Section 3.2).

By the EOL stage, several new membrane cracks were formed, such as crack L5 which was initiated at 20th cycle, and all the existing cracks continued propagating along their original direction. Interestingly, all cracks at EOL stage had reached a similar length, while the crack lengths at 15th cycle were still considerably different. For instance, crack L1 was 120 µm and crack L4 was 67 µm in length at the 15th cycle, and crack L1 had grown to 193 µm while crack L4 had grown to 187 µm by EOL. Crack L5, which was not present at 15th cycle, had grown to 184 µm length at EOL. It may be inferred that the edge crack growth was restricted to a limited region beyond which they were unable to propagate freely. According to cross-sectional view, these edge cracks were all formed at the boundary where the Kapton®-Teflon® gasket layer meets the GDL, especially in the gap region between gaskets and GDLs that was filled with adhesive (Figure 37 (b) and (d)). Most edge cracks in the FOV at EOL were still constrained in the adhesive filled gap region with only cracks L2 and L3 slightly propagated into the GDL covered region, noting that cracks L2 and L3 had a larger dimension when initially formed. The dual Kapton®-Teflon® gasket layer was attached and cut together, leading to an open end into which the adhesive could flow when necessary driving forces are present. The flow of adhesive is promoted during operation in the presence of clamping compression forces, and leads to adhesive accumulation in the assembly gap between the gasket layers and GDL. The anode and cathode gasket layers had approximately 90 µm uniform offset (Figure 37(b)) along the entire image stack, resulting in approximately 160 µm total width of adhesive filled gap region on each edge. All cracks on the left edge had an angle between 10° to 30° with the X (cross-flow) direction, resulting in the actual length larger than horizontal length. Crack lengths were therefore projected on X axis to determine their horizontal length. At EOL stage, cracks L1-L5 had horizontal lengths of 193, 258, 250, 187, and 184 µm, respectively, which were slightly larger but still comparable to the width of the gap region. Based on the BOL cross-sectional view (Figure 37(b)), membrane under adhesive covered gap region appeared to be thinner than membrane in the active area. According to measurement results, membrane was 10 - 15 µm thick in adhesive covered region compared to 20 µm in land region and 22 µm in other regions, primarily due to local stress concentration. Such loss in membrane thickness would reduce mechanical strength and facilitate crack formation in this region. The right edge showed similarly angled cracks oriented symmetrically to the left edge, as depicted in Figure 37(c). The misalignment between anode and cathode gasket layers was 45 µm, and the adhesive covered gap region was 180 µm wide (Figure 37(d)). Initial

cracks were observed after 15 AST cycles (Figure 37(c)). After another 5 cycles of AST, all those initial cracks were significantly propagated with several new cracks formed. However, from 20th cycle to EOL, there was only mild propagation for both the original and the newly formed cracks. The crack propagation trends were generally consistent between the two edges, and overall crack lengths remained confined to a limited region around the gasket edges. Similar local membrane thinning issue was also observed at the right edge.
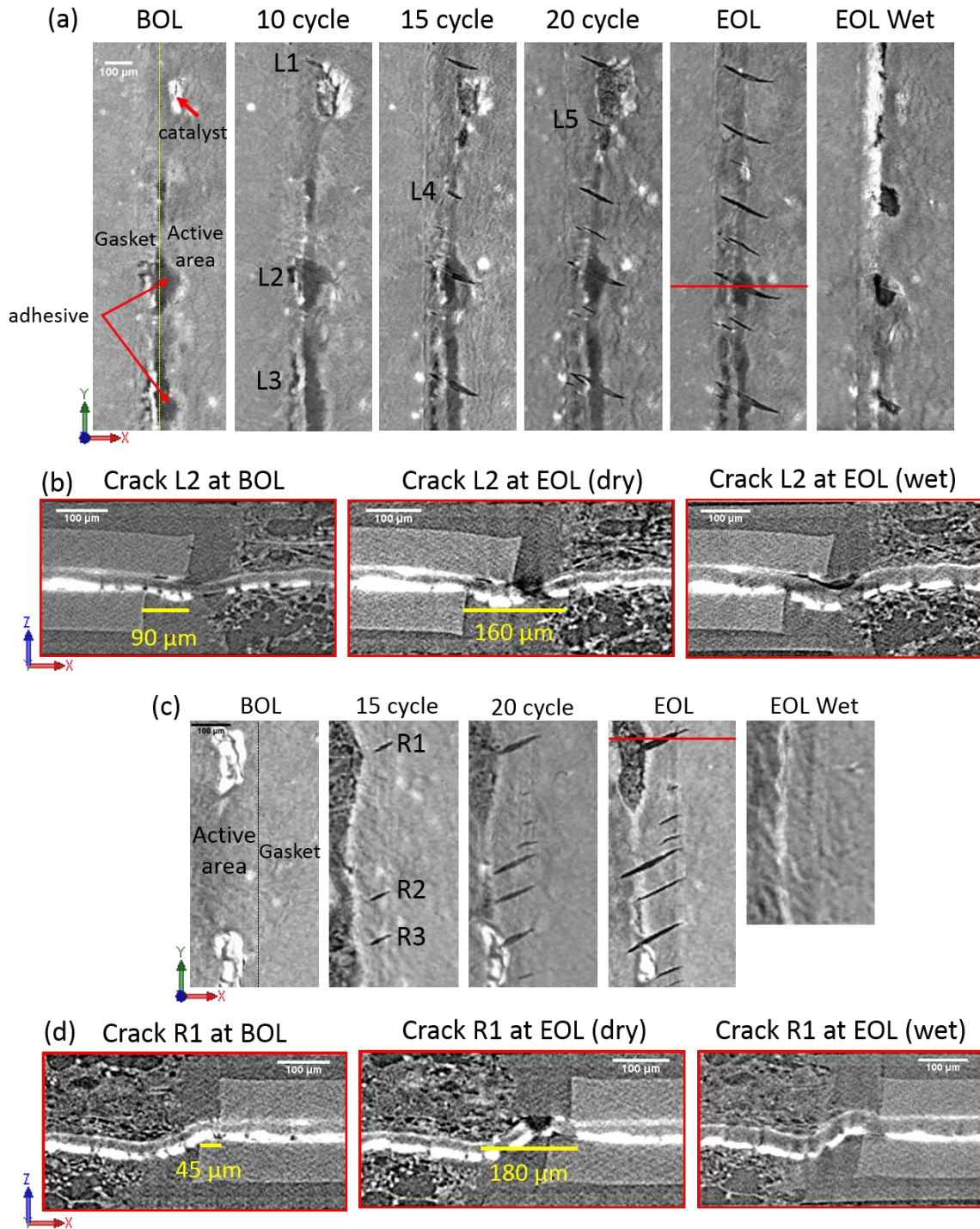
Figure 37: Design 2 4D crack at identical location (a) left edge membrane planar view from BOL to EOL (b) crack L2 cross-section view at highlighted location at BOL, EOL dry state, and EOL wet state (c) right edge memrbane planar view from BOL to EOL (d) crack R1 cross-section view at highlighted location at BOL, EOL dry state, and EOL wet state.

In order to quantitatively analyze the growth of edge cracks in design 2, the total number of membrane edge cracks that were though-thickness and longer than 50 µm along with the length and area of those cracks demonstrated in Figure 37 are plotted against the number of applied AST cycles in Figure 38. Both the number and size of edge cracks generally increased with combined AST cycling. The number of cracks at the right edge grew more rapidly than at the left edge, which could be explained from a stress relaxation perspective. Two initial cracks at the left edge were significantly larger in both length and area after the 15th cycle. The dominant large cracks are likely to help release stress at adjacent smaller cracks, thus minimizing any new detectable crack formations. Similar interaction among cracks was also reported by Singh et al. [52] However, the cracks at the right edge were relatively smaller in size and may have thus afforded a lower level of stress release in the adjoining regions. As a result, a larger number of cracks were formed at the right edge to help distribute the release of stresses. For both edges, the majority of cracks were propagating faster during the first five AST cycles of their formation (*i.e.*, 15th to 20th cycle) compared to the later AST cycles (20th cycle to EOL) and appeared to eventually stabilize to a steady crack size, which supports the aforementioned observations of crack growth being restricted to a limited space in design 2. Amongst the five indicated cracks at the left edge, cracks L2, L3, and L4 had almost identical propagation rate in length according to their slope. Crack L1, which had larger initial length than cracks L4 and L5, ended up with similar length and area as L4 and L5. It is also noteworthy that the area of cracks L2, L3, and L4 decreased from the 25th cycle to EOL, which was attributed to a reduction in the width of these cracks with their longitudinal propagation. The indicated initial cracks at the right edge had comparable length to that of the three smaller cracks (L1, L4, and L5) at the left edge. Moreover, their individual propagation trends and final length were also similar. However, the area of the right edge cracks had almost stabilized after the 20th cycle, resulting in the left edge cracks having generally larger final crack areas at the time of failure. In conclusion, although the right edge had more cracks than the left edge, the crack sizes were generally smaller. The mechanisms of crack formation and propagation appeared to be consistent for both edges. Membrane at gasket edge region is covered by adhesive, which is a less rigid material than GDL or Teflon® gasket layer. Therefore, membrane in this region is subjected to higher cyclic mechanical stress during swelling and shrinking. Moreover, membrane is already thinner at this location from BOL, causing membrane strength reduction. As a result, membrane cracks were induced by these two

factors at the adhesive covered gasket edge region. On the other hand, membrane will experience less cyclic stress at GDL and Teflon® covered regions, thus preventing edge cracks from further propagation.
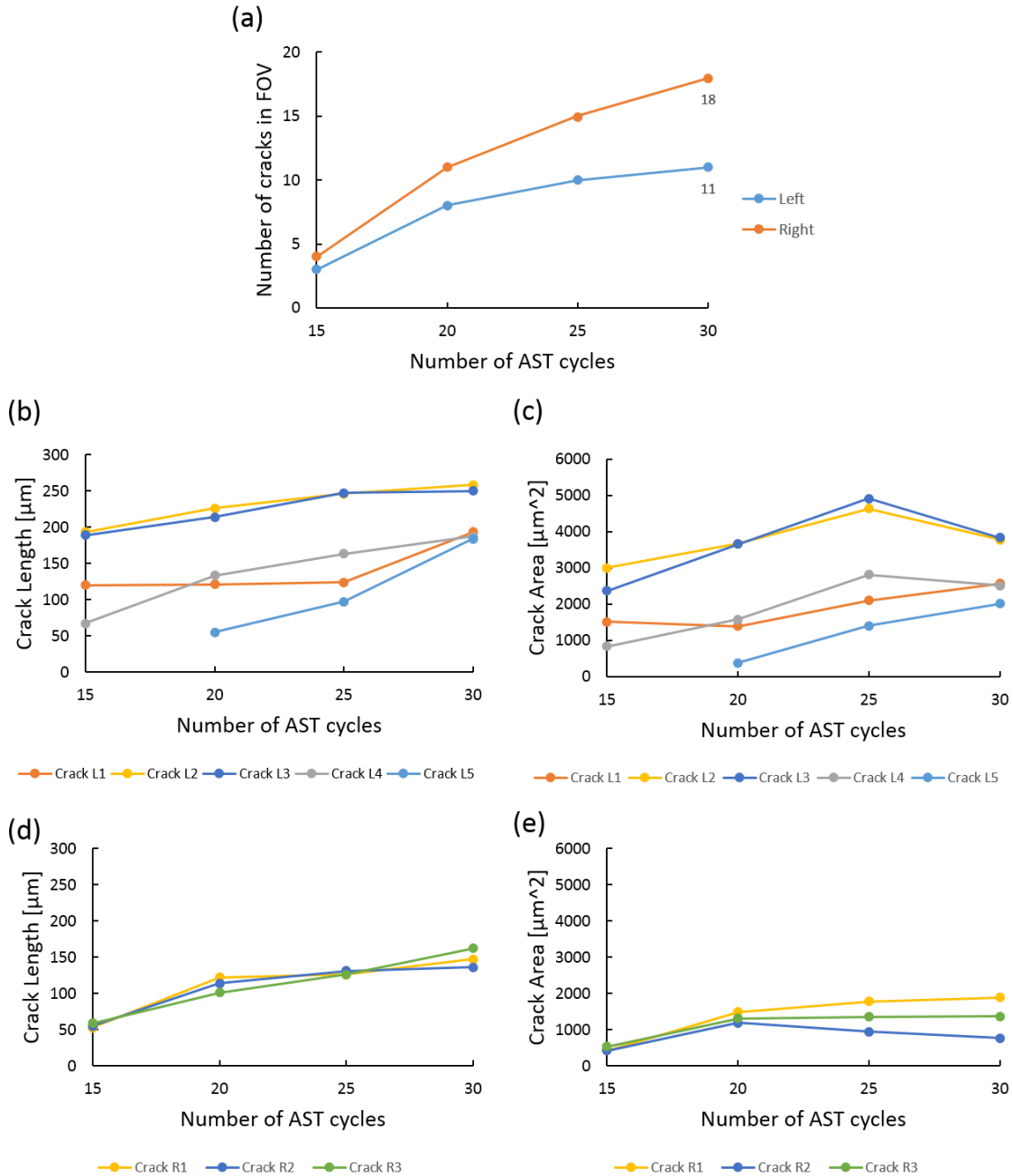
Figure 38: Design 2 membrane edge crack quantitative analysis: (a) number of edge cracks longer than 50 μm; (b) L1-L5 crack length over time; (c) L1-L5 crack area over time; (d) R1-R3 crack length over time; and (e) R1-R3 crack area over time. L = left edge; R = right edge.

Performance Loss Analysis

Although the membrane edge cracks were not completely eliminated in design 2, their size and associated impact on cell performance was clearly reduced in comparison to design 1. As described earlier, edge cracks in design 2 were mostly confined within the narrow adhesive region, where the concentration of gases that could crossover through these cracks is likely to be low due to the local sealing effect provided by the overlying adhesive. Average OCV and ELDT trends for design 2 are shown in Figure 35. From the OCV plot, there was a mild drop of 60 mV in the 15th – 20th cycle period, which could be attributed to the rapid edge crack initiation and propagation that also occurred during this period (Figure 37(c)). The ELDT measurements also indicated negligible convective crossover of hydrogen up to the 20th cycle. Significant hydrogen crossover signals, however, began to be detected at the 25th cycle when sizeable through-thickness membrane cracks started forming in the active area (more details in Section 3.2), and this active area membrane damage eventually led to the cell failure by the 31st cycle. Accordingly, it is established that the MEA edge design strategies adopted as part of design 2 were able to sufficiently limit the membrane edge crack phenomenon, such that the overall membrane damage and its corresponding effects on performance diagnostics were focused primarily in the MEA active area.

Another factor that could limit the effect of membrane edge cracks on cell performance is the MEA humidification. As indicated in Figure 37 (a) and (c), both left and right edge cracks in design 2 were almost completely closed under fully hydrated environment. The steady state OCV hold phase of AST cycling were conducted approximately under 50% relative humidity (Table 3). As a result, edge cracks should be partially closed and the size should be smaller than that indicated in the dry scan. It is clarified that the effect of humidity on membrane crack sizes discussed herein is likely a generally applicable phenomenon, and is not intended to be presented as a specific advantage of design 2. While nominal misalignment of anode and cathode gasket layers is expected with research scale MEA assembly techniques, in the results obtained with design 2 suggest that up to about 100 μm misalignment between the gasket layers can be acceptable from a fuel cell performance and durability perspective.

3.2. Active Area Degradation Analysis

Active area refers to the region where fuel cell reactions take place. Most degradation studies [16,44,81] focus on the active area because stresses are typically heavier in this region and more influential for overall fuel cell performance and durability. In this section, active area membrane degradation of the MEA with edge design 2 is discussed, which is believed to have larger impact on performance loss than edge effects. On the other hand, MEA with edge design 1 did not demonstrate any significant active area degradation due to earlier membrane failure at the edge region.

3.2.1. Electrochemical Diagnostics

As can be seen from Figure 35, the small scale MEA with edge design 2 failed at 31st cycle due to massive OCV loss that exceeds the 20% OCV loss failure criterion. As indicated in the plot, mild to moderate voltage decay was observed from BOL to 26th AST cycle. Comparing to BOL voltage at 0.918 V, the average OCV after 26 AST cycles decreased by merely 7%, to 0.855 V. As a result, the average voltage decay rate was 2.4 mV/cycle for the first 26 AST cycles, representing the mild voltage decay region. Massive voltage loss happened in the last five AST cycles which was accompanied by measurable ELDT signal. The average voltage decay rate from 26th to 30th cycle was 22 mV/cycle, approximately 9 to 10 times larger than for the mild decay region. Additionally, the last AST cycle experienced an abrupt voltage dip of 214 mV, leading to ultimate MEA failure. Comparing to BOL OCV, the EOL OCV had decreased by almost 40%, to 0.554 V. ELDT results correlated well with the OCV decay trend. The ELDT ΔOCV diagnostic remained at zero or negligible level during the entire mild and moderate voltage decay period. However, it suddenly increased to 46 mV at the 25th cycle when the OCV started to show significant loss. The ΔOCV increased linearly during the last five AST cycles and ended up with 100 mV at EOL. The OCV and ELDT trend reported here is comparable with previous COCV AST studies on larger scale technical cells and stacks [81], where the OCV was also observed to have mild decay in early degradation stage but suddenly started to drop dramatically near EOL and the ΔOCV exhibited sudden and linear increase near the ultimate failure. According to a previous report [60], the dramatic OCV loss is likely induced by through-plane membrane cracks that allowed convective hydrogen crossover to happen. It can also be learned that membrane

degradation would only cause minor performance loss in the early stage, but will induce significant performance loss when deformation accumulates and critical features such as through-thickness cracks are formed.

In addition to OCV and ELDT, several other diagnostic parameters were also tracked (Figure 39), including HFR (Figure 39(a)), C_{dl} (Figure 39(b)), and EPSA (Figure 39(c)). CV and EIS curves used to derive these parameters are demonstrated in Appendix B. As can be seen from the plots, there was no observable increasing or decreasing trend in HFR through the entire lifetime except a spike at the 20th cycle which was due to insufficient cell compression and therefore considered an outlier. Insufficient stack compression could introduce higher contact resistance among MEA components and lead to higher HFR. Nevertheless, such contact loss is reversible and can be simply fixed by applying appropriate stack compression. As a result, the overall cell resistance had negligible change during the entire AST. Double layer capacitance was maintained at around 4.7 mF (9.1 mF/cm^2) except for a mild rise at the 15th cycle and a mild dip at EOL. A CCL corrosion induced initial rise followed by a decreasing trend of C_{dl} was previously reported by White et al. [86], with the explanation of initial capacitance increase due to carbon oxidation and later capacitance decrease due to carbon-oxygen surface corrosion. Considering the limited data points obtained in this work, the variation of C_{dl} was comparatively minor, albeit approximately following the same trend, possibly suggesting minor carbon support oxidation and corrosion. C_{dl} for the entire lifetime also falls into the reasonable range reported by Springer et al. [89] EPSA on the other hand showed a decreasing trend for the entire lifetime with some minor fluctuations. This indicates that the present AST affected the Pt catalyst more significantly than the carbon support. Both the chemical and mechanical stressors applied in this work may have influenced the CCL health, with specific consequences for the Pt active surface area; for instance, ionomer degradation may have caused loss of structural integrity and the OCV potential hold and cyclic stress application may have caused Pt dissolution and agglomeration. Pt agglomeration can also take place as a result of carbon corrosion. All these effects are reducing the amount of active Pt and associated EPSA.

Performance of the cell was measured by polarization curve, as indicated in Fig.40. The BOL cell performance was slightly lower than that of the MEA with edge design 1 reported in part 1 of this work, which is likely due to the more restricted gas diffusion induced by the increased active area. There was a considerable performance loss

64

initiated from BOL to the 5th AST cycle across activation, ohmic, and mass transportation regions, which is likely correlated to the initial HFR uptick and EPSA drop showed in Fig.39. Another major performance loss was captured from the 15th AST cycle to 20th AST cycle where activation, ohmic, and mass transport loss all became significant. This primarily coincided with the initial rise in ELDT. Besides, conductivity loss due to carbon corrosion at the CCL will likely introduce more ohmic loss[86], and ionomer fragments being deposited on GDL which causes hydrophilic surface and flooding will like introduce more mass transport loss [60]. Major membrane damage was also initiated within this timeframe, which will be covered in detail next. Polarization curve measurement was not feasible at EOL due to significant OCV loss and fuel cell instability, as a consequence of membrane failure.
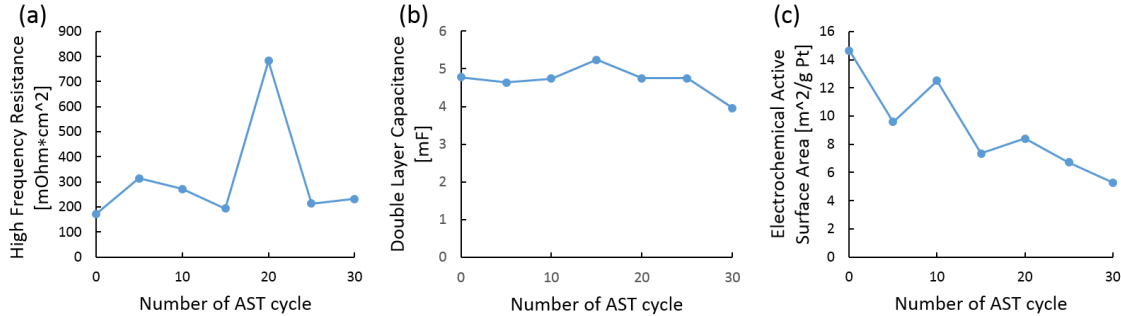

Figure 39: MEA edge design 2 electrochemcial diagnostics results: (a) high frequency resistance; (b) double layer capacitance; and (c) effective platinum surface area.
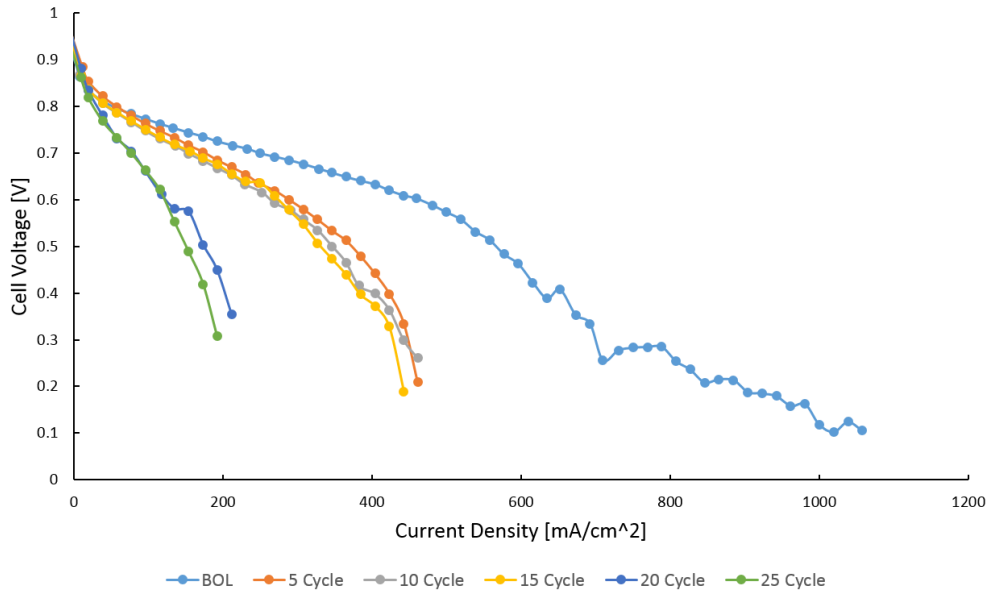

Figure 40: Polarization curve of the MEA with edge design 2.

3.2.2. Morphological Analysis

3D visualization by XCT is capable of detecting failures such as membrane and catalyst layer cracks, pinhole formation, and delamination [16,44,81]. However, similar features could also exist at BOL and have impact on ultimate membrane failure [53]. Hence, visualization at early life stages is also important, ideally with a 4D identical-location imaging methodology. In the present work, 4D visualization of the two flow channels were performed separately as demonstrated in Figure 13(b) due to the limitation of FOV. Figure 41 indicates the planar view of the membrane across the full width of the MEA at BOL and EOL. As can be seen from the figure, left channel membrane (Figure 41(a)) was crack free while right channel membrane (Figure 41(b)) already had one partial crack formed at BOL. Referring to the cross-sectional view of this existing crack (Figure 41(e)), part of the membrane was missing on anode side but the cathode side remained unharmed. According to the EOL images (Figure 41(c)-(d)) after 31 AST cycles, several through-thickness "wide I-shaped" membrane cracks without branching were formed under both channels. Unlike the crack types previously reported by Ramani et al. [81], only "I-shaped" cracks were observed in the present work while "Y-shaped" and "X-shaped" cracks were not observed at all. Moreover, the "I-shaped" crack reported in previous works had larger aspect ratio while in the present work they were widely open and closer to circular shape. Through-plane cracks in the MEA active area were first observed under both channels after the 25th AST cycle. Although some of the cracks were already initiated after the 20th cycle, they had not yet grown into through-thickness cracks and should not cause any measurable rise in internal gas crossover. Crack propagation from 25th cycle to EOL was significant. Under the left channel, all three through-plane cracks captured in the FOV at EOL were not present or could be barely distinguished at the 25th cycle. The right side image showed a similar trend that all cracks propagated significantly during the last five AST cycles. The comparison of active area membrane and CL cracks between 25th cycle and EOL is demonstrated in Appendix C. The crack propagation indicated by the images is in good agreement with the massive OCV decay in the last five AST cycles (Figure 35). Therefore, it is concluded that the formation of through-thickness membrane cracks opened convective hydrogen crossover pathways and was the main reason for ultimate cell failure. It is also noteworthy that all through-thickness membrane cracks were formed in the channel region rather than the land region. Instead of cracks, a number of

membrane "hills" were observed under the lands at both sides, as indicated in Figure 41 (c) and (d). Due to the formation of membrane hills, the overall flatness of the membrane was considerably affected so that several spots appear to be missing in the planar view. In summary, two different membrane degradation modes were observed in the main active area under the combined chemical/mechanical AST: 1) membrane cracks under channel region; and 2) membrane creep under land region. These two degradation mechanisms are analyzed further in the following sections.
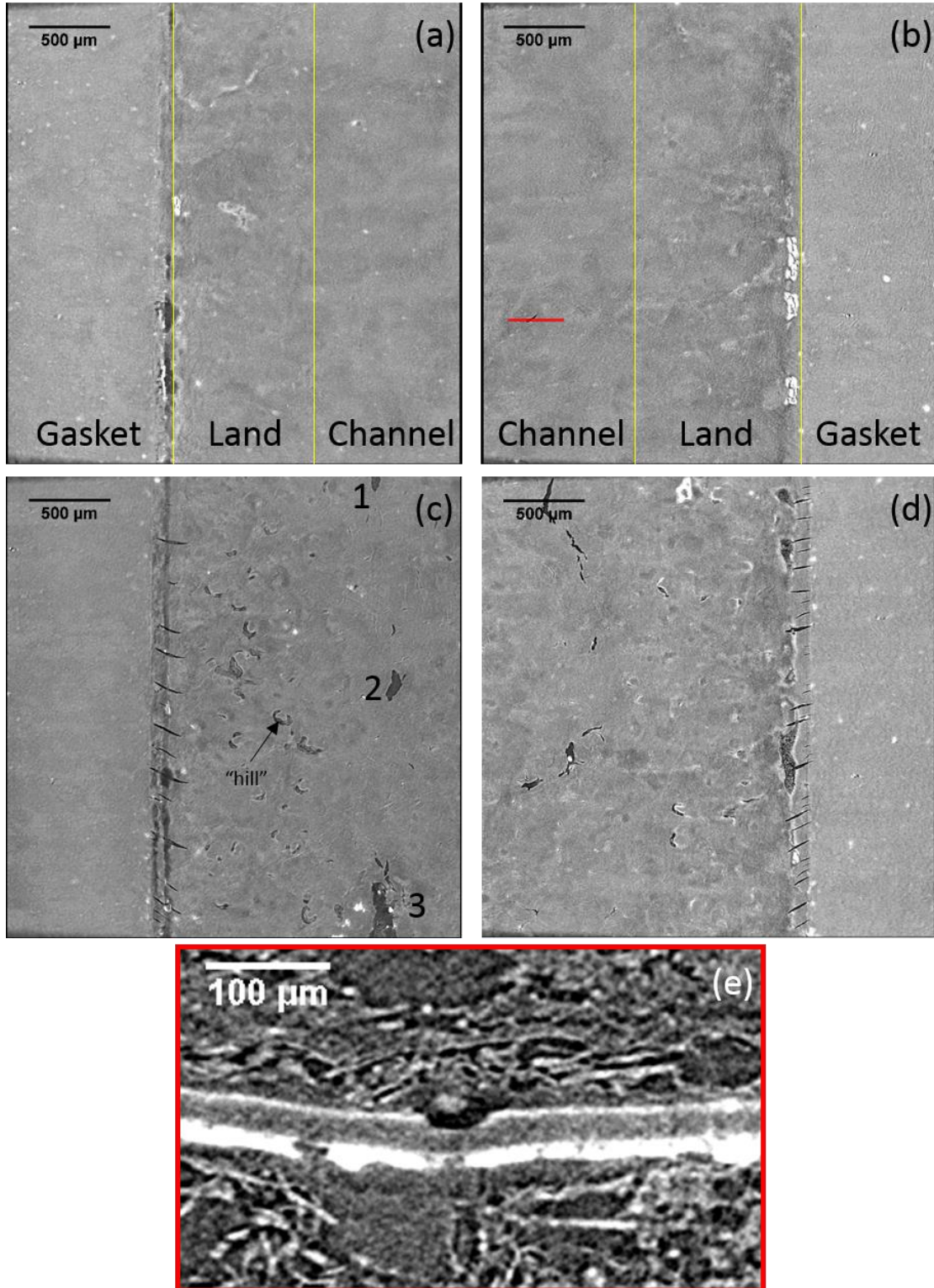
Figure 41: **4D identical-location XCT images of MEA edge design 2: membrane planar view at the (a,c) left and (b.d) right sides of the MEA at (a,b) BOL and (c,d) EOL, covering the full width of the active area; and (e) cross-sectional view of the BOL partial membrane crack under the right channel at the highlighted location in (b).**

Channel Region Analysis

As indicated in Figure 41(c), three through-thickness cracks were observed under the left channel in the dry scan. However, cracks 1 and 3 were only partially captured in 4D visualization. Additional scans were performed at EOL so that all three cracks could be fully observed. Fully captured crack 3 is shown in Figure 42 as the most representative and largest crack in terms of surface area. As can be seen, crack 3 was an inclusive crack with both anode and cathode catalyst layers involved. The corresponding CCL crack (Figure 42(b)) had similar outline as the membrane crack but the ACL crack outline (Figure 42(c)) was significantly larger. Based on measurement results, the surface area of membrane crack, and its corresponding ACL and CCL cracks were $0.108 \mathrm{~mm}^2$, $0.716 \mathrm{~mm}^2$ and $0.160 \mathrm{~mm}^2$ respectively. Referring to the dry state cross-sectional slice shown in Figure 42(d), a large anode platinum agglomeration (diameter $\approx$ $100 \mathrm{~\mu m}$) was observed at the interface of CCM and GDL, which almost extended into GDL voids. However, such agglomeration did not exist at BOL as indicated in Figure 42 (d). Besides, the ACL surface near the crack was almost fully degraded, implying that the agglomerate was formed from disintegrated pieces of ACL material. Several other platinum agglomerations like the one presented in Figure 42(d) were also observed, with those relatively small ones still attached to the CCM but larger ones having the tendency to detach from the membrane surface. CCL on the other hand, was partially remaining at the gap that was created by the crack. Delamination was also present near the crack region, but there were still some platinum residuals attached to the membrane. In terms of membrane deformation, the anode side had a wider opening than the cathode side. It can also be observed that the membrane thickness around the crack was larger than the bulk under dry state. Based on the measured results, the largest membrane thickness near the crack was 35 μm while the average membrane thickness under the channel region was around 22 μm. In wet state, the crack was almost fully closed as depicted in Figure 42(e). Meanwhile, the platinum catalyst that was remaining at the gap was trapped within the closed membrane crack, which could potentially connect anode and cathode GDLs and cause internal shorting. The slight membrane buckling into the cathode GDL leads to compression on the anode side and tension on the cathode side. Considering the wider opening on anode side in dry scan, it is likely that compression caused more mechanical stress concentration than tension so that the crack was initiated from the anode side. Therefore, RH cycling that induced CCM buckling was the main reason for crack formation and propagation while chemical stresses may also have

accelerated this process despite the absence of local membrane thinning. The wide gap created by the crack allowed membrane in-plane expansion during RH cycling, which enables relative slipping motion between CL and MPL. Both CL and MPL surfaces were relatively rough [53] so that catalyst layer deformations such as detachment and agglomeration that was observed in the images could happen during the slipping. Once agglomeration grows into certain size it will detach from the membrane surface and move into GDL pores, such as the one showed in Figure 42(d). The two other cracks under the left channel as well as the cracks under the right channel were similar to crack 3 in terms of morphology except that CL agglomeration and delamination was less significant, thus their planar views were not shown here for brevity. Most membrane cracks under the two flow channels were buckling driven cracks. In general, two types of membrane buckling were observed, either with or without pores involved. However, they can be classified into more detail, as illustrated in Figure 43. Crack 4 (Figure 43(a)) represents a typical buckling driven crack without pores involved. As can be seen in the wet phase image, significant membrane buckling into cathode GDL was present while large void or pore was not observed in either anode or cathode GDL. Crack 5 and 6 (Figure 43(b)) were two buckling driven cracks with pores involved. Referring to the dry phase image, the MPL surface under crack 5 was not perfectly bonded to CCM and slightly concave so that a gap was present between CCM and MPL, and a large pore was observed in the anode GDL above crack 6. According to Prass et al. [55], MPL tends to sag into GDL pores and form cracks due to insufficient mechanical support. As a result, crack 5 was buckling into the gap on the cathode MPL while crack 6 was buckling into the pore on the anode GDL in wet condition. Neither of these two cracks had grown into through-thickness membrane cracks yet at EOL, proving that buckling driven cracks are initiated from one certain electrode and gradually penetrate the entire membrane. The difference of buckling direction caused the two cracks to initiate from different electrodes, supporting the hypothesis that cracks always start from the electrode under compression. However, the membrane was not always buckling into gaps or pores, with crack 7 (Figure 43(c)) as an example. A large anode GDL pore was present above crack 7, but instead the membrane slightly buckled into cathode GDL which opened the crack from the anode side rather than from the cathode. Other than GDL and MPL pores, spots with missing CL could also cause membrane stress concentration and generate cracks. As shown in Figure 43(d), part of the CCL was missing under crack 8, causing the membrane to expand into this void during RH cycling

and generate compression on the anode side. Therefore, missing CL, especially CCL, could create voids with enough size to cause membrane cracks. In addition, certain pre-existing membrane features may also influence crack formation. As depicted in Figure 43(e), local membrane deformation was present on the anode side at BOL, labelled as crack 9. After 31 AST cycles, this initial membrane deformation propagated in terms of size but was not able to penetrate the membrane. Meanwhile, CCL crack and delamination was observed underneath crack 9, which can be explained by the tension generated by membrane buckling in the wet phase. If time permits, crack 9 was deemed likely to become another through-thickness crack.

Unlike the previous studies using GDE based MEAs [44,60,81], exclusive membrane cracks without CLs involved were not observed in the present work. All cracks were accompanied by corresponding CL cracks since all crack modes analyzed above were mainly mechanical stress driven and accelerated by chemical mechanisms. Moreover, the bonding between CL and MPL is weaker in CCM based MEAs assembled without hot pressing, which could potentially leave gaps between CCM and GDL. The current edge sealing structure also limited in-plane membrane expansion, forcing the membrane to undergo through-plane expansion during wet phase. Combining these aspects, the mechanical stresses were leveraged in the active area. Therefore, through-plane mechanical deformation such as buckling was dominating membrane crack formation and failure. Chemical stress on the other hand, was considered to be moderate comparing to mechanical stress since exclusive membrane crack which is typically driven by chemical mechanisms was not observed. Moreover, membrane thinning was not observed in the channel region. According to the XCT measured results, the membrane thickness was around 22 µm in dry state at both BOL and EOL, representing negligible thickness reduction. However in previous studies, up to 50% membrane thickness reduction was achieved at EOL, which is driven by radical chemical species attack [60]. Chemical stress was still likely to accelerate the overall membrane degradation by the induced loss of mechanical membrane properties [16] but was not creating any additional crack in the present work.

71
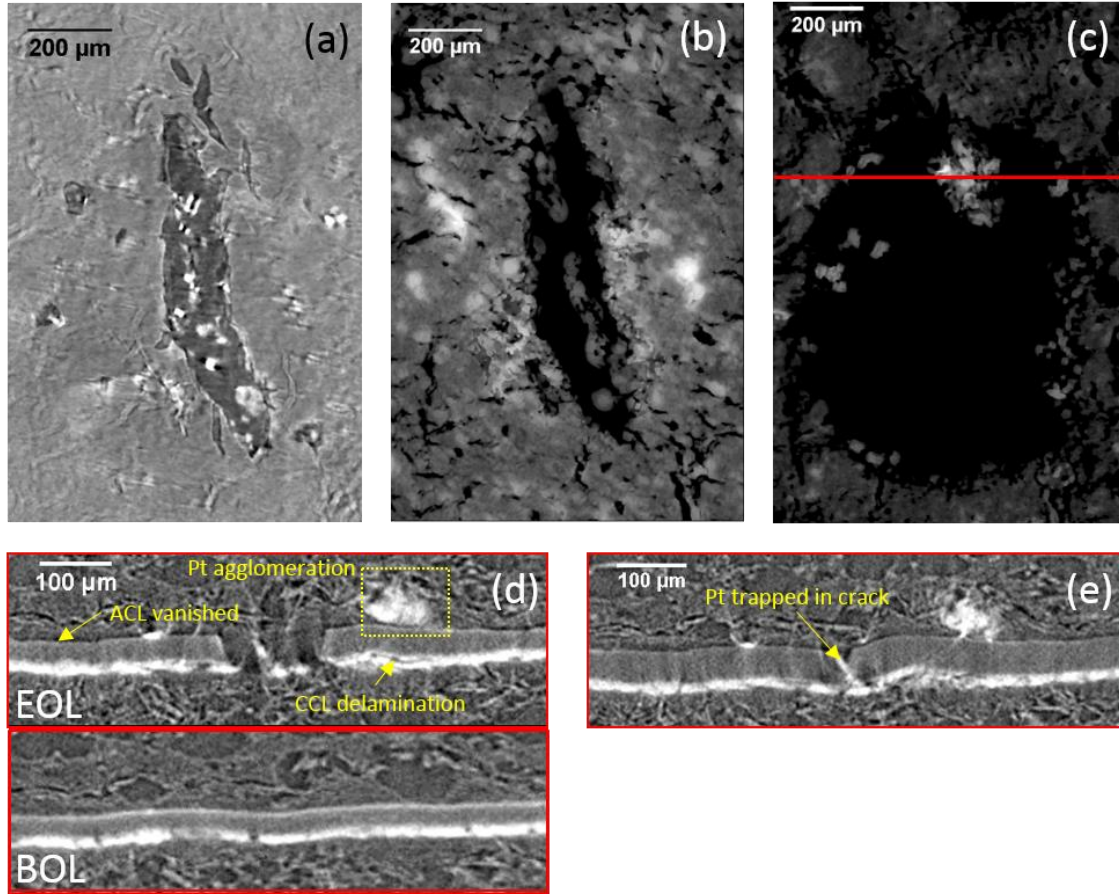
Figure 42: Detailed analysis of crack 3 at EOL: (a) planar membrane view under dry state; (b) planar CCL view under dry state; (c) planar ACL view under dry state; (d) cross-sectional MEA view at the highlighted location under dry state at both EOL and BOL; and (e) cross-sectional MEA view at the highlighted location under wet state.
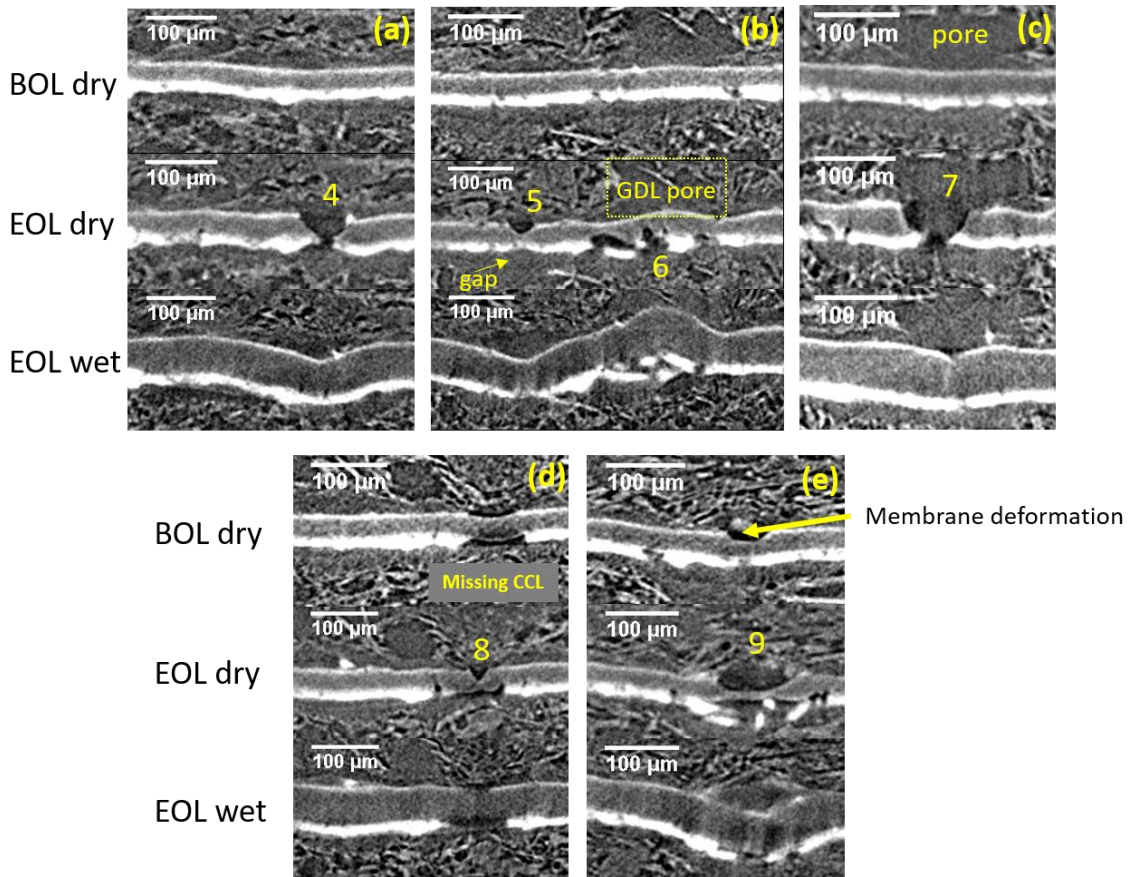
Figure 43: Detailed 4D analysis of various membrane cracks (a) without macro GDL pore, (b) with macro GDL pore, (c) with GDL pore present but with no visible effect, (d) with missing CCL, and (e) with local membrane deformation at BOL.

Land Region Analysis

In the land region where the MEA is compressed by the flow field plates, membrane creep was the dominant degradation mode that created the "hills" as illustrated in Figure 44. Such membrane creep spots were observed under both left and right land regions as well as the middle land region between the two flow channels. Over 100 creep spots were observed in the land region within the entire FOV, with most of them protruding into anode GDL and only few into cathode GDL. All anode creep spots were related to GDL pores and two representative spots are indicated in Figure 44(a). At BOL, large anode GDL pores were observed at both creep spots while at EOL the pores were filled with membrane. Referring to the crack formation mechanism discussed in the previous section, it can be inferred that creep was also caused by through-plane membrane expansion and shrinkage during repeated RH cycling. In the channel region, the membrane could push the GDLs into the flow channel during swelling so that stress

73

between CCM and GDL is partially released. However, the GDL portion under the land region is constrained by the plates and therefore stress is accumulated at the CCM / MPL interface. For the membrane, in-plane expansion is restricted by the frame structure, and through-plane expansion is also partially restricted by the plate. As a result, MPL infiltration into the GDL substrate is likely to happen due to stress concentration, especially at the locations that lack GDL substrate support. The MPL infiltration provided membrane expansion space, thus facilitated membrane creep. Referring to the morphology of anode creep spots in Figure 44(a), ACL agglomeration was observed in both creep spots. During the RH cycling, membrane was forced to expand and creep into GDL pores. Simultaneously, the ACL was locally compressed to become a large agglomerated particle. Such agglomeration would also cause anode EPSA deduction. Moreover, some of the anode catalyst even detached from the CCM and reattached to the GDL surface, which was possibly due to stress concentration at the interface between CCM and MPL. Membrane and CCL cracks were also observed in Figure 44(a). Similarly to the crack forming mechanism, the cathode side was under compression when the membrane was bent into the anode GDL. The cyclic compression caused membrane and CCL to crack. However, the cracks did not propagate further because the local membrane thickness dramatically increased due to the creep, which counteracted the bending. Figure 44(b) shows a creep into cathode GDL which was rarely seen in the FOV. At BOL, a cathode GDL pore with relatively large size was observed, and this pore was filled by membrane material at EOL, indicating mechanical MPL failure. There was also significant CL delamination associated with this creep. However unlike anode creep, CL compression was not observed in this cathode creep. Generally, the pore size of the cathode GDL was smaller than for the anode GDL. Besides, thicker CL on cathode yields higher mechanical strength and helps prevent membrane creep to some extent. Other than deformation on membrane itself, membrane swelling can also bring negative impact on GDL structure and porosity. During membrane swelling, GDL is compressed and permanent structural damage can occur. GDL structural collapse will reduce porosity so that gas diffusion and water removal are both affected, which may lead to additional cell performance loss.
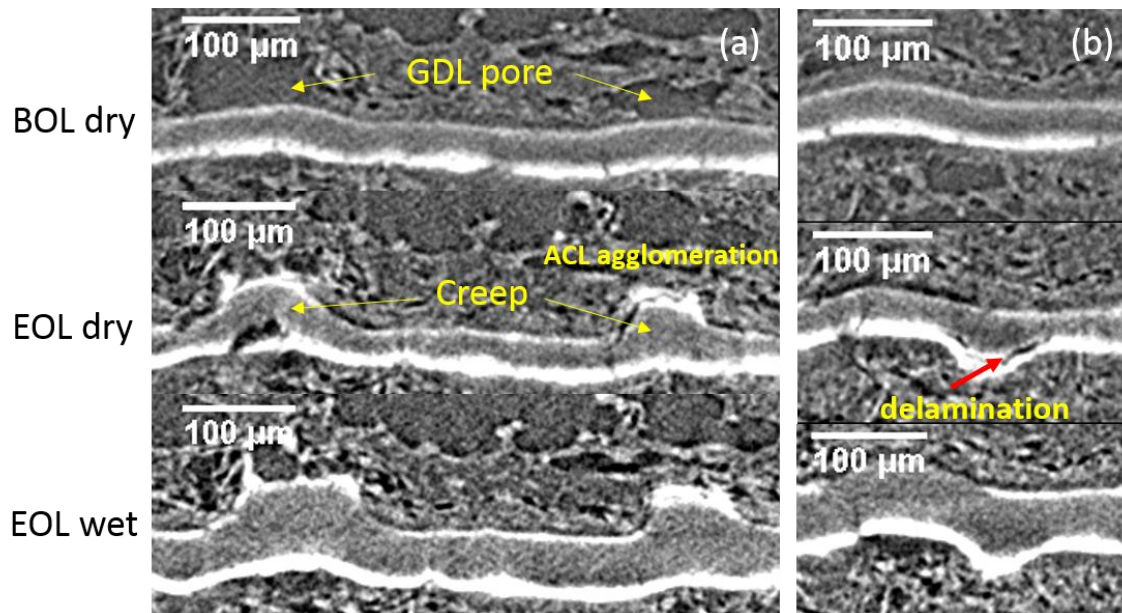
Figure 44: Membrane creep into (a) anode GDL and (b) cathode GDL.

Chapter 4.   Conclusion

The work presented in this thesis aimed at understanding the fundamentals and root cause of combined chemical and mechanical fuel cell membrane degradation in both active area and edge regions. A subsequent frame sealing technique based edge design equipped with suitable mitigations was first proposed based on preliminary findings from the original design. The subsequent design was then subjected to the combined chemical and mechanical AST. With 4D *in situ* visualization and diagnostic methods, efficacy of the implemented mitigations was verified, and membrane damage occurring within the active MEA area was effectively analyzed.

In this work, a Greenlight® G20 fuel cell test station and a laboratory based ZEISS Xradia® 520 Versa micro XCT system was cooperatively used to perform 4D *in situ* membrane degradation analysis. In order to study the root cause of membrane degradation in edge regions, two different MEA edge designs were examined, wherein the first design was used to identify and understand the mechanisms of membrane edge failure and the second design was purposely refined with an aim to mitigate edge failures encountered in the first design. In design 1, membrane cracks in the edge region covered by Teflon®-Kapton® gasket layers were detected by the 9th AST cycle, which was accompanied by OCV decay and introduction of fluctuations. These cracks formed at the two lateral edges perpendicular to the flow field direction, extended up to 1000 µm in length, and their willow leaf shapes indicated mechanical stresses as the likely driving mechanism. A separate damage feature, which was significantly larger than the edge cracks and may have been formed by combined chemical/mechanical stressors, was also detected under the extended Kapton® layer covering the CCM, and likely resulted in significant hydrogen crossover. The propagation of edge cracks was found to have an upper limit, and their extension into the active area was constrained by the gasket layers. The cell failure, however, in the 22nd AST cycle was primarily characterized with these membrane edge damage features without any sizeable membrane damage in the active area. Additionally, adhesive accumulation and membrane wrinkling were observed at the longitudinal edges under the flow channel, which was driven by non-uniform compression between land and channel regions. Membrane wrinkling resulted in longitudinal edges being squeezed and lateral edges getting stretched, which facilitates

lateral edge crack formation. Kapton® layer with adhesive that is attached to the CCM in order to prevent the CCM's permanent creep deformation under AST conditions was identified as the primary contributor in the formation of these membrane edge failures, while incomplete active area coverage which induced membrane wrinkling was identified as the secondary contributor.

In the subsequent design 2, the positions of Teflon® and Kapton® layers were switched to minimize CCM deformation from the likely flow of adhesive at elevated temperature and humidity, while also increasing the MEA active area to achieve complete coverage of flow channel lengths by GDLs that could improve the overall uniformity of clamping compression. In this new design, membrane edge cracks formed in the small gap between the gasket layer and GDL boundaries, and importantly, their growth was restricted to this region possibly from additional constraints provided by the adhesive accumulated in this region. In design 2, the size of major edge cracks was nearly five times lower than design 1 and no other type of major membrane damage features were detected at the edges. Moreover, the development period of edge cracks was also slightly delayed, occurring mainly from 10-20 cycles and accompanied by a mild OCV decay of about 50 mV. Subsequent severe membrane damage and associated effects on performance diagnostics (OCV decay and crossover leak) were linked to microstructural changes in the MEA active area. Although edge degradation was not completely absent through the mitigations implemented in design 2, the redesigned edge had sufficient mechanical robustness to eliminate edge failure and sustain the operation of the small scale MEA, thereby allowing investigation of targeted combined chemical/mechanical membrane degradation in the active area. It is also noticeable that the edge crack features are highly dependent on the artifacts generated during assembly such as gasket misalignment, adhesive overflow, and interfacial gap between gasket and active area. These artifacts will vary slightly from cell to cell, which may affect some of the edge crack properties such as length, orientation, and time of formation.

In terms of active area membrane degradation under combined chemical and mechanical AST, membrane crack was the dominant failure in the flow channel region while membrane creep was the main deformation observed in the land region. According to *in situ* diagnostic results, most cell performance losses occurred in the last five AST cycles (26th to 31st cycle) which was attributed to internal hydrogen crossover. Based on

77

4D image analysis, through-thickness membrane cracks were first observed at the 25th AST cycle and rapidly propagated thereafter. Therefore, it was confirmed that membrane crack was the dominating degradation mode causing massive gas crossover. Most membrane cracks were driven by membrane buckling during RH cycling when membrane underwent cyclic swelling and shrinking. The MEA frame design 2 limited in-plane membrane expansion to a great extent so that through-plane membrane expansion was dominant. Based on cross-sectional image analysis, most membrane buckling was due to weak bonding between CCM and MPL, large pores in GDL, missing catalyst layer, and membrane deformation that created gaps so that the stresses acting on anode and cathode sides of the CCM were not balanced. As a result, buckling occurred and created bending stress inside the membrane. Through morphological analysis, all membrane cracks related to buckling were initiated from the catalyst layer surface under compression, and gradually propagated into the membrane. Comparing to previous pure chemical and combined chemo-mechanical degradation studies, membrane thinning and exclusive membrane crack were not observed. Moreover, branching during in-plane crack propagation that was exclusively discovered in larger GDE based MEAs subjected to COCV AST was not observed in the present work either. Referring to these facts, chemical stress was considered moderate in the current combined chemical/mechanical AST protocol.

Instead of cracks, membrane creep was exclusively observed in the land region where the graphite flow field plates constrained through-plane membrane expansion. For most creep spots, membrane filled the macro pores beneath MPL in anode GDL and formed "hills". During the wet phase in RH cycling, stress concentration was present at the interface of CCM and MPL. The existence of macro pores in GDL led to insufficient mechanical support to MPL and thus caused MPL to collapse under high compression. Most creep spots were found in anode due to the fact that ACL was thinner than CCL and macro pores in anode GDL were generally larger than in cathode GDL. Catalyst layer agglomeration was also observed at creep spots. Gas diffusion and water removal may be negatively influenced due to this GDL over compression and membrane creep filling up the pores. However, the impact of creep on cell performance loss was considered mild comparing to the effect of membrane cracks that enabled massive gas crossover. Compared to the edge region, the active area is much less sensitive to the artifacts during assembly. Therefore, the membrane failure modes in the active area are

more representative and reproducible. Their properties are not expected to significantly vary from cell to cell.

In the frame mitigation study, the local membrane thinning issue in design 2 at BOL was observed with the help of 4D *in situ* visualization technique, and the thinning was believed to have created stress concentration and facilitated edge crack formation. Additionally, the gap between gasket layer and GDL results in insufficient mechanical support for membrane so that it is prone to crack at this region. Nevertheless, the current design mitigations have demonstrated reliable execution of the combined chemical and mechanical AST to produce failures in the desired regions of interest. Again thanks to the 4D *in situ* visualization technique, the acquisition of both dry and wet MEA images in the same FOV as well as the evolution of membrane damage were enabled, which provided a thorough understanding on membrane degradation mechanisms, especially the interaction between CCM and other MEA and cell components under various working environments. The capability of tracking failure evolution allowed the correlation between *in situ* diagnostic results and MEA images at each corresponding life stage to be built, which yielded a better understanding of the exact reasons of cell performance loss at each given life stage. Taking the present work as an example, it was discovered that edge degradation of MEA design 2 was not critical to performance loss but active area cracks was the dominating failure mode. Such conclusion cannot be drawn without the support of intermediate MEA images. In the opinion of the author, the adopted 4D *in situ* imaging methodology played a key role in revealing the mechanisms of edge failure in this work, which have not been previously established. The laboratory based small scale custom MEAs used in this work required manual assembly, which could introduce handling errors, tolerance issues, design-based non-uniformities, and cell-to-cell variations in the highly sensitive MEA edge regions. As demonstrated in this work, the non-destructive XCT-based 4D imaging approach is particularly useful in characterizing such edge issues and understanding their impact on cell performance. Such technique should not be limited to membrane degradation study only, but can also be leveraged in the degradation studies of other relevant fuel cell components and other fuel cell operational issues.

Chapter 5.   Future Work

5.1. Cell Design Modification

Based on experimental results, membrane degradation indicated more mechanical based failures than chemical based failures using this current combined chemical and mechanical AST protocol. Ideally, similar levels of chemical and mechanical stresses are preferred so that their interactions can be better understood. The mild chemical degradation was possibly due to low cell temperature during the OCV hold phase. In the present work, only the anode plate was heated by cartridge heater, while TC was placed in cathode plate to measure the plate temperature. Cartridge heater was set to 95 °C in OCV hold phase, but cathode TC only read around 45 – 50 °C. The significant temperature gradient between heater and TC could be attributed to: 1) Poor contact between heater and endplate; 2) Poor contact between TC and endplate; 3) Inlet gas absorbing heat; 4) Poor heat conduction from anode to cathode; and 5) Heat loss to the surrounding. Among these major heat loss contributors, 1) and 2) were due to the relatively loose fit between heater or TC and their insert, which could be resolved by applying thermal paste before plugging; 3) was due to the inlet gas heat loss in the unheated and uninsulated connection tube between the station and cell, which could be resolved by reducing the length of and insulating the connection tube; 4) could be addressed through plate design modification; and 5) could be mitigated by applying extra insulation material around the cell.

5.2. AST Protocol Modification

The SSF is expected to have the capability of reaching higher cell temperature in the combined AST cycles with appropriate design modification of the graphite plates. Therefore, studies on AST conditions could be carried out to fine tune the present AST protocol to achieve more balanced chemical and mechanical membrane degradation. As mentioned in this thesis, operating conditions such as high temperature, low relative humidity, high voltage, and/or high reactant concentration can accelerate chemical degradation. In the present work, the cell was already maintained at OCV during chemical degradation phase. As a result, temperature, RH, and reactant concentration

can be adjusted. In the author's opinion, conducting AST at 90°C would be a good starting point. The membrane will however have the risk of going through glass transition if the temperature exceeds 100°C. Dew point temperature could remain at 60°C, which would result in relatively low RH of 28%. In addition, higher reactant concentration could be applied as well, i.e. using higher oxygen concentration on the cathode side. For instance, 40% oxygen mix with nitrogen could be used as a starting point to replace air [46], which would roughly double the oxygen concentration.

5.3. Mitigated Frame Design Application

The most tangible outcome from the present work is the mitigated MEA frame design, which is capable of withstanding combined chemical and mechanical AST that represents actual fuel cell operation from beginning to end of life. A minor drawback of this mitigated frame design is the local membrane thinning at gasket edges induced by local stress concentration. For future study, thinner Teflon® and/or Kapton® gasket layers can be tested for stress concentration relief. Other frame designs based on PEM direct sealing or wrapped sealing techniques can also be proposed and tested for comparison. The test stand and methodology used in this work could also be leveraged in other fuel cell degradation studies. For instance, the Nafion® NR211 membrane could be replaced by ePTFE reinforced membrane or hydrocarbon based membrane, to study and compare the degradation mechanism of different types of PEM. Moreover, adjacent CL and GDL components could be modified to study interactions between different MEA components. Overall, the capability of 4D *in situ* visualization and this mitigated frame design is only partially realized at the current stage, and further research is recommended to thoroughly understand PEMFC degradation and develop suitable durability mitigation strategies.

References

[1] D.S. Lemmen, Canada's Changing Climate Report, (n.d.) 444.

[2] E. and C.C. Canada, Greenhouse effect, Aem. (2008). https://www.canada.ca/en/environment-climate-change/services/climate-change/greenhouse-effect.html (accessed January 27, 2020).

[3] E. and C.C. Canada, Greenhouse gas emissions, Aem. (2007). https://www.canada.ca/en/environment-climate-change/services/environmental-indicators/greenhouse-gas-emissions.html (accessed January 27, 2020).

[4] Ryan P. O'Hayre author, Fuel cell fundamentals / Ryan O'Hayre, Suk-Won Cha, Whitney G. Colella, Fritz B. Prinz., Third edition., Wiley, Hoboken, New Jersey, 2016.

[5] M.M. Mench, Fuel cell engines / Matthew M. Mench., Hoboken, NJ: John Wiley & Sons, 2008.

[6] T. Yoshida, K. Kojima, Toyota MIRAI Fuel Cell Vehicle and Progress Toward a Future Hydrogen Society, Electrochem. Soc. Interface. 24 (2015) 45–49. https://doi.org/10.1149/2.F03152if.

[7] O. Bahn, M. Marcy, K. Vaillancourt, J.-P. Waaub, Electrification of the Canadian road transportation sector: A 2050 outlook with TIMES-Canada, Energy Policy. 62 (2013) 593–606. https://doi.org/10.1016/j.enpol.2013.07.023.

[8] M. Sykes, J. Axsen, No free ride to zero-emissions: Simulating a region's need to implement its own zero-emissions vehicle (ZEV) mandate to achieve 2050 GHG targets, Energy Policy. 110 (2017) 447–460. https://doi.org/10.1016/j.enpol.2017.08.031.

[9] Fuel Cell Technologies Office Multi-Year Research, Development, and Demonstration Plan, Energy.Gov. (n.d.). https://www.energy.gov/eere/fuelcells/downloads/fuel-cell-technologies-office-multi-year-research-development-and-22 (accessed January 27, 2020).

[10] A.S. Alavijeh, M.-A. Goulet, R.M.H. Khorasany, J. Ghataurah, C. Lim, M. Lauritzen, E. Kjeang, G.G. Wang, R.K.N.D. Rajapakse, Decay in Mechanical Properties of Catalyst Coated Membranes Subjected to Combined Chemical and Mechanical Membrane Degradation, Fuel Cells. 15 (2015) 204–213. https://doi.org/10.1002/fuce.201400040.

[11] S. Zhang, X.-Z. Yuan, J.N.C. Hin, H. Wang, K.A. Friedrich, M. Schulze, A review of platinum-based catalyst layer degradation in proton exchange membrane fuel cells, Journal of Power Sources. 194 (2009) 588–600. https://doi.org/10.1016/j.jpowsour.2009.06.073.

[12]   J. Park, H. Oh, T. Ha, Y.I. Lee, K. Min, A review of the gas diffusion layer in proton exchange membrane fuel cells: Durability and degradation, Applied Energy. 155 (2015) 866–880. https://doi.org/10.1016/j.apenergy.2015.06.068.

[13]   DOE Technical Targets for Fuel Cell Transit Buses, Energy.Gov. (n.d.). https://www.energy.gov/eere/fuelcells/doe-technical-targets-fuel-cell-transit-buses (accessed September 7, 2019).

[14]   DOE Technical Targets for Polymer Electrolyte Membrane Fuel Cell Components, Energy.Gov. (n.d.). https://www.energy.gov/eere/fuelcells/doe-technical-targets-polymer-electrolyte-membrane-fuel-cell-components (accessed September 7, 2019).

[15]   J. Wu, X.Z. Yuan, J.J. Martin, H. Wang, J. Zhang, J. Shen, S. Wu, W. Merida, A review of PEM fuel cell durability: Degradation mechanisms and mitigation strategies, Journal of Power Sources. 184 (2008) 104–119. https://doi.org/10.1016/j.jpowsour.2008.06.006.

[16]   Y. Singh, F.P. Orfino, M. Dutta, E. Kjeang, 3D visualization of membrane failures in fuel cells, Journal of Power Sources. 345 (2017) 1–11. https://doi.org/10.1016/j.jpowsour.2017.01.129.

[17]   H.-F. Lee, M. Killer, B. Britton, Y. Wu, H.-D. Nguyen, C. Iojoiu, S. Holdcroft, Fuel Cell Catalyst Layers and Membrane-Electrode Assemblies Containing Multiblock Poly(arylene ether sulfones) Bearing Perfluorosulfonic Acid Side Chains, J. Electrochem. Soc. 165 (2018) F891–F897. https://doi.org/10.1149/2.1081810jes.

[18]   L. Ghassemzadeh, T.J. Peckham, T. Weissbach, X. Luo, S. Holdcroft, Selective formation of hydrogen and hydroxyl radicals by electron beam irradiation and their reactivity with perfluorosulfonated acid ionomer, Journal of the American Chemical Society. 135 (2013) 15923–32. https://doi.org/10.1021/ja408032p.

[19]   H. Kim, Multiscale and Multiphysics Computational Frameworks for Nano- and Bio-Systems, Springer New York, New York, NY, 2011.

[20]   A.Z. Weber, J. Newman, Transport in Polymer-Electrolyte Membranes I. Physical Model, J. Electrochem. Soc. 150 (2003) A1008–A1015. https://doi.org/10.1149/1.1580822.

[21]   T. Holmes, T.J.G. Skalski, M. Adamski, S. Holdcroft, Stability of Hydrocarbon Fuel Cell Membranes: Reaction of Hydroxyl Radicals with Sulfonated Phenylated Polyphenylenes, Chem. Mater. 31 (2019) 1441–1449. https://doi.org/10.1021/acs.chemmater.8b05302.

[22]   W. Vielstich, A. Lamm, H.A. Gasteiger, J. Wiley, K. Kordesch, M. Cifrain, Gasteiger H. Handbook of fuel cells, fundamentals technology and applications, 2003.

[23]   G. Maier, J. Meier-Haack, Sulfonated Aromatic Polymers for Fuel Cell Membranes, in: G.G. Scherer (Ed.), Fuel Cells II, Springer, Berlin, Heidelberg, 2008: pp. 1–62. https://doi.org/10.1007/12_2008_135.

[24]   C.H. Park, C.H. Lee, M.D. Guiver, Y.M. Lee, Sulfonated hydrocarbon membranes for medium-temperature and low-humidity proton exchange membrane fuel cells (PEMFCs), Progress in Polymer Science. 36 (2011) 1443–1498. https://doi.org/10.1016/j.progpolymsci.2011.06.001.

[25]   D.W. Shin, M.D. Guiver, Y.M. Lee, Hydrocarbon-Based Polymer Electrolyte Membranes: Importance of Morphology on Ion Transport and Membrane Stability, Chem. Rev. 117 (2017) 4759–4805. https://doi.org/10.1021/acs.chemrev.6b00586.

[26]   C.H. Park, C.H. Lee, J.-Y. Sohn, H.B. Park, M.D. Guiver, Y.M. Lee, Phase Separation and Water Channel Formation in Sulfonated Block Copolyimide, J. Phys. Chem. B. 114 (2010) 12036–12045. https://doi.org/10.1021/jp105708m.

[27]   M.S. Saha, D.K. Paul, B.A. Peppley, K. Karan, Fabrication of catalyst-coated membrane by modified decal transfer technique, Electrochemistry Communications. 12 (2010) 410–413. https://doi.org/10.1016/j.elecom.2010.01.006.

[28]   J.M. Serpico, S.G. Ehrenberg, G.E. Wnek, T.N. Tangredi, Gas diffusion electrode, US5677074A, 1997. https://patents.google.com/patent/US5677074A/en (accessed September 7, 2019).

[29]   Y. Wang, K.S. Chen, J. Mishler, S.C. Cho, X.C. Adroher, A review of polymer electrolyte membrane fuel cells: Technology, applications, and needs on fundamental research, Applied Energy. 88 (2011) 981–1007. https://doi.org/10.1016/j.apenergy.2010.09.030.

[30]   S. Park, J.-W. Lee, B.N. Popov, A review of gas diffusion layer in PEM fuel cells: Materials and designs, International Journal of Hydrogen Energy. 37 (2012) 5850–5865. https://doi.org/10.1016/j.ijhydene.2011.12.148.

[31]   M.F. Mathias, J. Roth, J. Fleming, W. Lehnert, Diffusion media materials and characterisation, in: Handbook of Fuel Cells, American Cancer Society, 2010. https://doi.org/10.1002/9780470974001.f303046.

[32]   J. Ahn, R. Holze, Bifunctional electrodes for an integrated water-electrolysis and hydrogen-oxygen fuel cell with a solid polymer electrolyte, J Appl Electrochem. 22 (1992) 1167–1174. https://doi.org/10.1007/BF01297419.

[33]   I. Cabasso, Y. Yuan, X. Xu, Gas diffusion electrodes based on poly(vinylidene fluoride) carbon blends, US5783325A, 1998. https://patents.google.com/patent/US5783325A/en (accessed January 29, 2020).

[34] C. Lim, C.Y. Wang, Effects of hydrophobic polymer content in GDL on power performance of a PEM fuel cell, Electrochimica Acta. 49 (2004) 4149–4156. https://doi.org/10.1016/j.electacta.2004.04.009.

[35] S. Park, B.N. Popov, Effect of a GDL based on carbon paper or carbon cloth on PEM fuel cell performance, Fuel. 90 (2011) 436–440. https://doi.org/10.1016/j.fuel.2010.09.003.

[36] A. Woodman, E.B. Anderson, K.D. Jayne, M.C. Kimble, Development of Corrosion-Resistant Coatings for Fuel Cell Bipolar Plates, in: 1999.

[37] X. Li, I. Sabir, Review of bipolar plates in PEM fuel cells: Flow-field designs, International Journal of Hydrogen Energy. 30 (2005) 359–371. https://doi.org/10.1016/j.ijhydene.2004.09.019.

[38] M. Danilczuk, F.D. Coms, S. Schlick, Visualizing Chemical Reactions and Crossover Processes in a Fuel Cell Inserted in the ESR Resonator: Detection by Spin Trapping of Oxygen Radicals, Nafion-Derived Fragments, and Hydrogen and Deuterium Atoms, The Journal of Physical Chemistry B. 113 (2009) 8031–8042. https://doi.org/10.1021/jp901597f.

[39] H. Christensen, K. Sehested, Reaction of hydroxyl radicals with hydrogen at elevated temperatures. Determination of the activation energy, J. Phys. Chem. 87 (1983) 118–120. https://doi.org/10.1021/j100224a027.

[40] H. Christensen, K. Sehested, H. Corfitzen, Reactions of hydroxyl radicals with hydrogen peroxide at ambient and elevated temperatures, J. Phys. Chem. 86 (1982) 1588–1590. https://doi.org/10.1021/j100206a023.

[41] A. John Elliot, D. R. McCracken, G. V. Buxton, N. D. Wood, Estimation of rate constants for near-diffusion-controlled reactions in water at high temperatures, Journal of the Chemical Society, Faraday Transactions. 86 (1990) 1539–1547. https://doi.org/10.1039/FT9908601539.

[42] G.V. Buxton, C.L. Greenstock, W.P. Helman, A.B. Ross, Critical Review of rate constants for reactions of hydrated electrons, hydrogen atoms and hydroxyl radicals ($\cdot$OH/$\cdot$O$^-$ in Aqueous Solution, Journal of Physical and Chemical Reference Data. 17 (1988) 513–886. https://doi.org/10.1063/1.555805.

[43] C. Chen, T.F. Fuller, The effect of humidity on the degradation of Nafion® membrane, Polymer Degradation and Stability. 94 (2009) 1436–1447. https://doi.org/10.1016/j.polymdegradstab.2009.05.016.

[44] Y. Singh, F.P. Orfino, M. Dutta, E. Kjeang, 3D Failure Analysis of Pure Mechanical and Pure Chemical Degradation in Fuel Cell Membranes, Journal of The Electrochemical Society. 164 (2017) F1331–F1341. https://doi.org/10.1149/2.0451713jes.

[45]   S. Kundu, K. Karan, M. Fowler, L.C. Simon, B. Peppley, E. Halliop, Influence of micro-porous layer and operating conditions on the fluoride release rate and degradation of PEMFC membrane electrode assemblies, Journal of Power Sources. 179 (2008) 693–699. https://doi.org/10.1016/j.jpowsour.2007.11.117.

[46]   N. Macauley, A.S. Alavijeh, M. Watson, J. Kolodziej, M. Lauritzen, S. Knights, G. Wang, E. Kjeang, Accelerated Membrane Durability Testing of Heavy Duty Fuel Cells, J. Electrochem. Soc. 162 (2015) F98–F107. https://doi.org/10.1149/2.0671501jes.

[47]   J. Healy, C. Hayden, T. Xie, K. Olson, R. Waldo, M. Brundage, H. Gasteiger, J. Abbott, Aspects of the Chemical Degradation of PFSA Ionomers used in PEM Fuel Cells, Fuel Cells. 5 (2005) 302–308. https://doi.org/10.1002/fuce.200400050.

[48]   F.D. Coms, The Chemistry of Fuel Cell Membrane Chemical Degradation, ECS Trans. 16 (2008) 235–255. https://doi.org/10.1149/1.2981859.

[49]   S. Kundu, M.W. Fowler, L.C. Simon, R. Abouatallah, N. Beydokhti, Open circuit voltage durability study and model of catalyst coated membranes at different humidification levels, Journal of Power Sources. 195 (2010) 7323–7331. https://doi.org/10.1016/j.jpowsour.2010.05.027.

[50]   T.A. Zawodzinski, T.E. Springer, J. Davey, R. Jestel, C. Lopez, J. Valerio, S. Gottesfeld, A Comparative Study of Water Uptake By and Transport Through Ionomeric Fuel Cell Membranes, J. Electrochem. Soc. 140 (1993) 1981–1985. https://doi.org/10.1149/1.2220749.

[51]   Y.S. Li, T.S. Zhao, W.W. Yang, Measurements of water uptake and transport properties in anion-exchange membranes, International Journal of Hydrogen Energy. 35 (2010) 5656–5665. https://doi.org/10.1016/j.ijhydene.2010.03.026.

[52]   Y. Singh, R.T. White, M. Najm, T. Haddow, V. Pan, F.P. Orfino, M. Dutta, E. Kjeang, Tracking the evolution of mechanical degradation in fuel cell membranes using 4D in situ visualization, Journal of Power Sources. 412 (2019) 224–237. https://doi.org/10.1016/j.jpowsour.2018.11.049.

[53]   F.E. Hizir, S.O. Ural, E.C. Kumbur, M.M. Mench, Characterization of interfacial morphology in polymer electrolyte fuel cells: Micro-porous layer and catalyst layer surfaces, Journal of Power Sources. 195 (2010) 3463–3471. https://doi.org/10.1016/j.jpowsour.2009.11.032.

[54]   S. Kundu, M.W. Fowler, L.C. Simon, S. Grot, Morphological features (defects) in fuel cell membrane electrode assemblies, Journal of Power Sources. 157 (2006) 650–656. https://doi.org/10.1016/j.jpowsour.2005.12.027.

[55]   S. Prass, S. Hasanpour, P.K. Sow, A.B. Phillion, W. Mérida, Microscale X-ray tomographic investigation of the interfacial morphology between the catalyst and micro porous layers in proton exchange membrane fuel cells, Journal of Power Sources. 319 (2016) 82–89. https://doi.org/10.1016/j.jpowsour.2016.04.031.

[56]   T. Uchiyama, H. Kumei, T. Yoshida, Catalyst layer cracks by buckling deformation of membrane electrode assemblies under humidity cycles and mitigation methods, Journal of Power Sources. 238 (2013) 403–412. https://doi.org/10.1016/j.jpowsour.2013.04.026.

[57]   T. Uchiyama, M. Kato, T. Yoshida, Buckling deformation of polymer electrolyte membrane and membrane electrode assembly under humidity cycles, Journal of Power Sources. 206 (2012) 37–46. https://doi.org/10.1016/j.jpowsour.2012.01.073.

[58]   P.W. Majsztrik, A.B. Bocarsly, J.B. Benziger, Viscoelastic Response of Nafion. Effects of Temperature and Hydration on Tensile Creep, Macromolecules. 41 (2008) 9849–9862. https://doi.org/10.1021/ma801811m.

[59]   A. Kusoglu, A.Z. Weber, New Insights into Perfluorinated Sulfonic-Acid Ionomers, Chem. Rev. 117 (2017) 987–1104. https://doi.org/10.1021/acs.chemrev.6b00159.

[60]   C. Lim, L. Ghassemzadeh, F. Van Hove, M. Lauritzen, J. Kolodziej, G.G. Wang, S. Holdcroft, E. Kjeang, Membrane degradation during combined chemical and mechanical accelerated stress testing of polymer electrolyte fuel cells, Journal of Power Sources. 257 (2014) 102–110. https://doi.org/10.1016/j.jpowsour.2014.01.106.

[61]   S. Kreitmeier, P. Lerch, A. Wokaun, F.N. Büchi, Local Degradation at Membrane Defects in Polymer Electrolyte Fuel Cells, J. Electrochem. Soc. 160 (2013) F456. https://doi.org/10.1149/1.023306jes.

[62]   R.C. McDonald, C.K. Mittelsteadt, E.L. Thompson, Effects of Deep Temperature Cycling on Nafion® 112 Membranes and Membrane Electrode Assemblies, Fuel Cells. 4 (2004) 208–213. https://doi.org/10.1002/fuce.200400015.

[63]   N. Garland, T. Benjamin, J. Kopasz, DOE Fuel Cell Program: Durability Technical Targets and Testing Protocols, ECS Trans. 11 (2007) 923–931. https://doi.org/10.1149/1.2781004.

[64]   R. Mukundan, A.M. Baker, A. Kusoglu, P. Beattie, S. Knights, A.Z. Weber, R.L. Borup, Membrane Accelerated Stress Test Development for Polymer Electrolyte Fuel Cell Durability Validated Using Field and Drive Cycle Testing, J. Electrochem. Soc. 165 (2018) F3085–F3093. https://doi.org/10.1149/2.0101806jes.

[65]   D.-H. Ye, Z.-G. Zhan, A review on the sealing structures of membrane electrode assembly of proton exchange membrane fuel cells, Journal of Power Sources. 231 (2013) 285–292. https://doi.org/10.1016/j.jpowsour.2013.01.009.

[66] H. Yoshida, D. Wachi, M. Mohri, Y. Fujii, N. Sugita, S. Goto, Fuel cell with a seal tightly in contact with an electrode for preventing leakage of a reactant gas, US7326485B2, 2008. https://patents.google.com/patent/US7326485B2/en?oq=US7326485 (accessed October 27, 2018).

[67] P. Stahl, J. Biesdorf, P. Boillat, J. Kraft, K.A. Friedrich, Water Distribution Analysis in the Outer Perimeter Region of Technical PEFC Based on Neutron Radiography, J. Electrochem. Soc. 162 (2015) F677–F685. https://doi.org/10.1149/2.0351507jes.

[68] A.J.L. Steinbach, M.K. Debe, J.M. Le, S.J. Obradovich, E.J. Iverson, Gas diffusion layer incorporating a gasket, US7732083B2, 2010. https://patents.google.com/patent/US7732083B2/en?oq=US7732083 (accessed October 27, 2018).

[69] M. Adachi, Sealing material for fuel cell, US6451468B1, 2002. https://patents.google.com/patent/US6451468B1/en?oq=US6451468 (accessed October 27, 2018).

[70] H. Oschmann, Catalyst-coated membrane with integrated sealing material and membrane-electrode assembly produced therefrom, US8067130B2, 2011. https://patents.google.com/patent/US8067130B2/en?oq=US8067130 (accessed October 27, 2018).

[71] B. Sompalli, B.A. Litteer, W. Gu, H.A. Gasteiger, Membrane Degradation at Catalyst Layer Edges in PEMFC MEAs, J. Electrochem. Soc. 154 (2007) B1349–B1357. https://doi.org/10.1149/1.2789791.

[72] H.E. Martz, C.M. Logan, D.J. Schneberk, P.J. Shull, C.M. Logan, D.J. Schneberk, P.J. Shull, X-Ray Imaging : Fundamentals, Industrial Techniques and Applications, CRC Press, 2016. https://doi.org/10.1201/9781315375199.

[73] X. Huang, R. Solasi, Y. Zou, M. Feshler, K. Reifsnider, D. Condit, S. Burlatsky, T. Madden, Mechanical endurance of polymer electrolyte membrane and PEM fuel cell durability, Journal of Polymer Science Part B: Polymer Physics. 44 (2006) 2346–2357. https://doi.org/10.1002/polb.20863.

[74] K.O. Kjellsen, A. Monsøy, K. Isachsen, R.J. Detwiler, Preparation of flat-polished specimens for SEM-backscattered electron imaging and X-ray microanalysis—importance of epoxy impregnation, Cement and Concrete Research. 33 (2003) 611–616. https://doi.org/10.1016/S0008-8846(02)01029-3.

[75] W.K. Epting, J. Gelb, S. Litster, Resolving the Three-Dimensional Microstructure of Polymer Electrolyte Fuel Cell Electrodes using Nanometer-Scale X-ray Computed Tomography, Advanced Functional Materials. 22 (2012) 555–560. https://doi.org/10.1002/adfm.201101525.

[76] S. Litster, W.K. Epting, E.A. Wargo, S.R. Kalidindi, E.C. Kumbur, Morphological Analyses of Polymer Electrolyte Fuel Cell Electrodes with Nano-Scale Computed Tomography Imaging, Fuel Cells. 13 (2013) 935–945. https://doi.org/10.1002/fuce.201300008.

[77] M. Andisheh-Tadbir, F.P. Orfino, E. Kjeang, Three-dimensional phase segregation of micro-porous layers for fuel cells by nano-scale X-ray computed tomography, Journal of Power Sources. 310 (2016) 61–69. https://doi.org/10.1016/j.jpowsour.2016.02.001.

[78] S. Odaya, R.K. Phillips, Y. Sharma, J. Bellerive, A.B. Phillion, M. Hoorfar, X-ray Tomographic Analysis of Porosity Distributions in Gas Diffusion Layers of Proton Exchange Membrane Fuel Cells, Electrochimica Acta. 152 (2015) 464–472. https://doi.org/10.1016/j.electacta.2014.11.143.

[79] A. Pfrang, S. Didas, G. Tsotridis, X-ray computed tomography of gas diffusion layers of PEM fuel cells: Segmentation of the microporous layer, Journal of Power Sources. 235 (2013) 81–86. https://doi.org/10.1016/j.jpowsour.2013.01.179.

[80] ImageJ, (n.d.). https://imagej.nih.gov/ij/ (accessed February 1, 2020).

[81] D. Ramani, Y. Singh, F.P. Orfino, M. Dutta, E. Kjeang, Characterization of Membrane Degradation Growth in Fuel Cells Using X-ray Computed Tomography, Journal of The Electrochemical Society. 165 (2018) F3200–F3208. https://doi.org/10.1149/2.0251806jes.

[82] R.T. White, D. Ramani, S. Eberhardt, M. Najm, F.P. Orfino, M. Dutta, E. Kjeang, Correlative X-ray Tomographic Imaging of Catalyst Layer Degradation in Fuel Cells, J. Electrochem. Soc. 166 (2019) F914–F925. https://doi.org/10.1149/2.0121913jes.

[83] R.T. White, F.P. Orfino, M.E. Hannach, O. Luo, M. Dutta, A.P. Young, E. Kjeang, 3D Printed Flow Field and Fixture for Visualization of Water Distribution in Fuel Cells by X-ray Computed Tomography, J. Electrochem. Soc. 163 (2016) F1337–F1343. https://doi.org/10.1149/2.0461613jes.

[84] H. Markötter, J. Haußmann, R. Alink, C. Tötzke, T. Arlt, M. Klages, H. Riesemeier, J. Scholta, D. Gerteisen, J. Banhart, I. Manke, Influence of cracks in the microporous layer on the water distribution in a PEM fuel cell investigated by synchrotron radiography, Electrochemistry Communications. 34 (2013) 22–24. https://doi.org/10.1016/j.elecom.2013.04.006.

[85] R.T. White, S.H. Eberhardt, Y. Singh, T. Haddow, M. Dutta, F.P. Orfino, E. Kjeang, Four-dimensional joint visualization of electrode degradation and liquid water distribution inside operating polymer electrolyte fuel cells, Sci Rep. 9 (2019) 1–12. https://doi.org/10.1038/s41598-018-38464-9.

[86]   R.T. White, A. Wu, M. Najm, F.P. Orfino, M. Dutta, E. Kjeang, 4D in situ visualization of electrode morphology changes during accelerated degradation in fuel cells by X-ray computed tomography, Journal of Power Sources. 350 (2017) 94–102. https://doi.org/10.1016/j.jpowsour.2017.03.058.

[87]   D. Ramani, Y. Singh, R.T. White, T. Haddow, F.P. Orfino, M. Dutta, E. Kjeang, Insights into the Evolution of Chemical Degradation in Fuel Cell Membranes Using 4D <em>in Situ</Em> Visualization, in: ECS, 2019. https://ecs.confex.com/ecs/236/meetingapp.cgi/Paper/125907 (accessed May 26, 2020).

[88]   R.T. White, M. Najm, M. Dutta, F.P. Orfino, E. Kjeang, Communication—Effect of Micro-XCT X-ray Exposure on the Performance of Polymer Electrolyte Fuel Cells, J. Electrochem. Soc. 163 (2016) F1206–F1208. https://doi.org/10.1149/2.0751610jes.

[89]   S. Te, Z. Ta, W. Ms, G. S, Characterization of Polymer Electrolyte Fuel-Cells Using AC-Impedance Spectroscopy, J. Electrochem. Soc. 143 (1996) 587–599.

Appendix A. EIS Derivation

The total impedance of Randles circuit, as illustrated in Figure 22 Section 2.6.3, can be derived through the following steps:

$$Z = R_\Omega + \frac{Z_{dl}(R_{ct} + Z_w)}{Z_{dl} + R_{ct} + Z_w}$$

Impedance of double layer capacitor (Z_{dl}) and Warburg impedance (Z_w) can be expressed as:

$$Z_{dl} = \frac{1}{j\omega C_{dl}}$$

$$Z_w = \frac{\sigma}{\omega^{\frac{1}{2}}} - j\frac{\sigma}{\omega^{\frac{1}{2}}}$$

Total impedance can then be written as:

$$Z = R_\Omega + \frac{\frac{1}{j\omega C_{dl}}(R_{ct} + \sigma\omega^{-0.5} - j\sigma\omega^{-0.5})}{\frac{1}{j\omega C_{dl}} + R_{ct} + \sigma\omega^{-0.5} - j\sigma\omega^{-0.5}}$$

$$= R_\Omega + \frac{R_{ct} + \sigma\omega^{-0.5} - j\sigma\omega^{-0.5}}{1 + j\omega C_{dl}R_{ct} + jC_{dl}\sigma\omega^{0.5} + C_{dl}\sigma\omega^{0.5}}$$

$$= R_\Omega + \frac{R_{ct} + \sigma\omega^{-0.5} - j\sigma\omega^{-0.5}}{1 + C_{dl}\sigma\omega^{0.5} + j\omega C_{dl}(R_{ct} + \sigma\omega^{-0.5})}$$

Multiply $1 + C_{dl}\sigma\omega^{0.5} - j\omega C_{dl}(R_{ct} + \sigma\omega^{-0.5})$ in both numerator and denominator to get rid of imaginary part in denominator:

$$Z = R_\Omega + \frac{(R_{ct} + \sigma\omega^{-0.5} - j\sigma\omega^{-0.5})[1 + C_{dl}\sigma\omega^{0.5} - j\omega C_{dl}(R_{ct} + \sigma\omega^{-0.5})]}{(1 + C_{dl}\sigma\omega^{0.5})^2 + \omega^2 C_{dl}^2(R_{ct} + \sigma\omega^{-0.5})^2}$$

$$= R_\Omega + \frac{R_{ct} + \sigma\omega^{-0.5} - j\omega C_{dl}(R_{ct}^2 + 2R_{ct}\sigma\omega^{-0.5} + \sigma^2\omega^{-1}) - j(\sigma\omega^{-0.5} + \sigma^2 C_{dl})}{(1 + C_{dl}\sigma\omega^{0.5})^2 + \omega^2 C_{dl}^2(R_{ct} + \sigma\omega^{-0.5})^2}$$

$$= R_\Omega + \frac{R_{ct} + \sigma\omega^{-0.5}}{(1 + C_{dl}\sigma\omega^{0.5})^2 + \omega^2 C_{dl}^2(R_{ct} + \sigma\omega^{-0.5})^2}$$

$$- j\frac{\omega C_{dl}(R_{ct} + \sigma\omega^{-0.5})^2 + \sigma\omega^{-0.5}(1 + \sigma\omega^{0.5}C_{dl})}{(1 + C_{dl}\sigma\omega^{0.5})^2 + \omega^2 C_{dl}^2(R_{ct} + \sigma\omega^{-0.5})^2}$$

As a result,

$$Z_{Re} = R_\Omega + \frac{R_{ct} + \sigma\omega^{-0.5}}{(1 + C_{dl}\sigma\omega^{0.5})^2 + \omega^2 C_{dl}^2 (R_{ct} + \sigma\omega^{-0.5})^2}$$

$$Z_{Im} = \frac{\omega C_{dl}(R_{ct} + \sigma\omega^{-0.5})^2 + \sigma\omega^{-0.5}(1 + \sigma\omega^{0.5}C_{dl})}{(1 + C_{dl}\sigma\omega^{0.5})^2 + \omega^2 C_{dl}^2 (R_{ct} + \sigma\omega^{-0.5})^2}$$

In low frequency region where ω approaches 0:

$$Z_{Re} = R_\Omega + \frac{R_{ct} + \sigma\omega^{-0.5}}{(1 + C_{dl}\sigma\omega^{0.5})^2 + \omega^2 C_{dl}^2 (R_{ct} + \sigma\omega^{-0.5})^2}$$

$$= R_\Omega + \frac{R_{ct}}{1 + \omega^2 C_{dl}^2 (R_{ct} + \sigma\omega^{-0.5})^2} + \frac{\sigma\omega^{-0.5}}{1 + \omega^2 C_{dl}^2 (R_{ct} + \sigma\omega^{-0.5})^2}$$

$$= R_\Omega + R_{ct} + \sigma\omega^{-0.5}$$

$$Z_{Im} = \frac{\omega C_{dl}(R_{ct} + \sigma\omega^{-0.5})^2 + \sigma\omega^{-0.5}(1 + \sigma\omega^{0.5}C_{dl})}{(1 + C_{dl}\sigma\omega^{0.5})^2 + \omega^2 C_{dl}^2 (R_{ct} + \sigma\omega^{-0.5})^2}$$

$$= \frac{\omega C_{dl}R_{ct}^2 + 2R_{ct}\sigma\omega^{0.5}C_{dl} + \sigma^2 C_{dl} + \sigma\omega^{-0.5} + \sigma^2 C_{dl}}{1 + \omega^2 C_{dl}^2 (R_{ct} + \sigma\omega^{-0.5})^2}$$

$$= 2\sigma^2 C_{dl} + \sigma\omega^{-0.5}$$

Rearranging gives the relation between Z_{Im} and Z_{Re}:

$$Z_{Im} = Z_{Re} - R_\Omega - R_{ct} + 2\sigma^2 C_{dl}$$

In high frequency region where Warburg impedance is negligible and Randles circuit is simplified as indicated in Figure 24:

$$Z = R_\Omega + \frac{\dfrac{R_{ct}}{j\omega C_{dl}}}{\dfrac{1}{j\omega C_{dl}} + R_{ct}}$$

$$= R_\Omega + \frac{R_{ct}}{1 + j\omega C_{dl}R_{ct}}$$

$$= R_\Omega + \frac{R_{ct}(1 - j\omega C_{dl}R_{ct})}{1 + \omega^2 C_{dl}^2 R_{ct}^2}$$

$$= R_\Omega + \frac{R_{ct}}{1 + \omega^2 C_{dl}^2 R_{ct}^2} - j\frac{\omega C_{dl}R_{ct}^2}{1 + \omega^2 C_{dl}^2 R_{ct}^2}$$

As a result,

$$Z_{Re} = R_\Omega + \frac{R_{ct}}{1 + \omega^2 C_{dl}^2 R_{ct}^2}$$

$$Z_{Im} = \frac{\omega C_{dl} R_{ct}^2}{1 + \omega^2 C_{dl}^2 R_{ct}^2}$$
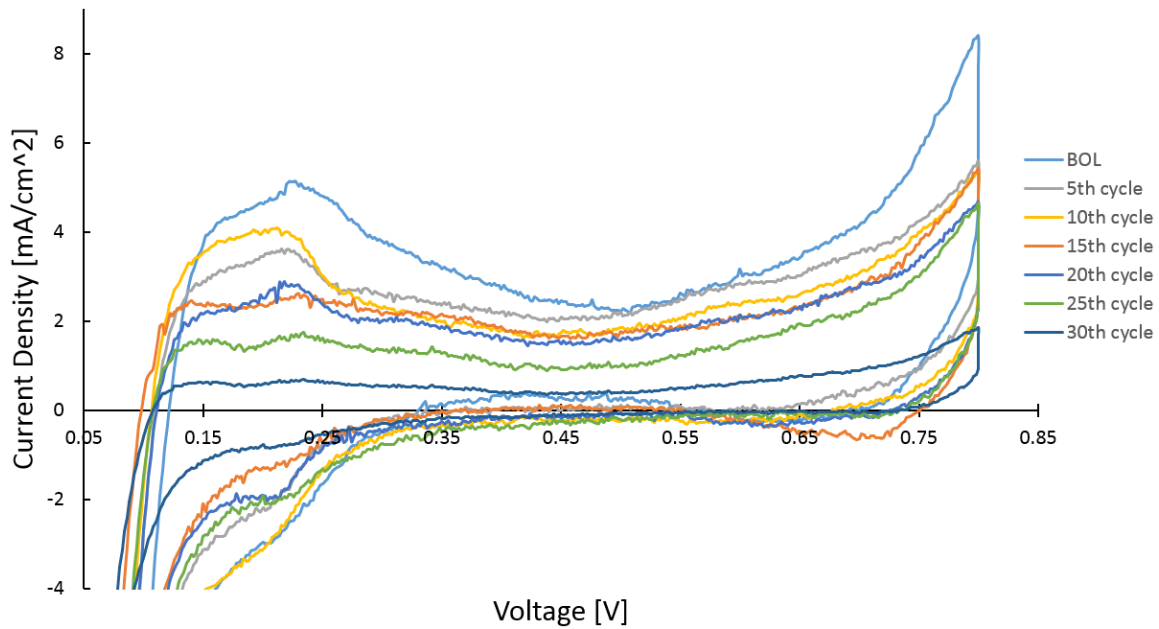
Appendix B. Diagnostics CV and EIS Data

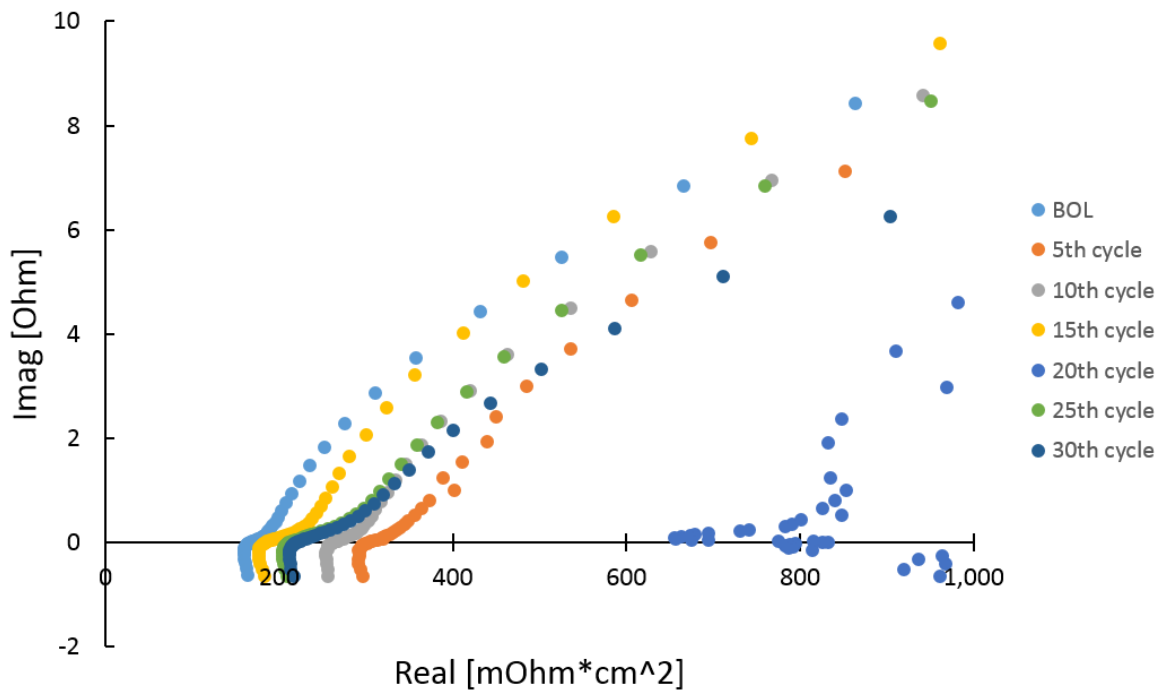**Figure B1:**   Diagnostics CV data of MEA with edge design 2 from BOL to EOL.

Figure B2:   Diagnostics EIS data of MEA with edge design 2 from BOL to EOL.

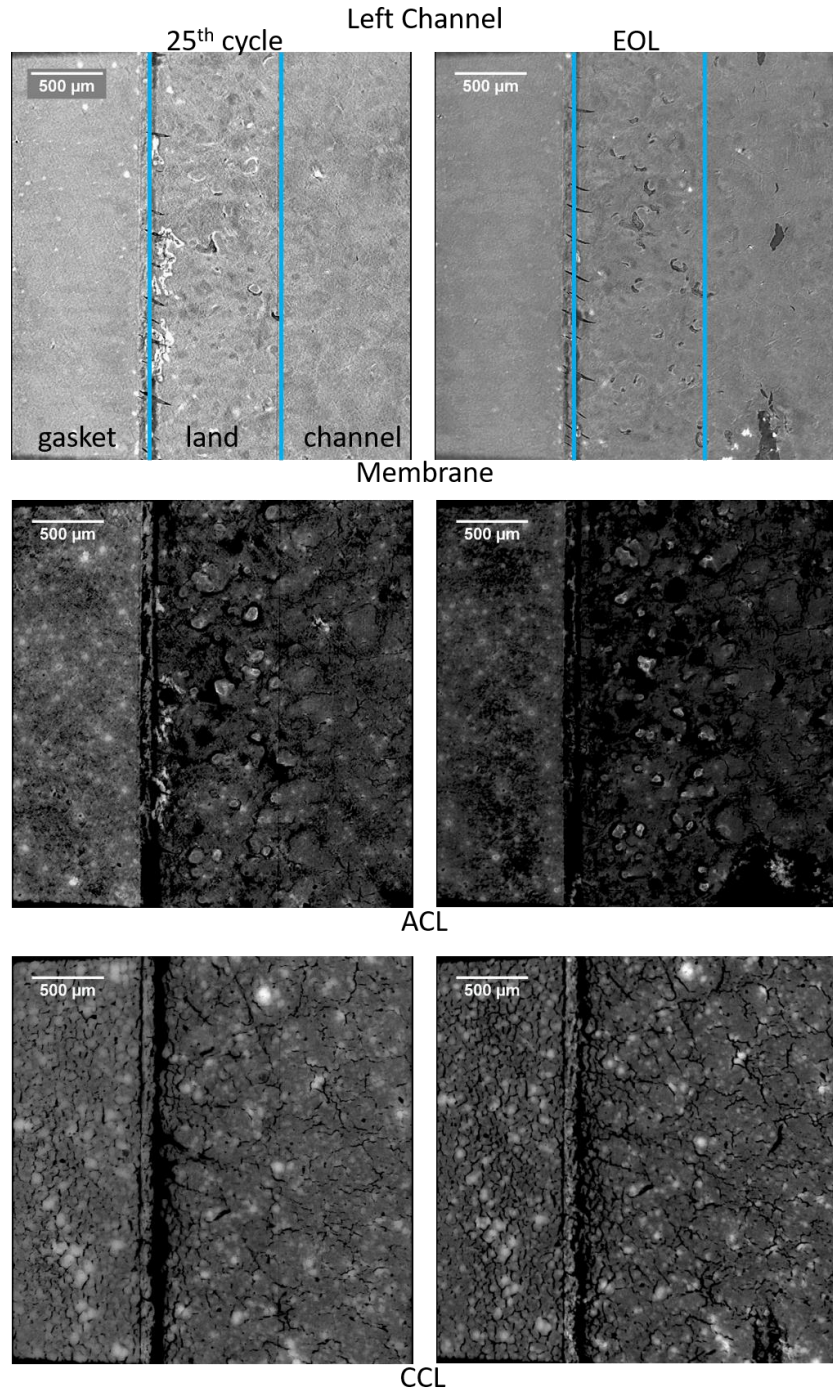# Appendix C. 4D *In situ* XCT Images for Crack Propagation

Left Channel

25th cycle

EOL

500 µm

500 µm

gasket   land   channel

Membrane

500 µm

500 µm

ACL

500 µm

500 µm

CCL

Figure C1: **Left channel CCM planar views at 25th AST cycle (left) and EOL (right).**

Right Channel

25th cycle

EOL

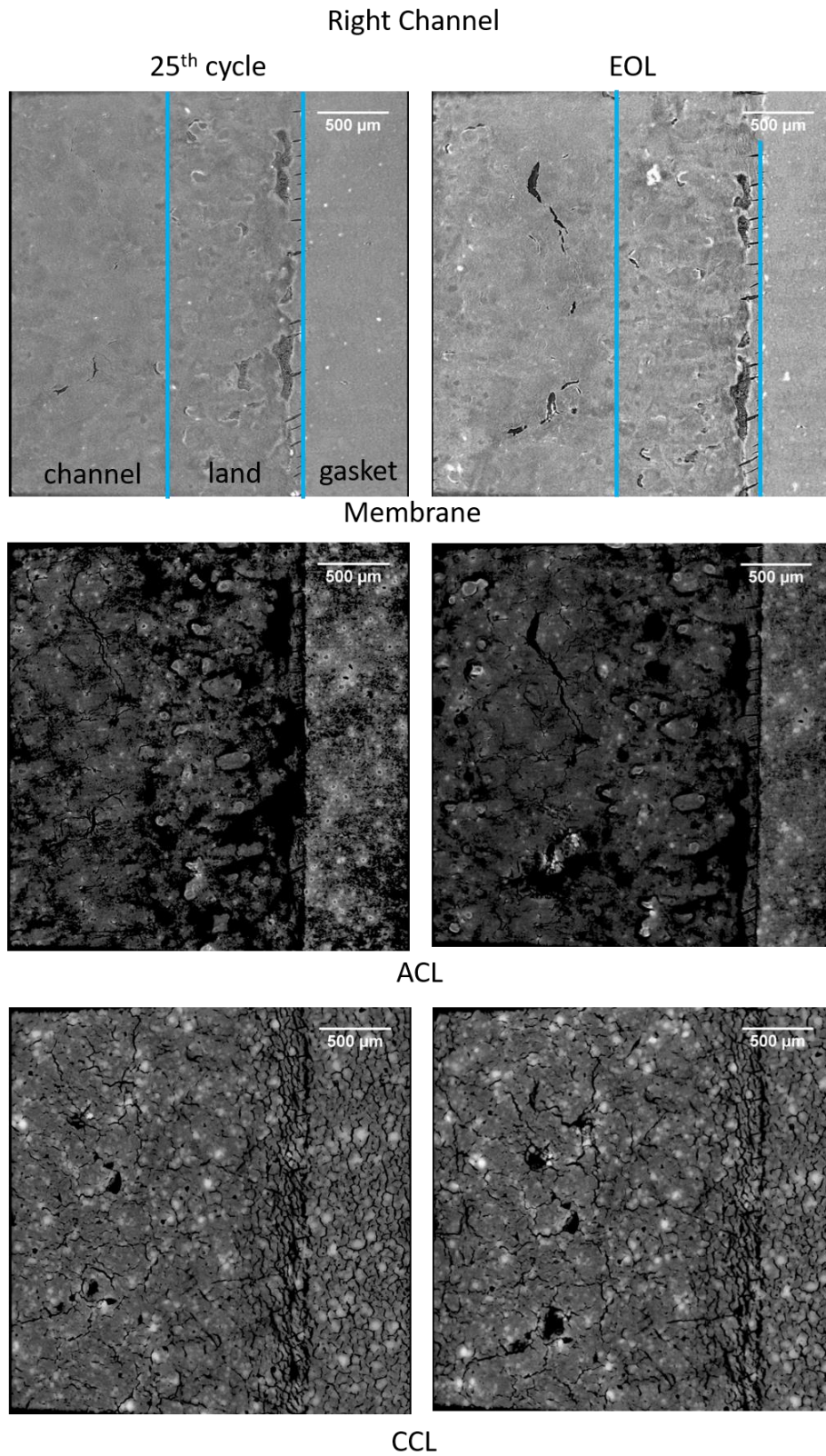channel   land   gasket

Membrane

ACL

CCL

Figure C2:   Right channel CCM planar views at 25th AST cycle (left) and EOL (right).